Development of fast timing detector for CMS experiment upgrade at CERN

Konstantin Shchablo

N d'ordre NNT : 2020LYSE1328

THÈSE DE DOCTORAT DE L'UNIVERSITÉ DE LYON
opérée au sein de
l'Université Claude Bernard Lyon 1

École doctorale ED52
Physique et d'Astrophysique de Lyon (PHAST)

Spécialité de doctorat : Physique des particules

Soutenue publiquement le 15/12/2020, par :
Konstantin SHCHABLO

Développement d'un détecteur à grande précision temporelle pour la mise en jouvence de l'expérience CMS au CERN.

Devant le jury composé de :

Mme FOUZ MaryCruz, Directrice de Recherche, CIEMAT (Espagne)	**Rapporteur**
Mme CARLOGANU Cristina, Directrice de Recherche, CNRS-IN2P3	**Rapporteur**
M. DE LA TAILLE Christophe, Ingénieur de Recherche, CNRS-IN2P3	**Examinateur**
M. CONTARDO Didier, Directeur de Recherche, CNRS/IN2P3	**Président du jury**
M. LAKTINEH Imad, Professeur des universités, Université Lyon 1	**Directeur de thèse**
M. GOUZEVITCH Maxime, Chargé de Recherche, CNRS-IN2P3	**Co-encadrant**

Contents

Chapter 1

Introduction

French

Cette thèse est consacrée au développement et aux tests de nouveaux types de Chambres à Plaques résistives (RPC) pour le détecteur Compact muon solenoid (CMS) qui collecte les données du Grand collisionneur des Hadrons (LHC) au Conseil Européen pour la recherche nucléaire (CERN). Ces détecteurs vont servir pour la mise à jour de CMS dans le cadre du programme de haute luminosité (HL-LHC) qui commencera en 2025. Ces chambres améliorées (iRPC) seront placées dans la zone la plus proche du faisceau de la partie avant du spectromètre à muons de CMS où le taux de radiations est incompatible avec le fonctionnement des chambres RPC standard.

Le premier chapitre sur les particules élémentaires, pose les bases historiques, théoriques et expérimentales de la physique des particules. Ce sera une description brève du Modèle Standard et de ses extensions qui ont amené à la conception et la réalisation des collisionneurs toujours plus puissants et des détecteurs plus performants.

Le deuxième chapitre présente le LHC et la chaine d'accélération qui a permis d'atteindre un niveau d'énergie jusqu'à présent jamais atteint. Ce chapitre détaille aussi le détecteur CMS et tout ses sous-détecteurs et en particulier les RPC. Nous parlerons aussi du projet HL-LHC et de la mise à jour du détecteur CMS.

Les détails du projet iRPC sont présentés dans le chapitre suivant où on parlera du schéma de ir-PC avec une description des prototypes, des méthodes et des solutions trouvées pour optimiser les performances. La carte de lecture électronique (FEB), ainsi que les cartes (PCB) à pistes qui ont été construits et testés pendant la phase Recherche et Développement, et la nouvelle approche pour le partitionnement et traitements des données seront abordées dans ce chapitre.

Le chapitre quatre discute des capacités et des performances des iRPC, tels que l'efficacité, la résolution en temps, la capacité à soutenir des taux de particules élevés.

Le dernier chapitre décrit les améliorations possibles de ces chambres dans le système d'acquisition de CMS. Enfin la thèse est conclue par des considérations sur la possibilité d'utiliser ces chambres pour la recherche de nouvelles particules lourdes à longue durée de vie.

English

This thesis is devoted to the development and testing of new types of Resistive Plate Chamber (RPC) for the Compact Muon Solenoid (CMS) detector located on the Large Hadron Collider (LHC) at the European Organization for Nuclear Research (CERN). This new RPC will have to withstand high particle fluxes at the High-Luminosity LHC phase (HL-LHC).

The second chapter on elementary particles briefly describes the historical, theoretical, and experimental foundations of elementary particle physics. A brief description of the Standard Model (SM) and extensions of it are given, which explains the reason of the conception and realization of increasingly powerful colliders as well as more precise detectors.

The third chapter presents the LHC, the most powerful collider. This chapter also details the CMS detector and all its sub-detectors, where Resistive Plate Chambers are reviewed in detail. It also presents the data acquisition system and many improvements needed to upgrade it to take full advantage of the instantaneous luminosity increase provided by HL-LHC.

The fourth chapter, on the improved Resistive Plate Chambers (iRPC), includes the new RPC scheme with a description of the prototypes' characteristics and the solutions needed to reach the chamber's requested performance. The Front-End Board (FEB) electronics and strips PCB, which were built and tested during Research and development (R&D), and the new approach for clustering and processing data will also be described in this chapter.

The fifth and sixth chapters explain the capability and performance that include performance studies such as efficiency, time resolution, rate capability studies, etc. The last part includes an approach based on iRPC output that might improve the CMS Muon system's trigger efficiency and possible usage of this chamber to improve search algorithms of the hypothetical HSCP.

The last chapter summarizes all results described in chapters fourth to sixth, in line with the set objectives of the Ph.D. thesis. Also, it represents further steps to complete the R&D of iRPC for CMS.

Chapter 2

The Physics of Elementary Particles

The physics of elementary particles is the physics section that studies elementary particles' structure and properties and their interactions. The purpose of this study is to understand and establish the most fundamental laws ruling our Universe. The particle physics research already has more than a century of history, and during this time, new concepts of the quantum world which are not inherent in classical physics have been generated. The construction of the Standard Model of fundamental interactions (strong, weak, electromagnetic) of quarks and leptons is one of the main results of the modern physics of elementary particles. This model is based on the special theory of relativity, local symmetry, and the mechanism of spontaneous violation of symmetry. In recent years, model predictions have been tested many times in experiments. At present, it is the only physical theory that adequately describes the world up to distances of about 10^{-18} meters.

2.1 The Standard Model

The Standard Model (SM) theory allows us to predict the properties of thousands of different processes in the Universe and classify all known elementary particles. The theory describes the Universe matter by using six varieties of leptons and six types of quarks. Bosons provide all interactions and force carriers. The SM description of the particle content may be organized into the chart shown below:

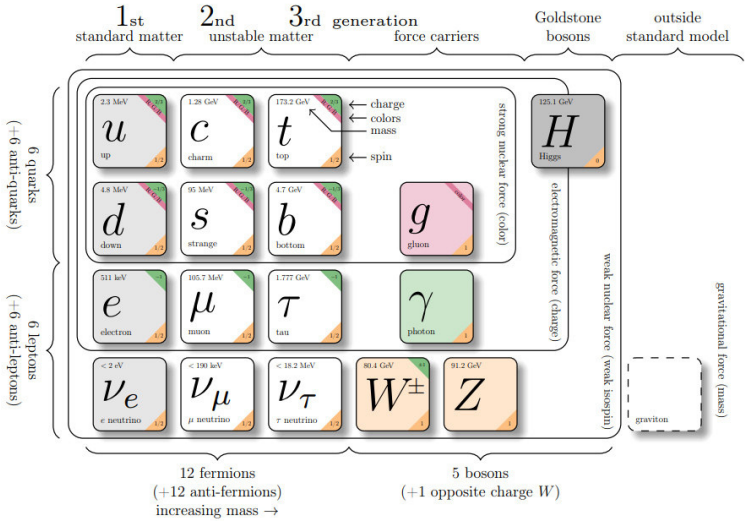

Figure 2-1: The Standard Model: classification of quarks, leptons and bosons.

2.1.1 The Particle Content

Fermions are divided into quarks and leptons: six leptons and six quarks. Quarks have no structure, and each quark has three color states: red (R), green (G), and blue (B). Color does not manifest itself in the observed hadrons and works only inside them in combination with six flavors (up, down, strange, charm, top, and bottom) of the discovered quarks. Since each quark has three colors, 18 types of quarks are considered. Leptons are also fundamental particles. They have no structure, as well. There are six of them: three charged e, μ, τ and three neutral ν_{e}, ν_{μ}, ν_{τ}. Leptons are involved only in electromagnetic and weak interactions. Chart 2.1 shows the proprieties of fundamental fermions (leptons and quarks united in three generations): the electric charge (given in units of electron charge), spin, and the particle mass. The substance surrounding us consists of fermions of the first generation. The influence from particles of the second and third generations manifested itself during the early Universe. Among the structureless fundamental particles, a special role is played by the fundamental gauge bosons, which have an integer internal quantum number of spin. Gauge bosons are responsible for three types of fundamental interactions: strong (gluons), electromagnetic (photon), weak (bosons). The Higgs boson has a key role in the SM, explaining why elementary particles except photons and gluons have a mass. In particular, the Higgs boson explains why the photon has no mass, while the W and Z bosons are very heavy.

2.1.2 Fundamental Forces

All of the physical phenomena occurring in nature are determined by only four fundamental forces: strong, electromagnetic, weak, and gravitational. The sector of Quantum Chromodynamics (QCD) is a Yang-Mills gauge theory [117] with $SU(3)$ symmetry that describes interactions of quarks and gluons. The QCD theory has an excellent agreement about what must be happening within the high energy particle collisions: the formation of color charged flux tubes among quarks and antiquarks and the eventual fragmentation of those flux tubes into mesons and baryons, rather than free quarks and gluons [63]. The effective Yukawa interaction can describe the nuclear force between nucleons (which are fermions), mediated by pions (pseudoscalar mesons). The Yukawa interaction is also used in SM to describe the coupling between the Higgs field and massless lepton and quark fields. By spontaneous symmetry breaking, fermions acquire a mass proportional to the vacuum value of the Higgs field. The Higgs mechanism gives an explanation of the generation mechanism of the mass for gauge bosons. Without the Higgs mechanism, all bosons would be considered massless, but measurements show that the W+, W−, and Z_0 bosons have relatively large masses.

2.1.3 Theoretical Aspects

The Standard Model is a theoretical construction in the physics of elementary particles. It was developed in stages throughout the second half of the 20th century, through the work of many scientists around the world [87].

The SM is defined using the quantum field theory framework using gauge symmetry (Eq. 2.1). The principles of interactions are controlled by symmetries founded by Noether's theorem [86], which states that every differentiable symmetry of the action of a physical system has a corresponding conservation law.

$$SU(3)_C \otimes SU(2)_L \otimes U(1)_Y, \tag{2.1}$$

where C is color charge; L is the left-handed fields; Y is the hypercharge.

Strong interaction (quarks and gluons) requires the conservation of the color charge $SU(3)_C$:

$$L_{\mathrm{QCD}} = \bar{\psi}\,(i\gamma^\mu D_\mu - m\,)\,\psi - \frac{1}{4}G_{\mu\nu}G^{\mu\nu}, \tag{2.2}$$

where ψ is the quark field with mass m; the γ^μ are Dirac matrices; D_μ is the covariant derivative for QCD ($D_\mu := \partial_\mu - ig_s\,G^\alpha_\mu\,\frac{\lambda_\alpha}{2}$, where g_s is the coupling constant of the strong interaction; G is the gluon gauge field, for eight different gluons $\alpha = 1\ldots 8$; λ_α is one of the eight Gell-Mann matrices.); $G_{\mu\nu}$ is the QCD tensor ($G^a_{\mu\nu} = \partial_\mu \mathcal{A}^a_\nu - \partial_\nu \mathcal{A}^a_\mu + g_s f^{abc}\mathcal{A}^b_\mu \mathcal{A}^c_\nu$, where $\mathcal{A}^c_\nu$ is the gauge field of the gluon.).

The electroweak is the unified description of two interactions: electromagnetic (QED) and the weak one. The basic processes in QED are electron-muon scattering ($e+\mu \to e+\mu$), electron-electron scattering ($e^- + e^- \to e^- + e^-$), electron-positron scattering ($e^- + e^+ \to e^- + e^+$), Compton scattering ($\gamma + e^- \to \gamma + e^-$), pair production ($\gamma + \gamma \to e^+ + e^-$) and pair annihilation ($e^- + e^+ \to \gamma + \gamma$). The examples of weak interactions processes may be such as neutrino-electron scattering ($\nu_\mu + e^- \to \nu_\mu + e^-$) for neutral weak interactions (Z boson) and muon decay ($\mu \to e + \nu_\mu + \overline{\nu_e}$), neutron decay ($n \to e + p + e + \overline{\nu_e}$), pion decay ($\pi^- \to l^- + e + \overline{\nu_l}$) for charged weak interactions (W bosons) and W and Z bosons also can couple to themselves.

The electroweak theory group ($SU(2)_L \otimes U(1)_Y$) imposes the local symmetry of the isospin associated with the group $SU(2)_L$ as well as the local symmetry of the hypercharge $U(1)_Y$:

$$\begin{aligned} L_{EM} = &-\frac{1}{4}W^a_{\mu\nu}W^{\mu\nu}_a - \frac{1}{4}B_{\mu\nu}B^{\mu\nu} + \bar{L_i}iD_\mu\gamma^\mu L_i + \bar{e_{R_i}}iD_\mu\gamma^\mu e_{R_i} \\ &+\bar{Q_i}iD_\mu\gamma^\mu Q_i + \bar{u_{R_i}}iD_\mu\gamma^\mu u_{R_i} + \bar{d_{R_i}}iD_\mu\gamma^\mu d_{R_i} \end{aligned} \tag{2.3}$$

where $W^a_{\mu\nu}(a = 1, 2, 3)$ ($W^a_{\mu\nu} = \partial_\mu W^a_\nu - \partial_\nu W^a_\mu + g\epsilon_{abc}W^b_\mu W^c_\nu$) is weak tensor associated the of the weak isospin group $SU(2)_L$ the coupling constant of the weak isospin and ϵ_{abc} the corresponding antisymmetric structure constants; $B_{\mu\nu}$ ($B_{\mu\nu} = \partial_\mu B_\nu - \partial_\nu B_\mu$) is the isoscalar field associated with the hypercharge group $U(1)_Y$; D_μ is the covariant derivative ($D_\mu := \partial_\mu - ig_2\,W^\alpha_\mu\,\frac{\tau_a}{2} + ig_1 B_\mu \frac{Y}{2}$, where Y is the weak hypercharge, τ_a are the Pauli spin matrixes.); i is sub represents index of three generations of fermions;

the γ^μ are Dirac matrices; L and e are the left-handed doublet and right-handed singlet electron fields; Q, u, d are the left-handed doublet, right-handed singlet up, and right handed singlet down quark fields.

In order to obtain the electrical charges for each fermion, the weak hypercharge operator Y of the $U(1)_Y$ is defined as a linear combination of the charge operator and the third component of the weak-isospin generators. The hypercharge (Y) of left-handed and right-handed fundamental fermion (Eq. 2.4 leptons, Eq. 2.5 quarks) apply:

$$Y(\ ((\frac{\nu_e}{e}),(\frac{\nu_\mu}{\mu}),(\frac{\nu_\tau}{\tau}))_L\ ) = -1, \quad Y((\nu_e,\nu_\mu,\nu_\tau)_R) = 0, \quad Y((e,\mu,\tau)_R) = -2 \tag{2.4}$$

$$Y(\ ((\frac{u}{d}),(\frac{c}{s}),(\frac{t}{b}))_L\ ) = \frac{1}{3}, \quad Y((d,s,b)_R) = -\frac{2}{3}, \quad Y((u,s,t)_R) = \frac{4}{3} \tag{2.5}$$

Under local gauge invariant in the electroweak sector, the fermions' mass terms and gauge bosons are not introduced. If mass terms are explicitly introduced, the local gauge invariance is violated. Thus, the mechanism of spontaneous symmetry breaking must be applied. Electroweak symmetry is inconsistent with the description of massive fermions. Indeed, in the Lagrangian, the terms of the mass of fermions contain couplings of left-handed and right-handed fields, which have different transformation proper-ties (Eq. 2.7).

$$m\overline{\psi}\psi = m(\overline{\psi}_L\psi_R + \overline{\psi}_R\psi_L) \tag{2.6}$$

However, these terms that break the symmetry $SU(2)$ are not included in the Lagrangian. Furthermore, experiments show that the W gauge bosons must have mass, and the introduction of mass terms for these bosons is also impossible for the same reasons. In order to solve these problems, a complex scalar field Φ a doublet of $SU(2)_L$ four real fields ϕ_i and a hypercharge $Y = 1$ are introduced:

$$\Phi = \begin{pmatrix}\phi^+\\ \phi^0\end{pmatrix} = \begin{pmatrix}\phi_1 + i\phi_2\\ \phi_3 + i\phi_4\end{pmatrix} \tag{2.7}$$

The most general Lagrangian expression for a complex scalar field is used:

$$L_{Higgs} = (D_\mu\Phi)^\dagger(D_\mu\Phi) - V(\Phi), \tag{2.8}$$

where D_μ is the covariant derivative ($D_\mu = \partial_\mu - ig_2 W_\mu^\alpha \frac{\tau_a}{2} + ig_1\frac{1}{2}B_\mu$, where g_1 is the term of B boson coupling to the weak hypercharge Y; g_2 is the term of W left-handed weak isospin doublets.); $V(\Phi)$ (Eq. 2.10) is the potential.

$$V(\Phi) = \mu^2\Phi^\dagger\Phi + \lambda(\Phi^\dagger\Phi)^2 \tag{2.9}$$

The case where $\mu^2 < 0$ and $\lambda > 0$ is shown in Figure 2-2.

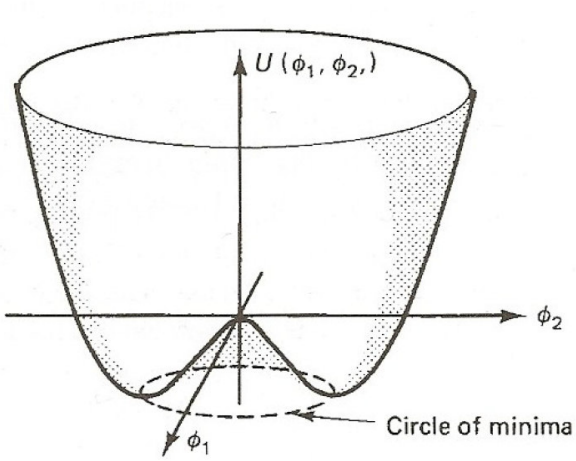

Figure 2-2: Potential for $V(\Phi)$ for $\mu^2 < 0$ and $\lambda > 0$ [64].

Since the potential could be chosen (Eq. 2.10) with minimum energy satisfying $\Phi^\dagger\Phi = \frac{\nu^2}{2}$ such as:

$$\Phi_{min} = \frac{1}{\sqrt{2}}\begin{pmatrix}0\\ \nu\end{pmatrix},\ where\ \nu = \sqrt{\frac{\mu^2}{\lambda}} \tag{2.10}$$

Next developing the doublet Φ_h around this state of the Higgs field that breaks the symmetry $SU(2)_L \otimes U(1)_Y$:

$$\Phi_h = \frac{1}{\sqrt{2}}\begin{pmatrix}ih_1 + h_2\\ (h+\nu) + ih_3\end{pmatrix} \approx e^{i\theta}\begin{pmatrix}0\\ \frac{h+\nu}{\sqrt{2}}\end{pmatrix}, \tag{2.11}$$

where θ is the Nambu–Goldstone boson.

Due to the gauge invariance, the unitary gauge can be written as:

$$\Phi_h \to \frac{1}{\sqrt{2}}\begin{pmatrix}0\\ h+\nu\end{pmatrix} \tag{2.12}$$

The choice of unitary gauge for term of Lagragean $|D^\mu\Phi|^2$ is possible to define the masses of bosons (Eq. 2.13).

$$\left|(\partial_\mu - ig_2 W_\mu^\alpha \frac{\tau^a}{2} + ig_1\frac{1}{2}B_\mu)\frac{1}{\sqrt{2}}\begin{pmatrix}0\\ h+\nu\end{pmatrix}\right|^2 = \frac{1}{2}\left|\begin{pmatrix}-\frac{ig_2}{2}(W_\mu^1 - iW_\mu^2)(h+\nu)\\ (\partial_\mu + \frac{i}{2}(g_2W_\mu^3 - g_1B_\mu))(h+\nu)\end{pmatrix}\right|^2 =$$

$$\frac{1}{2}(\partial_\mu + h)^2 + \frac{1}{8}g_2^2(h+\nu)^2\left|W_\mu^1 - iW_\mu^2\right| - \frac{1}{8}g_2^2(h+\nu)^2\left|g_2W_\mu^3 - g_1B_\mu\right| \tag{2.13}$$

So, the Lagrangian's kinetic part of the Higgs sector gives the following bosons and then the mass terms ($M_W^2W_\mu^+W^{-\mu}$, $\frac{1}{2}M_Z^2Z_\mu Z^\mu$, $\frac{1}{2}M_A^2A_\mu A^\mu$) show that $W^\pm, Z$ have masses:

$$W^\pm \equiv \frac{1}{\sqrt{2}}(W_\mu^1 \mp iW_\mu^2)\ with\ mass\ m_{W^\pm} = \frac{g_2\nu}{2} \tag{2.14}$$

$$Z_\mu \equiv \frac{1}{\sqrt{g_2^2+g_2^1}}(g_2 W_\mu^3 - g_1 B_\mu) \; with \; mass \; m_{Z_0} = \frac{\sqrt{g_2^2+g_1^2}}{2}\nu \tag{2.15}$$

$$A_\mu \equiv \frac{1}{\sqrt{g_2^2+g_2^1}}(g_2 W_\mu^3 + g_1 B_\mu) \; with \; mass \; m_A = 0 \tag{2.16}$$

Next, for the fermion mass generate in the electroweak Standard Model, the Yukawa Lagrangian is needed:

$$L_{Yukawa} = -f_e \bar{L}\Phi e_R - f_d \bar{Q}\Phi d_R - f_u \bar{Q}\tilde{\Phi} u_R + h.c. \tag{2.17}$$

Assuming a Higgs field Φ with $Y = 1$ as before, plus the isodoublet $\tilde{\Phi} = i\tau_2\Phi^*$, which has $Y = -1$:

$$\Phi = \begin{pmatrix} \phi^+ \\ \phi^0 \end{pmatrix} \rightarrow \frac{1}{\sqrt{2}}\begin{pmatrix} 0 \\ h+\nu \end{pmatrix} \quad \tilde{\Phi} = \begin{pmatrix} \phi^{0*} \\ -\phi^- \end{pmatrix} \rightarrow \frac{1}{\sqrt{2}}\begin{pmatrix} h+\nu \\ 0 \end{pmatrix} \tag{2.18}$$

then the equation 2.17 takes the form:

$$L = -\frac{f_e\nu}{\sqrt{2}}(\bar{e_L}e_R + \bar{e_R}e_L) - \frac{f_u\nu}{\sqrt{2}}(\bar{u_L}u_R + \bar{u_R}u_L) - \frac{f_d\nu}{\sqrt{2}}(\bar{d_L}d_R + \bar{d_R}d_L) \tag{2.19}$$

eventually getting the fermion masses:

$$m_{e,u,d} = \frac{f_{e,u,d}\nu}{\sqrt{2}} \tag{2.20}$$

It should be noted that for quarks that their mass states, not equal electroweak states flavor. The physical states are given by diagonalization the up and down quark mass matrices by Cabibbo-Kobayakshi-Maskawa (CKM) matrix that achieved by switching from the base of the eigenstates of flavor to the eigenstates of mass.

$$M_{CKM} = \begin{pmatrix} c_{12}c_{13} & s_{12}c_{13} & s_{13}e^{-i\delta_{13}} \\ -s_{12}c_{23} - c_{12}s_{23}s_{13}e^{i\delta_{13}} & c_{12}c_{23} - s_{12}s_{23}s_{13}e^{i\delta_{13}} & s_{23}c_{13} \\ s_{12}s_{23} - c_{12}c_{23}s_{13}e^{i\delta_{13}} & -c_{12}s_{23} - s_{12}c_{23}s_{13}e^{i\delta_{13}} & c_{23}c_{13} \end{pmatrix} \tag{2.21}$$

where $s_{ij} = sin(\theta_{ij})$; $c_{ij} = cos(\theta_{ij})$; δ is CP-violating phase.

2.1.4 Theoretically Predictions and Beyond SM

The Standard Model is theoretically self-consistent, and it has a lot of successful predictions (Fig. 2-3).

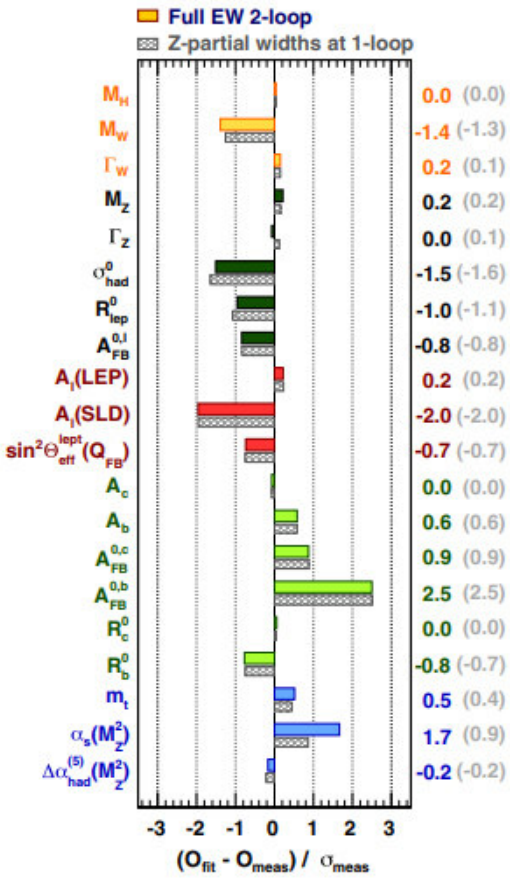

Figure 2-3: Comparison of the adjustment results with direct measurements of some standard model parameters [110].

One thing to note is that the Standard Model does not entirely explain baryon asymmetry, nor does it incorporate the theory of gravitation as described by general relativity. It also does not include neutrino oscillations and their non-zero masses.

The coupling constants $g_e = \alpha_1$, $g_w = \alpha_2$, $g_s = \alpha_3$ respectively of the electromagnetic interaction, weak and strong depend on the energy scale. It turns out that these three constants are close to each other at high energy but do not match at a single point. The convergence towards a single high-energy value is necessary for a theory that would unify these three interactions. The calculation of the evolution of constants by the renormalization method, which does not lead to their convergence, tends to prove the incompleteness of the Standard Model (Fig. 2-4).

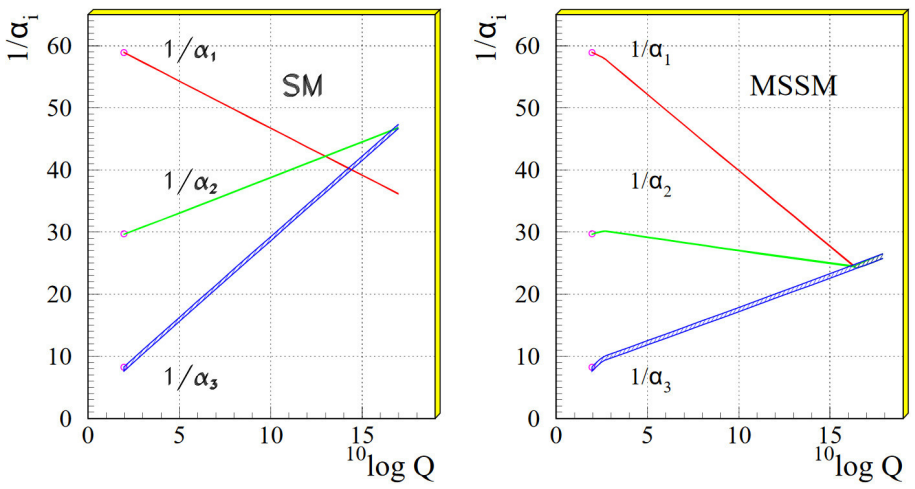

Figure 2-4: Evolution of the inverse of the three coupling constants in the Standard Model (left) and in the supersymmetric extension of the SM (right) [73].

Many theories that go beyond the Standard Model try to explain and solve SM problems [83]. Supersymmetry (SUSY) and theories built with its help are considered to be among the SM extension candidates. The basic prediction of SUSY is that for each Standard Model particle, there is a super-partner, which spin differs by $\frac{1}{2}$. Since no such partners have been found, the supersymmetry must be broken. As it is impossible to cover all space of SUSY parameters, assumptions about supersymmetry breaking are made. It leads to the formulation of models with a small number of parameters (MSSM) on the scale of supersymmetry breaking. These theories predict, in some scenarios, the presence of exotic Long-Lived Particles (LLPs). The following theories can be seen as examples: Gauge-Mediated Supersymmetry Breaking (GMSB) models [60], Split Supersymmetry (Split-SUSY) [61, 69, 76] Magnetic Monopoles [50] for looking Heave Stable Charged Particle (HSCP) that are interesting since they may be seen in modern detectors (See Ch. 6.2).

2.2 Experimental techniques

The tool for studying the structure of matter is an accelerator that creates particles of such high energy that they are able to penetrate the deep regions of the studied micro-object. A particle accelerator can be compared with a microscope. It is known from classical optics that to study the structure of an object having a size of d, the object must be irradiated with the light in which wavelength λ is substantially less than its size, i.e. $\lambda \ll$ d. The basis of quantum (wave) physics, operating with the particle as a wave packet, is the relation obtained between the wavelength λ and momentum p, which the particle has: $\lambda = \hbar/p$, where $\hbar = h/2\pi$ is the Planck's constant. Several machines are currently being operated throughout the world, accelerating charged particles (electrons, protons, antiprotons) to very high energies. Many active accelerators operate in the extracted beam mode when accelerated particles are directed

to a stationary target or in the mode of colliders when two particles, accelerated to high energies, collide with each other.

The centre of mass energy ($\sqrt{s}$) for fixed target experiment (proton beam hits a fixed Hydrogen target) in case of four-momentous are $p_1^\mu = (E_p, \vec{p_1})$ and $p_2^\mu = (m_p, \vec{0})$ given such as:

$$\sqrt{s_t} = \sqrt{(p_1^\mu + p_2^\mu)^2} = \sqrt{(E_p + m_p)^2 - \vec{p_1}^{\,2}} = \sqrt{2m_p^2 + 2E_p m_p} \approx \sqrt{2E_p m_p} \qquad (2.22)$$

The total collision (proton-proton collider) energy in the center of the mass system for momentous $p_1^\mu = (E_p, \vec{p_1})$ and $p_2^\mu = (E_p, \vec{p_2})$ where $(\vec{p_1} = -\vec{p_2})$ is equal:

$$\sqrt{s_c} = \sqrt{(p_1^\mu + p_2^\mu)^2} = \sqrt{(E_p + E_p)^2 - \vec{p_1}^{\,2} - \vec{p_2}^{\,2}} = 2E_p \qquad (2.23)$$

The collider mode becomes energetically more profitable when two protons, accelerated to energies of E_p, collide with each other. Figure 2-5, it is shown how the accelerator technique has been changed over time.

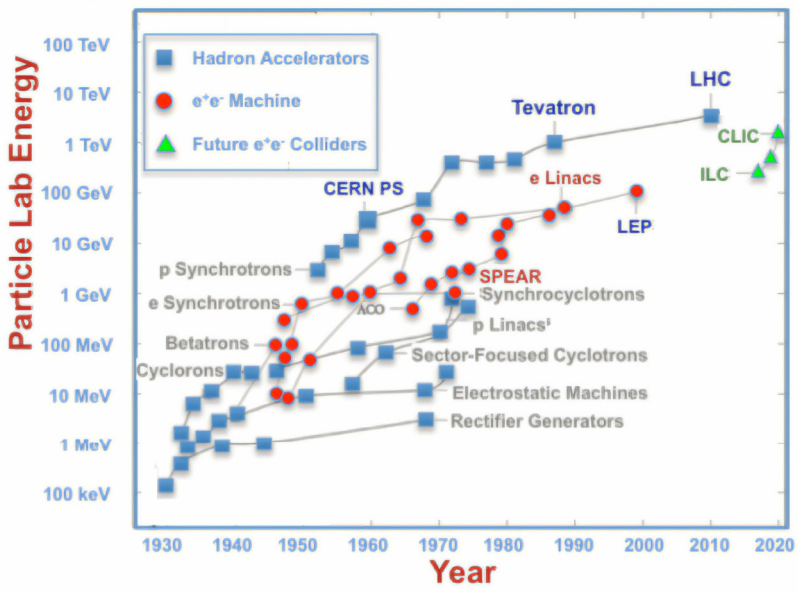

Figure 2-5: Livingston plot showing the historical exponential growth with time in the energy [90].

Thus, Figure 2-5 shows that one of the most modern accelerators is the LHC, which was built at CERN, and it has collision energy in the center of the mass system of about 14 TeV.

Chapter 3

The Acceleration Complex

3.1 The Large Hadron Collider

The Large Hadron Collider (LHC) [21] is one of the most complex experimental facilities ever created. This large complex was designed for research in elementary particle physics with nominal collision energy in the center of mass at 14 TeV. The LHC is located at CERN (Switzerland and France, near Geneva), in a 27 km radius tunnel at a depth of about 100 meters (Fig. 3-1).

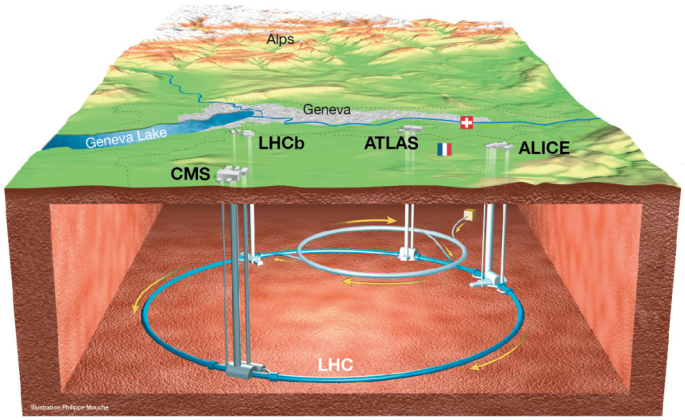

Figure 3-1: Overall view of the LHC with the location four main LHC detectors: ALICE, ATLAS, CMS and LHC [85].

The largest accelerator of this complex is the LHC, where two beams of protons can be accelerated up to 7 TeV each before they collide. For proton and ion injection, the LHC uses an SPS (Super Proton Synchrotron) accelerator with output energy of about 450 GeV for protons. Its perimeter is 6.9 km, and it is located underground at a depth of 50 m. Heavy particles in the SPS come from the proton Synchrotron PS, which in turn receives protons and ions from the booster (accelerator-injector).

3.1.1 Overview of the LHC

To describe the LHC operation, on can divide it into several sections (Fig. 3-2).

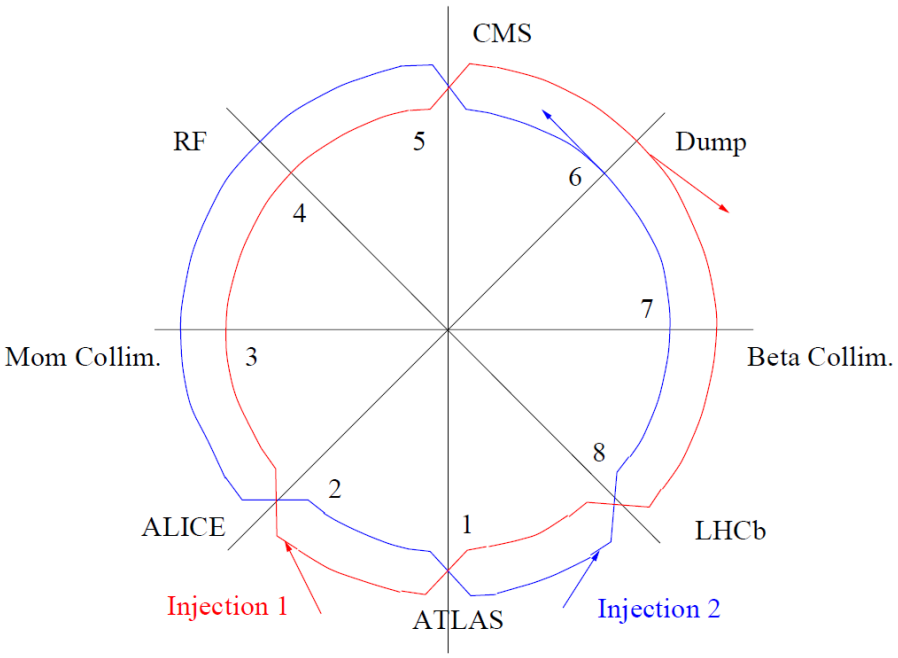

Figure 3-2: Schematic view of the LHC ring [71].

The proton beam enters into the LHC ring from the SPS booster. The proton beam in the accelerator does not at all look like a homogeneous and continuous "proton beam". It is divided into separate bunches of protons that fly one after another at a strictly defined distance. The entire LHC ring consists of eight sectors, which are marked from 1 to 8. In each section (1-2, 2-3, etc.), there are magnets in a row controlling the proton beam. Thanks to the magnetic field of these magnets, the proton beam constantly circulates, remaining inside the acceleration ring. These magnets form a circle for the protons to move along. In addition, special focusing magnets hold back the transverse oscillations of protons relative to the vacuum tubes' orbit. Two vacuum tubes run alongside each other, permitting the two opposite proton beams to circulate in opposite directions. These two tubes are combined into one only at designated points 1, 2, 5, and 8. At these points, the four main detectors are built: two versatile large detectors, ATLAS and CMS; and two specialized medium detectors, ALICE and LHCb; providing the collisions of the colliding proton beams. At point 4, there is an acceleration section. It is here that the proton beams gain additional energy with each turn during acceleration. At point 6, there is a beam injection system. If necessary, fast magnets could be installed there to lead the beams through a special channel.

3.1.2 Magnets

The LHC accelerator uses several thousand magnets of various applications to control the beams. These are the most important and the most expensive part of the accelerator. The magnets can be represented by several groups. The magnets (Fig. 3-3) that respond to keeping the beam in the orbit before the collision are called superconducting magnets. They are made of a low-temperature niobium-titanium superconductor. Each of them can hold up to 11 kA of current and produce a magnetic field with an induction of 8.3 Tesla. These powerful electromagnets stand along the entire acceleration ring and guide the proton beams through a narrow vacuum tube. It was created for the LHC using a unique technology. First, the necessity to operate the two opposite proton beams obliged to use not one but two magnets with opposite polarities under a single shell. Secondly, in order to minimize the connections between the magnets, they were made very long (15 meters). Moreover, it is worth noting that the wires were not wound around the vacuum tube but along it. This allowed the creation of a magnetic field perpendicular to the plane of the ring.

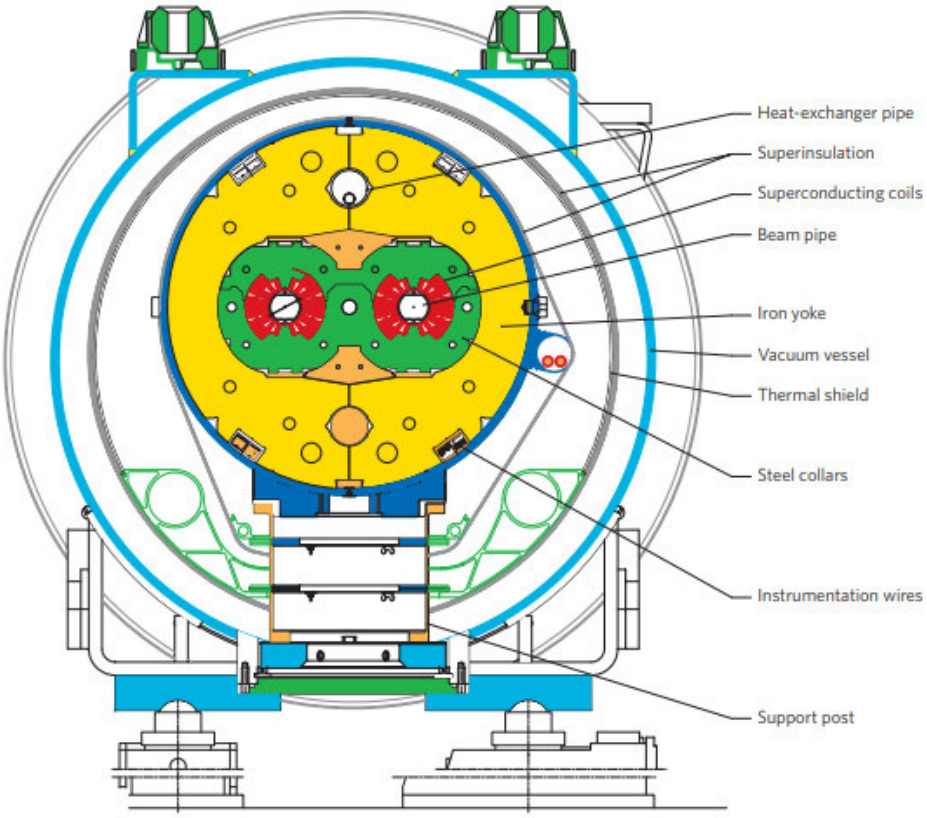

Figure 3-3: Cross-section of the main LHC magnets. In the center, there are two beam pipes separated by 194 mm. The superconducting coils (red) are held in place by collars (green) and surrounded by the magnet yoke (yellow). All these components form the magnet's cold mass, which is insulated in a vacuum vessel (outer blue circle) to minimize heat uptake from the surroundings. Image reproduced with permission [20].

Since the bunches consist of positively charged protons, they tend to disperse due to the electrical repulsion between the protons. To prevent this dispersion, the beams need to be focused. Superconductor magnets perform part of this task: the field is arranged so that particles that have deviated from the optimum trajectory return to it. However, it is very important to focus the beams as well as possible in front of collision points. The smaller the transverse focal size, the more likely protons are to collide with each other, and therefore the higher the luminosity of the accelerator. Reducing the transverse focal size by half results in a 16-fold increase in luminosity. This focusing of the beams in front of the collision points is performed by quadrupole magnets. A quadrupole magnet has an important difference with respect to a conventional optical lens, it can focus the beam in the vertical plane, defocusing it horizontally, or vice versa. Therefore, in order to focus the beam in both directions, it is necessary to use a combination of several quadrupole magnets of different effects. At the place of the proton injection into the LHC ring, as well as at the point of resetting the beam, there are special kicker magnets that carried out injection [53]. During normal operation of the LHC, these magnets are switched off and are only activated when another proton beam is "injected" into the LHC from the pre-accelerator or when the beam is removed from the accelerator. The LHC also has special magnets that ensure all the necessary tasks for the operation of the accelerator [104].

3.1.3 The Injection Complex

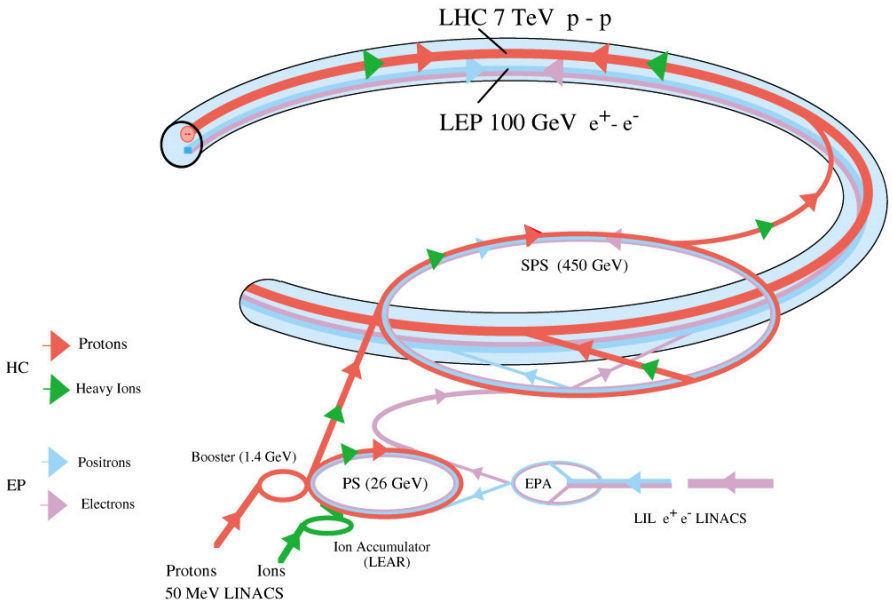

Figure 3-4: The LHC injection complex [25].

The injection of the protons into the LHC (Fig. 3-4) is not continuous but rather done in impulses. During the LHC operation, the transmission lines are empty, and

another proton portion is accumulated in the SPS pre-amplifier. At the end of each LHC operating cycle, the high-energy beam is reset, and the collider is prepared to receive a new proton portion. Before entering the SPS, the protons pass through several smaller accelerators. First, protons are extracted from hydrogen gas by ionization, then they are accelerated to 50 MeV in a linear accelerator and injected into a PSB booster. There, the protons are accelerated to an energy of 1.4 GeV, transferred to the proton synchrotron PS, accelerated to 25 GeV, and only after that they enter the SPS. The protons are accelerated up to 450 GeV and then injected into the LHC with the help of the kicker magnets. The field of kicker magnets rises to 0.12 tesla in less than 900 ns and for the duration of approximately 8 μs [9].

3.1.4 The Accelerator Section

Protons are injected into the LHC at 0.45 TeV and accelerated to 6.5 TeV while already inside the main accelerator ring. This acceleration occurs as the protons fly through several resonators. The resonator is a hollow metal chamber of complex shapes, inside which is a standing electromagnetic wave with an oscillation frequency of about 400 MHz. The efficient and homogeneous acceleration of the entire beam by a variable field is possible due to the fact that the entire beam is divided into separate parts, following at a strictly defined distance after each other. When protons pass through the resonator, the electromagnetic oscillation is in the phase where the electric field along the beam's axis pushes the protons forward. The phase of oscillation of the field in the resonator is adjusted so that at the moment of passage of particles the electric field increases rather than have the maximum value. This is done in order to equalize the energy of the accelerated particles automatically due to the effect that protons delayed will be accelerated more than protons that are moving ahead.

3.1.5 The Beam Rejection System

Typically, the beam circulates inside the vacuum chamber and does not touch the equipment. However, if a malfunction occurs in the magnetic control system or the beam deviates too far from the expected path, the beam becomes dangerous and must be reset quickly. There's a special system for all of this. It accommodates special fast magnets, which, if necessary, are activated in a few microseconds and slightly deflect the beam. As a result, protons descend from a circular orbit, and the defocused beam moves away from the accelerator through a special channel towards a separate room, made in massive carbon-composite blocks, where it is safely absorbed.

3.2 High Luminosity-LHC

To improve the ability to probe new physics beyond the Standard Model [12], the LHC will be updated so as to increase its instantaneous luminosity by 5-7.5 times, and it will be renamed as the High Luminosity Large Hadron Collider (HL-LHC). Luminosity is a way to measure accelerator performance. In this case, it is a collider parameter

characterizing the collision intensity of particles. The (instantaneous) luminosity L can be expressed as:

$$L = \gamma \frac{n_b N^2 f_{ref}}{4\pi\beta^* \epsilon_n} R; R = 1/\sqrt{1 + \frac{\Theta_c \sigma_z}{2\sigma}}, \tag{3.1}$$

where γ is the proton beam energy in units of rest mass (Lorentz boost factor); n_b is the number of bunches per beam: 2808 (nominal LHC value) for 25 ns bunch spacing; N is the bunch population; N: 1.15×10^{11}; f_{rev} is the revolution frequency (11.2 kHz); β^* is the beam beta function (focal length) at the collision point; ε_n is the transverse normalized emittance (nominal design: 3.75 μn); R is a luminosity geometrical reduction factor; Θ_c is the full crossing angle between colliding beams; and σ, σ_z are the transverse and longitudinal RMS respectively. With the nominal parameter values shown above, a luminosity of 7×10^{34} cm^{-2}s^{-1} is obtained, with an average pileup of $\mu \approx 140$ ($\mu = 19$ was the original forecast at the time of LHC approval due to uncertainties about the total proton cross-section at higher energies) [58].

As an example, the cross sections in proton-proton collisions as a function of the number of events per second for $L = 1 \times 10^{34}\ cm^{-2}s^{-1}$ is shown in Figure 3-6.

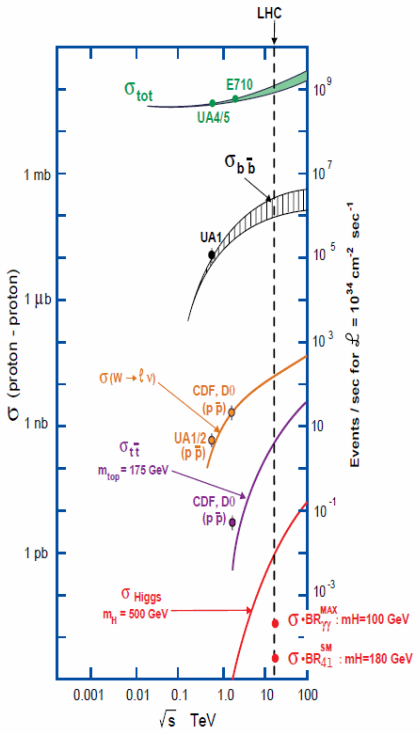

Figure 3-5: Cross sections in proton-proton collisions as a function of the center of mass energy [49].

The plan for increasing the luminosity of LHC is presented in Figure 3-6.

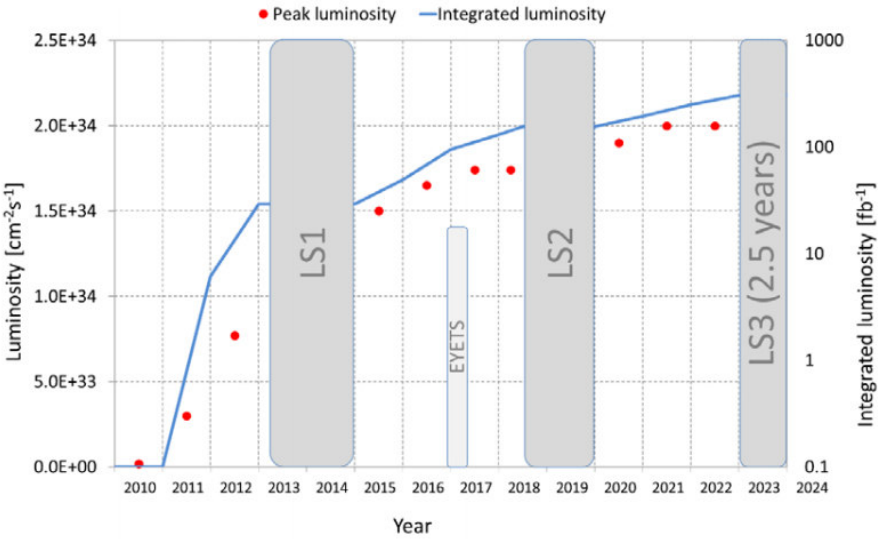

Figure 3-6: The LHC luminosity plan [58].

A possible improvement of the HL-LHC depends on several technological innovations that are extremely challenging for researchers, for instance, the installation of superconducting resonators. In order to amplify the power of the final focus lenses, magnetic elements with Nb_3Sn are used instead of traditional ones with niobium-titanium, as well as a high-temperature superconducting cable and a field of up to 16 tesla. Furthermore, handling the increased number of events would require significant upgrades to all detectors (CMS, ATLAS, LHCb, etc.) present in the LHC ring. Together, these upgrades help develop and refine the knowledge gained from the Higgs boson detection, among others, and offer a new perspective on the so-called "new physics", a more fundamental and complete theory than the Standard Model.

3.3 Experiments of LHC

The Large Hadron Collider has two large (ATLAS and CMS) and two medium (ALICE and LHCb) experiments, as well as several small scale experiments. Each of the large and medium detectors are located in a dedicated underground chamber; their position in the accelerator ring is shown Figure 3-1.

ALICE

A Large Ion Collider Experiment (ALICE) [6] is optimized for heavy nuclei collisions. Its dimensions are 26 meters long and 16 by 16 meters across. The total mass of the detector is 10 thousand tons. The pattern of the quark-gluon plasma flare is very different from that of the collision of two protons. Collisions of heavy nuclei have their specifications that achieved ALICE. When the quark-gluon plasma expands and cools down, thousands of particles are formed, but their energies are selectively (up to a

few GeV). Thus, the production of high-energy particles in such collisions becomes less probable than in the collision of protons. In studying the collision of the nuclei, particle identification becomes increasingly important. Particles that not play a very prominent role in proton collisions now come to the forefront as they provide a glimpse into the very center of quark-gluon plasma, which allows us to study Quark-Gluon Plasma (QGP) and features of heavy-ion physics such as high-pT particles, jets and heavy flavors in heavy-ion collisions [119].

LHCb

Components of the Large Hadron Collider beauty (LHCb) [10] are optimized for B-meson study. The most interesting thing about B mesons is that they are the strongest manifestation of a very important phenomenon (CP-violation) [17]. This phenomenon leads to a slightly different pattern of particle and anti-particle decay. This, in turn, has a direct bearing on the origin of our world. The LHCb detector looks like a cone where collisions of counter-rotating beams occur at its tip. It can track only those particles which are ejected at a small angle (not exceeding 15 degrees) with respect to the axis of the beam, where the majority of B mesons is expected. The detector has a length of 21 meters and a weight of 5600 tons.

CMS & ATLAS

Compact Muon Solenoid (CMS) [29] and A Toroidal LHC ApparatuS (ATLAS) [4] use classic multi-purpose detector scheme. There are track sub-detector for the determination of particles trajectories in the center detector, then calorimeters for measuring the energy of particles, and outside there are specific detectors for the registration of muons. All these sub-detectors are immersed in a strong magnetic field directed along the beam axis. This field curves the trajectories of particles that allow calculating their impulses by this curvature. The ATLAS detector is unprecedentedly large, with a moderately strong magnetic field. Having the moderately strong magnetic field in the ATLAS detector means that the internal detector must be quite large. As a result, only the internal detector is placed in the central ATLAS solenoid, and the calorimeters are based outside of it. Thus, the muon chambers are located at an even larger radius, and a separate magnetic field must be created for them. The CMS detector is different. A powerful magnetic field can only be achieved with a moderately compact magnet, a single magnet for internal detectors, and external muon chambers. Hence, the muon chambers have to stand directly outside the solenoid, while the calorimeters have to be placed directly inside the solenoid, so the given layout allows us to avoid material that acts as preshower between tracker and calorimeter but this affect to trajectories of particles. As a result, the calorimeters' dimensions become critical, which means that very heavy materials have to be used. In general, the detector is very heavy, and reliable mechanical support of its weight in such tight spaces is also a non-trivial engineering task.

The main success of ATLAS and CMS experiments was the discovery in 2012 of the Higgs boson (Fig. 3-7).

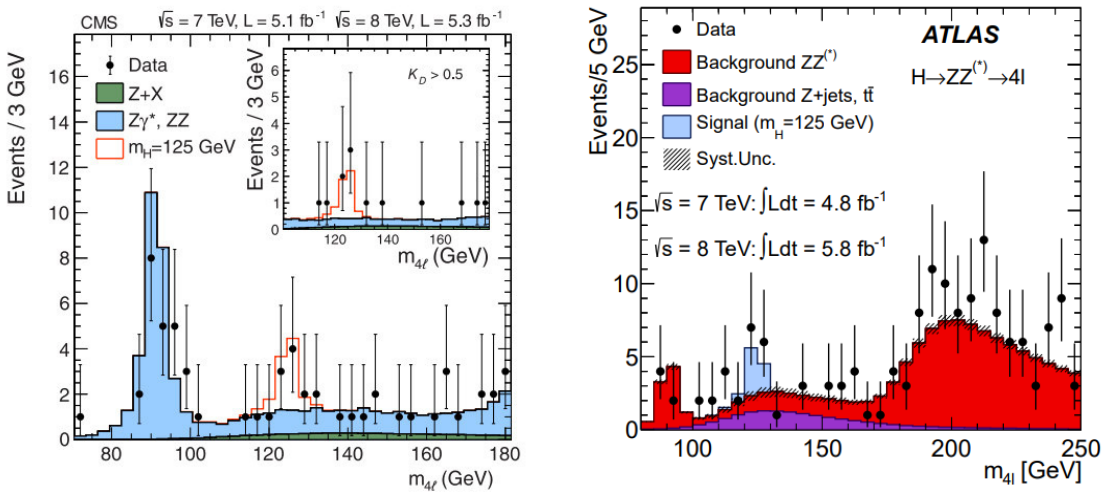

(a) (b)

Figure 3-7: (a) Distribution of the four-lepton invariant mass for the ZZ → 4l analysis in CMS detector. The points represent the data, the filled histograms represent the background, and the open histogram shows the signal expectation for a Higgs boson of mass $m_H = 125$ GeV, added to the background expectation. The inset shows the m_{4l} distribution after selection of events with $K_D > 0.5$, as described in [30]. (b) The distribution of the four-lepton invariant mass, m_{4l}, for the selected candidates in the Atlas detector, compared to the background expectation in the $80 - 250$ GeV mass range, for the combination of the $\sqrt{s} = 7$ TeV and $\sqrt{s} = 8$ TeV data. The signal expectation for a SM Higgs with mH = 125 GeV is also shown [5].

3.4 The Compact Muon Solenoid

The Compact Muon Solenoid (CMS) is one of the two large universal detectors located to the north of the LHC center. The detector is 25 m long and 15 m in diameter (Fig. 3-8). The CMS is more "compact" than the other large detector on the LHC, ATLAS (length 43 m, diameter 22 m) [35], but it is very heavy (15 kt). CMS has a huge and powerful superconducting magnet covering the tracker and calorimeters and a huge silicon tracker with a radius of 1.2 meters.

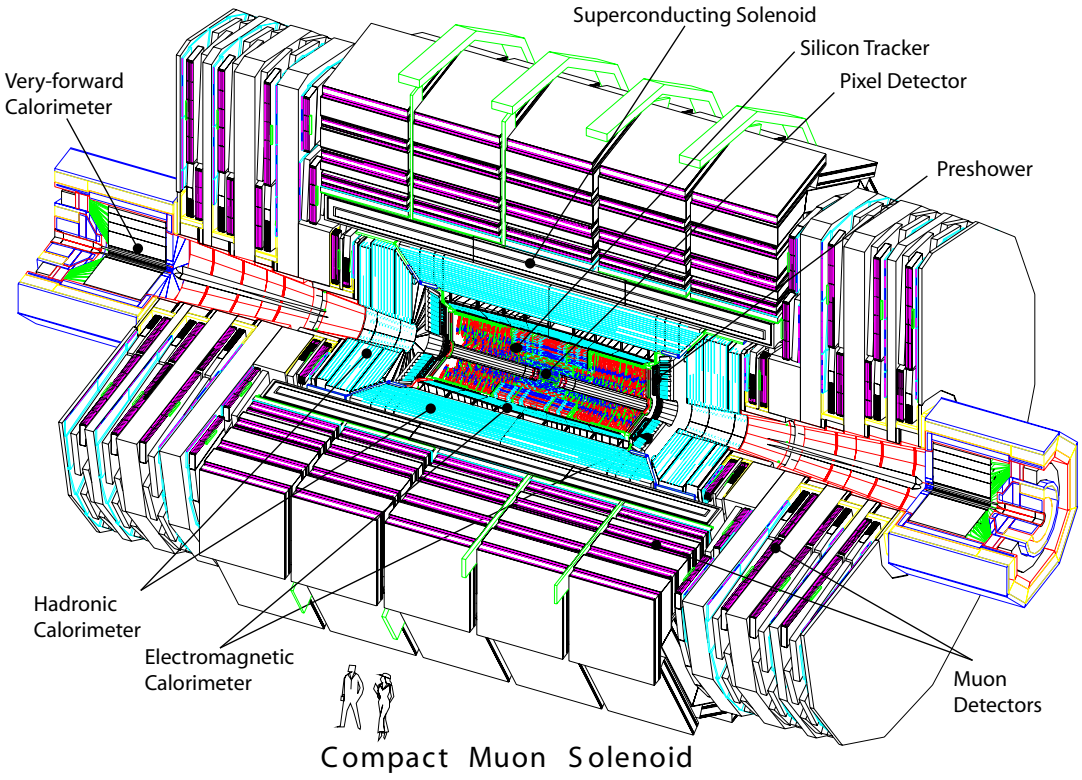

Figure 3-8: Overview of the Compact Muon Solenoid complex [14].

3.4.1 The CMS Layout

The cross-section of the CMS detector sector is depicted with a sequence of detectors (Fig. 3-9). There are several layers of trackers, followed by electromagnetic and hadronic calorimeters, a magnetic solenoid and then a massive yoke of the magnet with muon chambers.

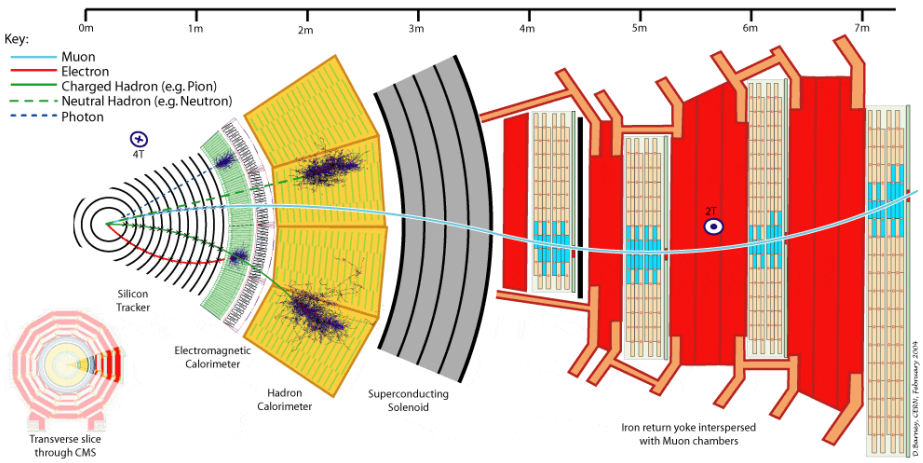

Figure 3-9: Overview of the cross-section of the CMS [14].

The center of the CMS coordinate system is the collision point. Neglecting the small tilt of the LHC plane, in the coordinate system, the x-axis is horizontal, pointing south to the LHC center, the y-axis is vertical pointing upwards, and the z-axis is horizontal pointing west. The polar angle (θ) is measured from the positive z-axis, and the azimuthal angle (ϕ) is measured from the positive x-axis in the x-y plane. The radius (r) denotes the distance from the z-axis. However, the particles produced by proton collisions are strongly dependent on the collision axis and distributed over the angle (Θ). The convenient coordinate for detectors is called pseudorapidity [45]. Pseudorapidity (η) is defined as:

$$\eta = -ln[tan\frac{\theta}{2}] \tag{3.2}$$

The traces of different types of particles and the avalanches they create are detected in trackers and calorimeters. The magnetic field directions inside and outside the superconducting coil are opposite, so the muon tracks are in the form of the s-curves. Other particles that are visible in the detector are stopped in the calorimeters.

3.4.2 The Solenoid Magnet

The key element of CMS is the heavy superconducting magnet (Fig. 3-10), which is the largest superconducting electromagnet ever created. It generates a $\sim$ 4 tesla magnetic field inside of a 6 m diameter, 12.5 m long cylinder. The total energy stored in such an electromagnet is 2.6 GJ [26]. Its design is similar to the design of a usual electromagnet with a core but "turned inside out". Instead of an inner iron core, it has an outer iron yoke, which prevents the magnetic field lines from diverging in space. Thanks to this design, a single electromagnet creates a strong magnetic field both inside and outside of the cylinder. The magnet is maintained at liquid helium temperature. The track detectors and calorimeters are placed inside the cylinder, and the outer field is used to deflect muons. As a result, when a muon leaves the center of the detector and flies through the field, it is deflected first in one direction and then

in the other. The yoke also serves as a filter in which muons interact and lose energy.

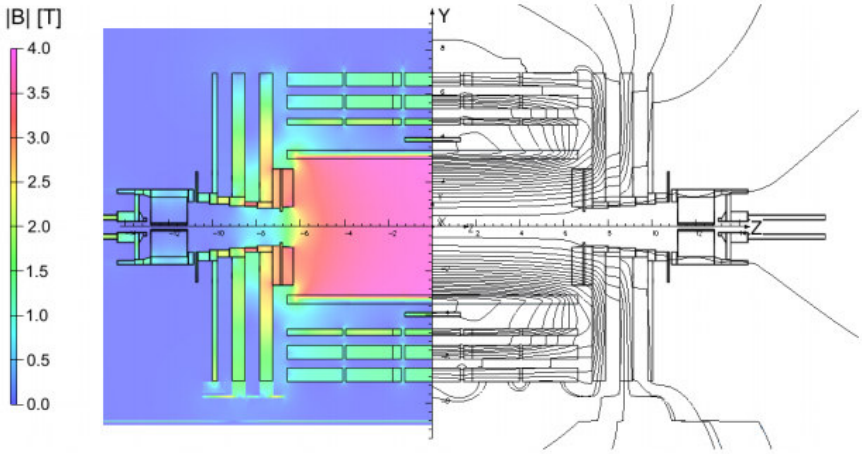

Figure 3-10: Value of |B| (left) and field lines (right) predicted on a longitudinal section of the CMS detector, for the underground model at a central magnetic flux density of 3.8 T. Each field line represents a magnetic flux increment of 6 Wb [31].

3.4.3 The Tracker System

The track detectors in the CMS detector follow a classic pattern [27]. The closest to the vacuum tube is the pixel detector. Within its volume, the particle flow is high. At a distance of 8 cm from the beam, an area of 1 cm^2 counts more than 10 million particles per second. The tracker consists of two subsystems: the pixel tracker and the strip tracker.

A general overview of the CMS tracker system is given in Figure 3-11, with its subsystems: Pixel, Tracker Inner Barrel (TIB) and Tracker Inner Disks (TID), Tracker Outer Barrel (TOB) and Tracker Endcaps (TEC).

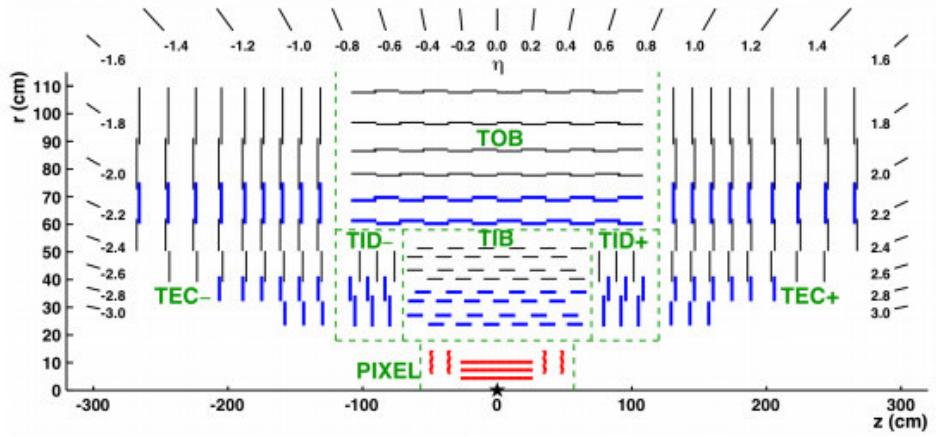

Figure 3-11: Schematic view of the CMS tracking detector [106].

The pixel detector consists of three cylindrical layers with radii of 4, 7 and 11 cm and contains 66 million 100×150 μm pixels (Fig. 3-12). In 2017, the new pixel detector was installed with an additional fourth layer of pixel modules in the barrel and a third disk per side in the Endcap region. The number of channels has almost doubled (from 66 million to 124 million), giving a four-hit covering in the whole tracking region up to $\eta = 2.5$ [100].

The Silicon Strip detectors are divided into the inner barrel part (TIB), the inner disks (TID), the outer barrel (TOB), and outer Endcaps (TEC). The TIB and TOB are composed respectively of four and six concentric layer barrel shell structures. The TID system is made of three disk structures on each side, each divided into three concentric rings, while the TEC is made of nine disk structures on each side, each made of four to seven rings. The detector contains more than 15 thousand individual modules of different designs, together with millions of sensitive strips, which are read out by thousands of data collection channels [13].

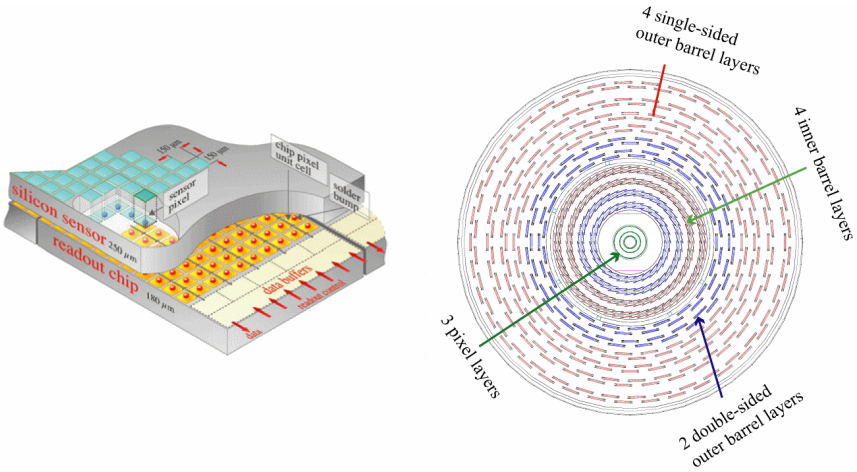

Figure 3-12: Left: The CMS silicon pixel detector. Right: The CMS tracker layers are shown in the plane perpendicular to the beam [51].

The strip detector is maintained at -20 $^{\circ}$C to optimize performance. Once the received signals are processed by the front-end electronics (electronics attached directly to the ends of the detection modules), the data is converted into an infrared laser sequence. The output signals from the detector pass through 40 thousand fiber channels.

3.4.4 The Calorimeter System

Two types of calorimeters are installed in the CMS detector. The electromagnetic (internal) one is responsible for measuring the energy of electrons and photons, and the hadron (external) one is built for measuring hadron energy (Fig. 3-13).

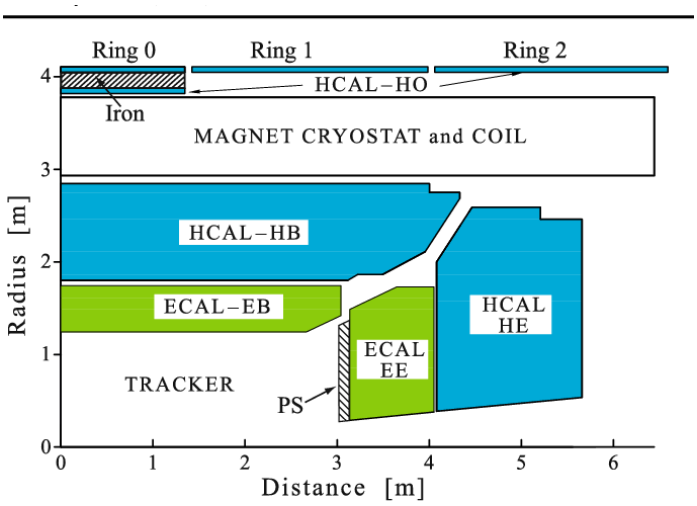

Figure 3-13: Location of the hadron calorimeter in and around the CMS magnet. HCAL HB and HCAL HE are the hadron calorimeters. ECAL EB and ECAL EE are the electromagnetic calorimeters and PS is preshower detector [46].

The homogeneous electromagnetic calorimeter (Fig. 3-14) of the CMS detector complex contains ≈ 76000 tungsten lead crystals ($PbW0_4$) out of which ≈ 61000 are in the cylindrical part (barrel) and ≈ 15000 on both ends. The size of the crystals is $2.2 \times 2.2 \times 23$ cm in the barrel and $3 \times 3 \times 22$ cm at the ends. The advantage of this material, compared with other scintillators, is that electrons and photons are developed within a very short distance. The crystals are located in carbon or glass fiber matrices, forming the so-called supermodules and super crystals.

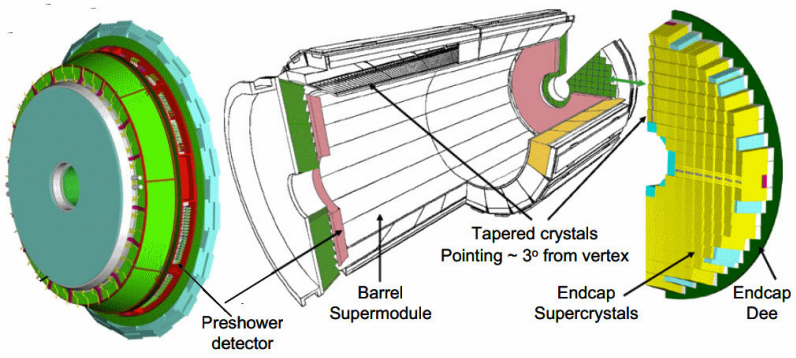

Figure 3-14: Schematic view of the CMS ECAL. It is 7.9 m long, 3.6 m in diameter, with a crystal mass of 90 t. Schematic view of the CMS ECAL preshower [34].

This calorimeter is able to distinguish a single high-energy photon from a pair of photons born from the decay of neutral high-energy pions. Single high-energy photons are rare, but they indicate that the Higgs boson disintegration into two photons. On the contrary, neutral pi-mesons are abundant, and in the vast majority of cases do not carry any particularly interesting information. However, π^0 mesons with short

lifetime also disintegrate into photons, and the signals from the two photons can be detected and simulate photons from the Higgs boson disintegration. An electromagnetic calorimeter may not be able to distinguish these events. To solve this problem, a thin layer of a special preshower [82] photon detector is installed in the end segments of the CMS, just in front of the electromagnetic calorimeter. This detector is made using silicon strip detector technology, so the size of the sensitive cell in it is only two millimeters (to be composed with crystals with a cross-section of 3 by 3 cm in the electromagnetic calorimeter). This is a disk with a 50 cm diameter hole in the middle for the beam pipeline. The disk is only 20 cm thick, but it consists of two layers of lead absorbers, between which there are silicon sensors with electronics. The preshower detector [111] is located at the ends, where the angle between the directions of the two decay photons is expected to be small (Fig. 3-14). The preshower detector has a significantly better granularity than the electromagnetic calorimeter. This detector can distinguish two photons separated by several millimeters as two separate particles. When the photon passes the lead absorber, it causes an electromagnetic downpour that includes electron-positron pairs, which are detected by the sensor.

The CMS Hadron Heterogeneous Calorimeter (Fig. 3-15) consists of central (Barrel HB), outer (HO), rear (Endcap HE), and front (HF) sections. HB and HE calorimeters are in the solenoid field. The HF-forward calorimeter sections are located at both ends of the CMS. The HB Calorimeter consists of 36 individual "wedges" each weighing 26 tonnes, plus other 36 slightly smaller wedges mounted on the HE Calorimeter. Brass is used in the HB and HE calorimeters. The thick (5 cm) brass strips are used in the HB Calorimeter, and 8 cm thick strips are used in the HE Calorimeter. They are layered with sensitive plastic scintillator cells leading to a total of 8000 reading channels. Since the HB Calorimeter may not be thick enough to contain the hadron shower, it is expected with another HO Calorimeter is made by adding scintillation tiles after the first muon absorber.

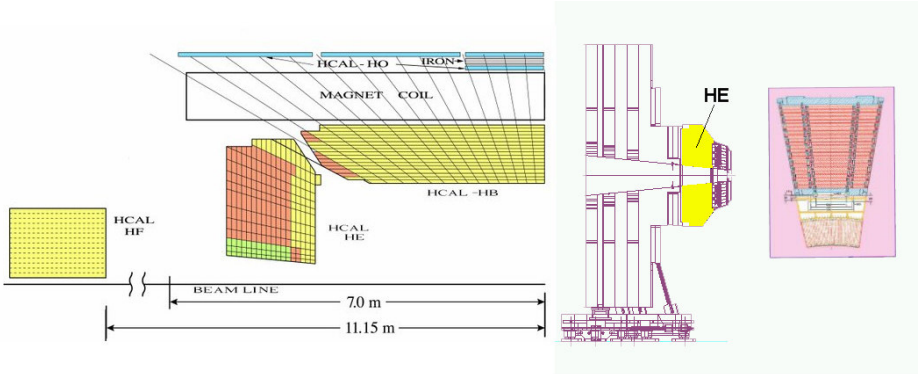

Figure 3-15: Generic view of the hadron calorimeter moved outside the magnet and the HCAL module showing sampling layers. Quarter view of the CMS hadron calorimeter. The shading indicates the optical grouping of scintillator layers into different longitudinal readouts [28].

As sensitive material, it uses fibers embedded in a steel absorption matrix. Light signals from scintillators are read by wave shifting fibers and then transmitted into

hybrid photodiodes or micro-pixel avalanche photodiodes via optical fibers.

3.4.5 The Muon System

The muon chambers are located outside the solenoid, alternating with the layers of the iron yoke. A schematic view of the CMS Muon spectrometer is reported in Figure 3-16. The barrel region is divided into five wheels, and the two Endcaps are made of three iron disks and four stations, which are divided into two or three rings.

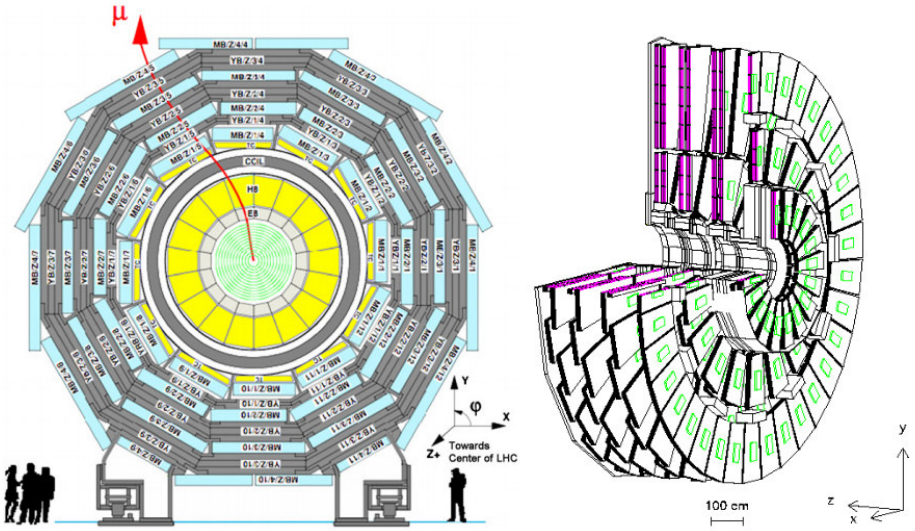

Figure 3-16: Left: Transverse view of a CMS barrel yoke wheel. Right: CMS Endcap Muon System [55].

The CMS detector uses three types of muon detectors: drift tubes, cathode strip chambers and resistive plate chambers. Some of these detectors are designed to determine the coordinates and the time when muons pass, while others are used for a fast muon trigger that should decide in real time whether or not the event is interesting from a muon perspective.

Drift Tubes

The Drift Tubes (DT) (Fig. 3-17) muon barrel system contains 250 drift tubes organized in five wheels [109]. The tubes are filled with gas (85% Ar + 15% CO_2) and contain positive voltage wires (anodes). The gas composition and the tube are optimized so as to provide a linear dependence of the drift time on distance. Single wire measurement resolution is of the order of 200μm and maximum drift time about 380 ns. A super layer is formed from four layers of parallel drift tubes. The chamber (2 m $\times$ 2.5 m) consists of two superlayers for measuring r $-$ ϕ coordinates and one layer perpendicular to them for measuring r $-$ Z coordinates. The DT were chosen to cover the pseudorapidity region up to $|\eta| > 1.2$ [37].

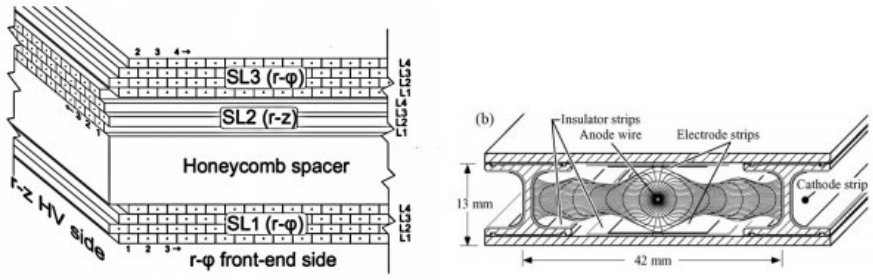

Figure 3-17: Left: Schematic view of a DT chamber. Right: Section of a drift tube cell showing drift lines and isochrones [44].

Cathode Strip Chambers

The Cathode Strip Chambers (CSC) (Fig. 3-18) are multi-wire proportional chambers, which consist of six planes of anode wires and, perpendicular to them, seven planes of cathode strips. Cathode strips are trapezoidal in shape ($\Delta\phi$ = const). A gas mixture ($40\%\ Ar + 50\%\ CO_2 + 10\%\ CF_4$) is used in the chambers; as the muons fly through the chamber, gas atoms are ionized and the electrons, which flow to the anode wires and creating an electronic avalanche. An avalanche around the anode induces charges on cathode strips that are about half as wide as the distance between the anode and the cathode. As the wires and strips are perpendicular, two-dimensional spatial information is taken from the CSC strip. The cathode strip chambers provide measurements of ϕ-coordinates of muon tracks with an accuracy of $\sim 100\ \mu$m, while time resolution is of the nanosecond order [36].

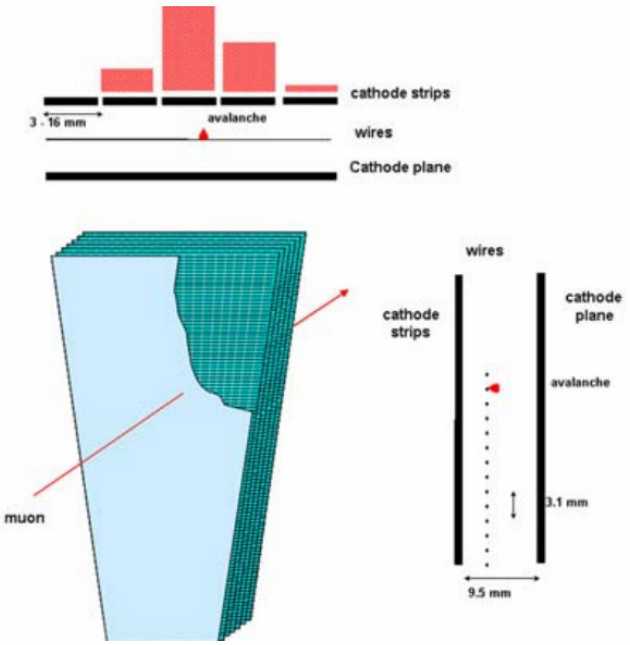

Figure 3-18: Principle of operation of a CSC Endcap muon chamber in CMS [68].

In total, the CSC system includes more than 500 muon chambers that contain approximately 2.5 million wires grouped in ≈ 211k anode reading channels. In addition, there are ≈ 270k cathode channels. The muon stations (ME1-ME4) are formed from cathode stripe chambers. The total area covered by the cathode strip chambers is approximately 1000 m^2.

Resistive Plate Chambers

The Resistive Plate Chamber (RPC) is based on gas ionization. When a charged particle passes through the chamber, it undergoes a series of stochastic interactions with atoms and molecules, transmitting some of its energy. This energy is then dissipated by the creation of an ion-electron pair and photon emission. These photons and electrons can then ionize other atoms and so on. The multiplication of electron-ion pairs stops when the emitted particles' energy becomes smaller than the ionization potential of the atom.

The Resistive Plate Counter was developed in the early 80s of the 20th century [102]. This chamber consists of two parallel electrode plates which are manufactured with a bulk resistivity made of bakelite ($10^{10} - 10^{11}$ Ω cm) [59] or glass [80], separated by a gas gap of a few millimeters (Fig. 3-19).

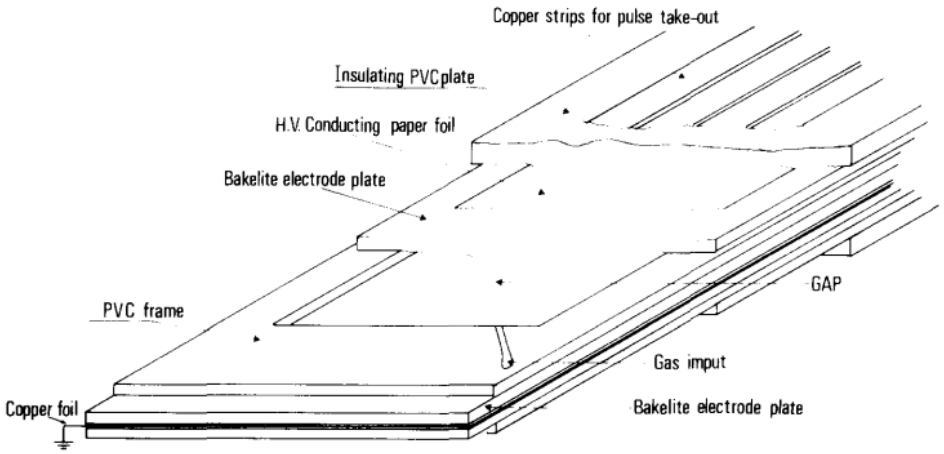

Figure 3-19: Sketch of the Resistive Plate Chamber [102].

The CMS RPCs have a double-gap with resistive plates operating in the avalanche mode (See Ch. 4.2.1). Their main task is to serve as quick triggers for the muon system. The time between successive intersections of LHC is 25 ns. The fast response time of the RPC allows an event to be uniquely associated with the muon track's intersection under the high load and large background conditions typical for the LHC. The RPC signals provide time, and coordinate measurements ($\Delta x \sim 1$ cm) that are accurate enough to effectively select events of interest in the environments where particle flows can reach 10^3 Hz/cm^2.

The RPC module contains four dielectric plates (Bakelite), which are 2 mm thick each. There are two gas gaps between them, which are also 2 mm thick each. Bakelite plates serve as electrodes. The signal is read out from strips, which are located

between the pairs of Bakelite plates. The chambers are equipped with Front-End Boards (FEB), which operate with a threshold of 220 mV $\approx$ 150 fC [18]. The main parameters of the current RPC are summarized in Table 3-20 and a schematic view of the barrel and the Endcap chamber is shown in Figure 3-21.

Table 3-20: Main CMS RPC parameters.

Number of Gaps	2
Gas mixture	$95\%\ C_2H_2F_4, 4.5\%\ iC_4H_{10}, 0.3\%\ SF_6$
Thickness	$2\ mm$
Resistivity	$1 - 6 \times 10^{20}\ \Omega cm$
Rate capability	$300 Hz/cm^2$
Efficiency	$> 95\%$
Time resolution	$1.5\ ns$
Intrinsic noise	$< 5\ Hz/cm^2$

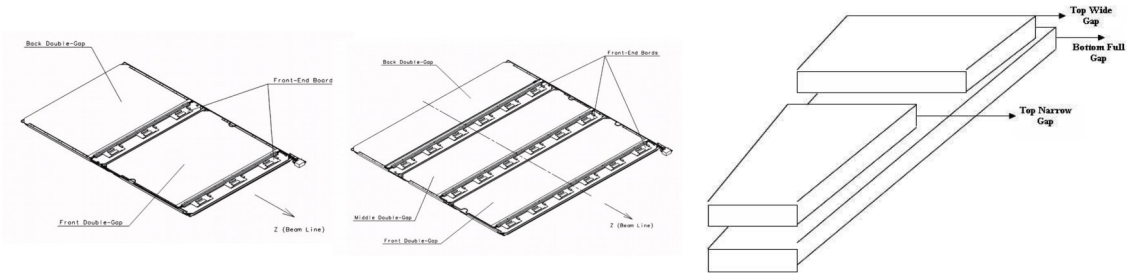

(a) (b)

Figure 3-21: (a) RPC Barrel Eta Partitions (Rolls). (b) Gap segmentation of CMS Endcap RPC [3].

The CMS consists of 1056 RPCs (Fig. 3-22) organized in four stations covering the range $|\eta| < 1.2$ in the Barrel area and four stations in each Endcap covering $0.9 < |\eta| < 1.9$.

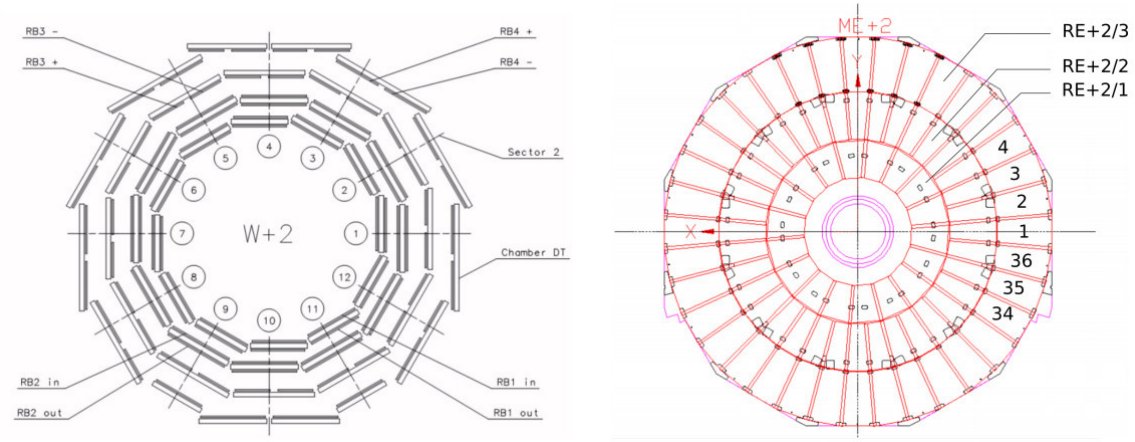

Figure 3-22: Left: Transverse view of the muon system layout in the barrel region, showing the positions of the DT and RPC stations [38]. Right: Layout of the RPC Endcap stations [113].

In the detector's cylindrical part, chambers are mounted as cylinders surrounding the beam axis and located in parallel to the drift tube modules. In the end part, these chambers are placed on parallel disks. The chambers are trapezoidal and are overlapped at an azimuth angle, providing continuous coverage [95]. Operating RPCs have stable performance and average efficiency within 95% (Fig. 3-23).

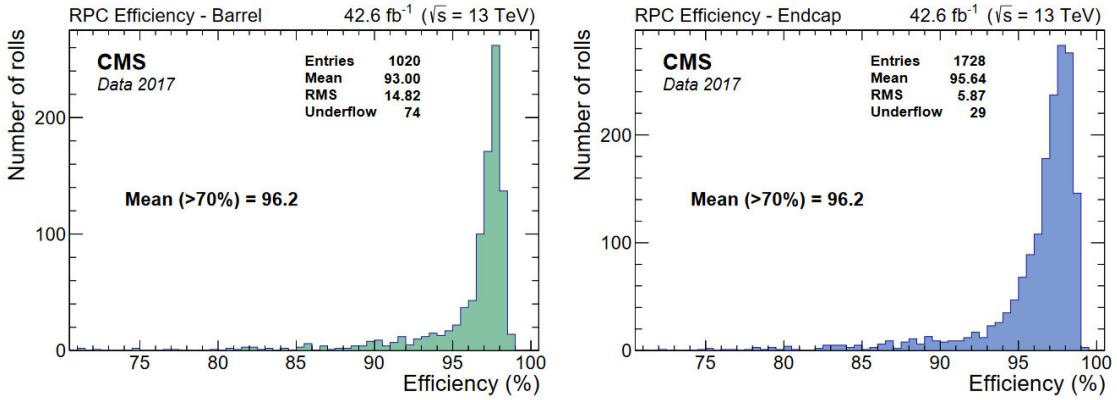

Figure 3-23: Overall efficiency in the Barrel (left) and Endcap (right) during the 2017 data taking [62].

3.4.6 The Trigger System

The L1 trigger from muon and calorimeter are then combined in the (L1) trigger (Fig. 3-24). The L1 trigger is operated at the beam collision frequency (40 MHz). The electronics read and store data in a buffer memory of 128 collision events or 3.2 μs. Thus, the trigger system has 3.2 μs to decide whether to transmit data to the next level of data processing or not. Every 25 ns, a new event is buffered from

the calorimeter. The muon and calorimeter's L1 trigger is then combined into an L1 Global Trigger (GT), which decides whether to transmit or reject the event. The data is temporarily stored in the processing element, pending a decision on whether or not to store it. This system is based on ASICs to ensure the fastest possible processing of raw data.

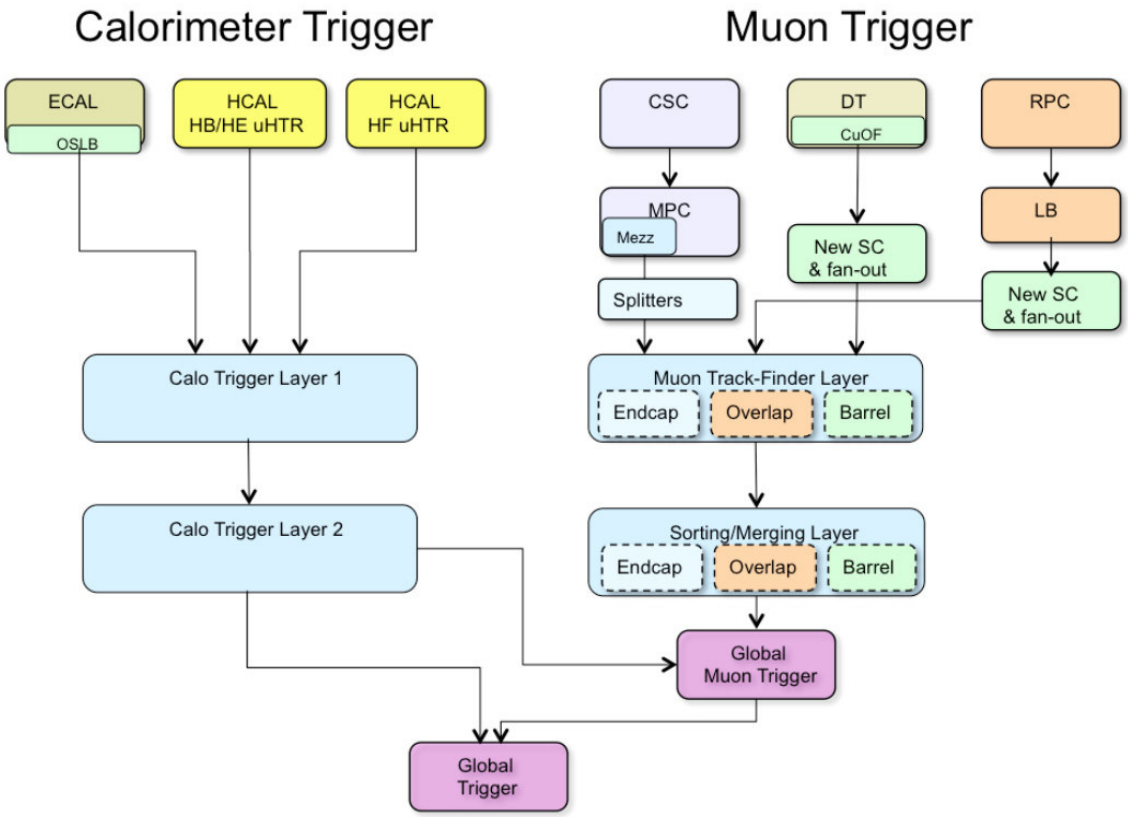

Figure 3-24: Diagram of CMS trigger [107].

The events that meet the L1-trigger requirements are selected and transmitted to the High-Level Trigger (HLT) [107, 7]. HLT is a software-oriented system implemented in the computing complex. HLT can be used to reconstruct objects of physics such as jets, leptons, etc. To pass the HLT, an event must satisfy at least one of its paths, which are on the list. HLT events are recorded permanently on a disk by the Data Acquisition System (DAQ) for further physics analysis and transfer to CERN Tier 0 in one or more data streams.

3.5 The CMS Upgrade Project for HL-LHC

The projected increase in luminosity in the HL-LHC period will require upgrading many CMS systems, which is a challenge [41]. The LHC will reach a luminosity of 7.5×10^{34} cm^{-2}s^{-1} with a pileup of about of 200 collisions. Integrating over 3000 fb^{-1} throughout the full experimental life time with the expected luminosity will impose

serious conditions on all the components because of the higher response speed, more complex reconstruction of events, and accelerated aging of all components due to high background. The real-life event had an average pileup of roughly 100 during the special HL-LHC run in 2016 with individual high intensity bunches (Fig. 3-25).

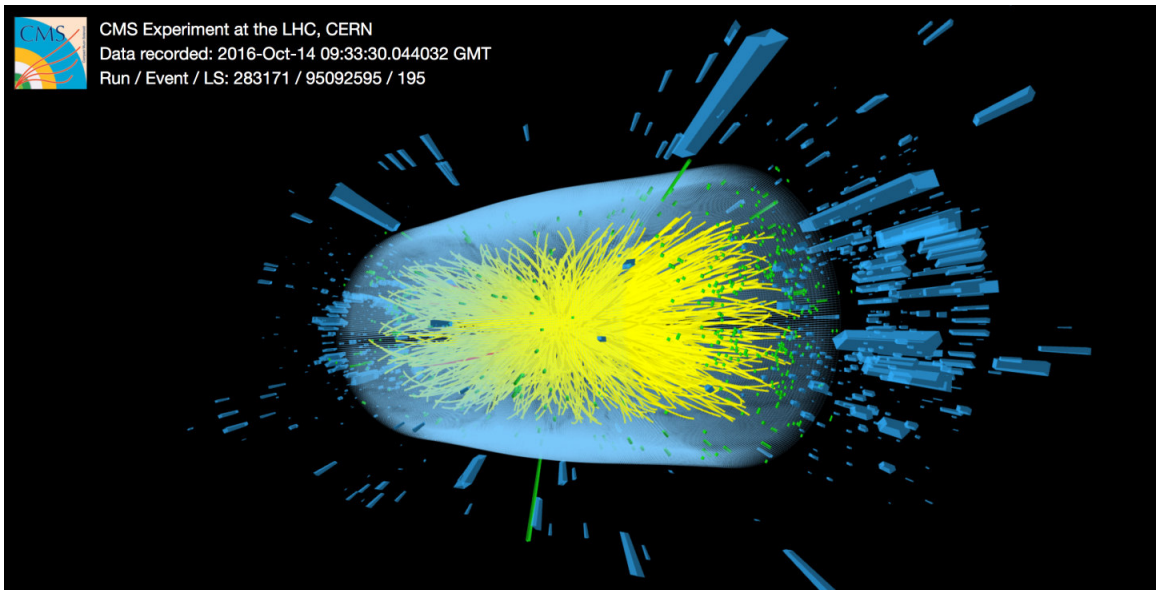

Figure 3-25: The proton-proton collisions at a center-of-mass energy of 13 TeV were recorded during the high pileup fill of Run 2. The events are from isolated bunches with average pileup roughly around 100 [43].

To ensure an improved performance at significantly higher collision rates, the CMS experiment needs to be upgraded. The main objective of the CMS upgrade experiment is to achieve an excellent performance of the detector subsystems in terms of optimized particle reconstruction (resolution, efficiency, etc.) [47].

The ability of both the tracks and the pixel system to analyze data will be quadrupled. The new module will also provide information on the 40 MHz L1 trigger for tracks with pT $>$ 2GeV/s, providing a meaningful power-down at the earliest stage of the event selection. The pixel system will implement smaller pixels and thinner sensors for improved impact resolution and better two-track separation [42].

The replacement of electromagnetic and hadron calorimeters for LC3 was planned due to the possibility of radiation damage. The new calorimeter shall be called the High Granularity Calorimeter (HG-Cal). Its electromagnetic sensor would consist of 28 tungsten wafers left with silicon sensors as an active material [40, 39].

As for the first level trigger (Fig. 3-26), improvements are planned in the electronics of the calorimeter trigger, the muon trigger, and the global trigger.

Phase II requires a higher reception speed of L1 to cope with HL-LHC luminosity without increasing the trigger thresholds. For this purpose, the electronics of some existing subdetectors will need to be upgraded. The frequency of data entry into the performance is estimated to be 5 kHz (7 kHz), with 140 (200) heaps of events. The L1 will also have trajectory information, which will help discard background noise

from the beginning of the event selection. A brand new L1 for calorimeters and the muon spectrograph will also be put into operation.

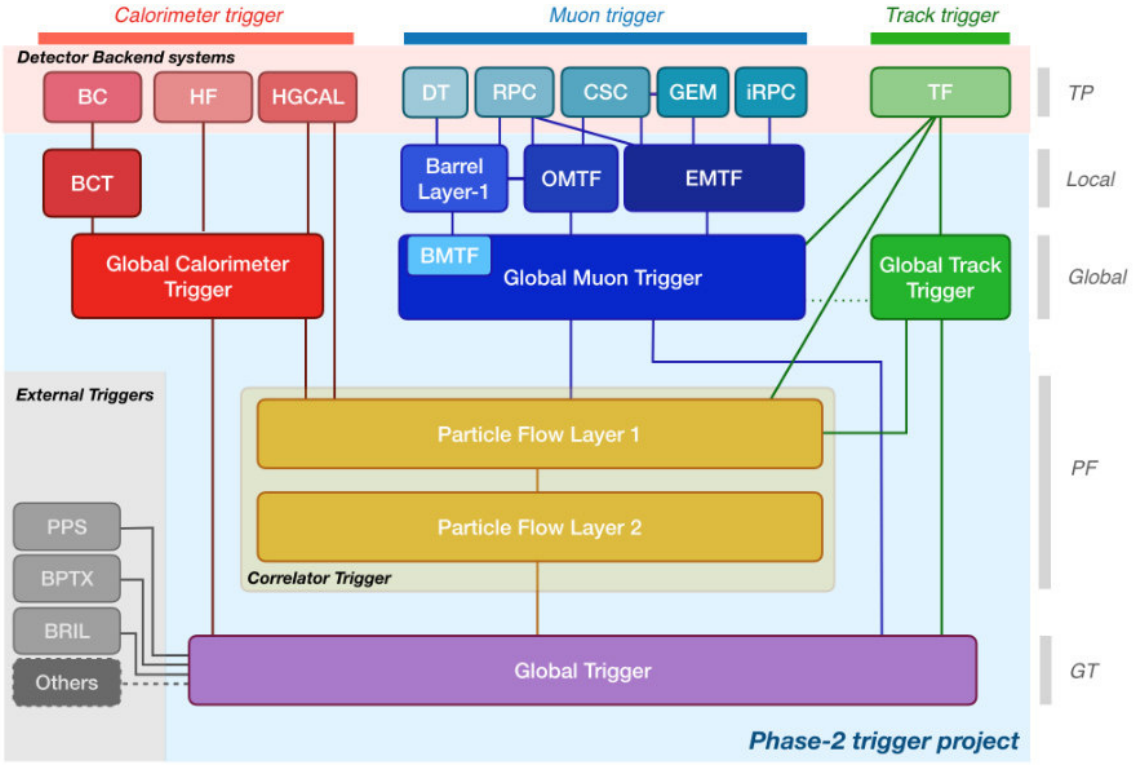

Figure 3-26: Functional diagram of the CMS L1 Phase-2 upgraded trigger design [2].

Modernization of the muon system has been the subject of numerous studies collected in TDR [41]. The conducted aging tests show that most of the muon tracker chambers will be able to withstand the HL-LHC environment until the end of Phase 2 without significant loss of efficiency. The measurements made on the detector indicate that the DT can withstand the hit rate expected during Phase II. Concerning CSC, it is assumed that they can be used until the HL-LHC is complete. While the CSC modules are expected to perform satisfactorily throughout the HL-LHC program, some electronic CSC front-end boards will need to be replaced to cope with more stringent trigger requirements. Overall, the new boards will be able to deal with the higher L1 response speeds due to the use of high-performance optical links and processors. Moreover, two superstations (GE1/1, GE2/1, ME0) will be installed with the gas electron multiplier: GEMs are gas detectors characterized by a spatial resolution of the order of ≈ 100 μm, and a time resolution in the order of ≈ 8 ns per efficiency plateau for Ar/CO_2 (70/30) as a gas mixture. When combining three foils to a triple GEM chamber, the gas gain reaches the value of the order of 10^4.

The RPC upgrade program includes the commission of all chambers and the installation of two new stations (RE3/1, RE4/1) with improved RPC. The existing RPC system is read with a 40 MHz frequency, synchronized with LHC beam crossings, which is higher than the chamber resolution (1.5 ns). The new system will record hits with time resolution of about 1 ns or even better. In particular, this improvement

allows suppressing the noise coming off the bunch crossing time and facilitates due synchronization of the RPC system. The number of hits measured per track would be increased with the help of two new stations (RE3/1, RE4/1) of RPC detectors to improve the muon system's redundancy and obtain a solid track. The equipping of these zones was planned from the beginning of the CMS, but was not carried out due to the large particle fluxes present in this region. These two stations could help ensure muons detection even if one or more CSC fail. Although CSC can identify and trigger muons with high efficiency, these chambers are less efficient in some areas due to the dead zones (not equipped with sensitive material). By including RPC hits in the trigger, the performance (Fig. 3-27) in these areas can be restored. It is also possible to eliminate the ambiguity of CSC hits (ghosts) at trigger level L1.

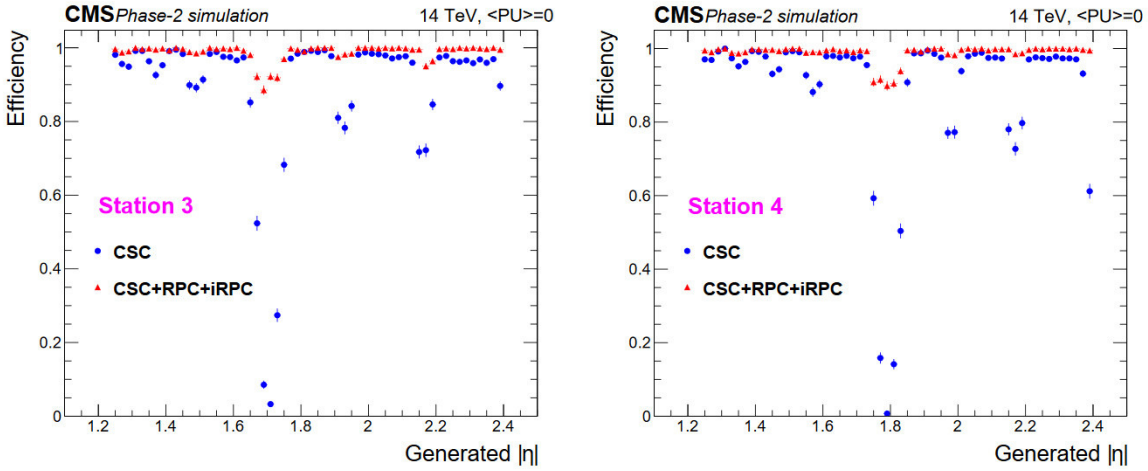

Figure 3-27: Impact of RPC hit inclusion on the local trigger efficiency in station 3 (left) and station 4 (right) [41].

Chapter 4

Improved Resistive Plate Chambers

The CMS upgrade program (See Ch. 3.5) includes, among others, the installation of two additional stations in the Endcap region (Fig. 4-1). These stations will be equipped with a new generation of RPC. The improved RPC (iRPC) will combine an upgraded gas detector version with front-end electronics equipped with a high precision timing. This improvement will make it possible to determine the position of the hits along the strip, improve the absolute time resolution as well as the detector rate capability compared to the RPC chambers currently used in the CMS (See Ch. 3.4.5).

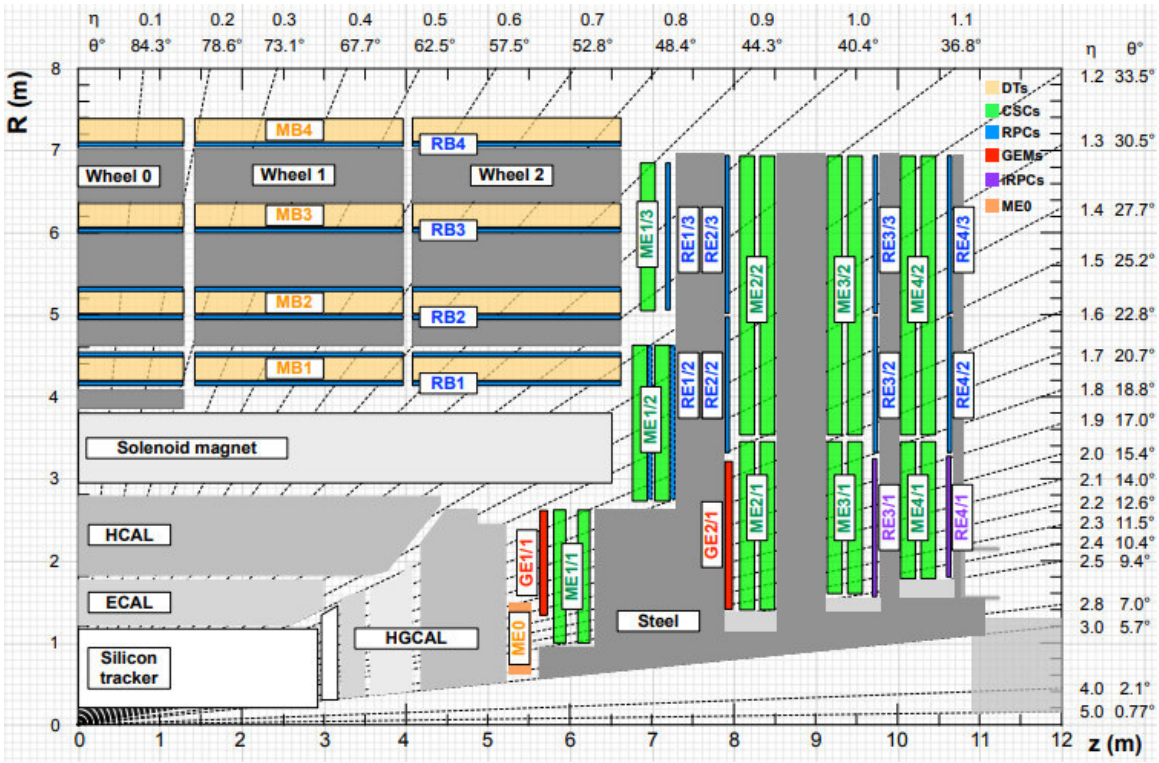

Figure 4-1: Layout of one quadrant of CMS. The slots RE3/1 and RE4/1 are to be instrumented by improved RPC chambers for the HL-LHC upgrade [114].

4.1 Installation of the iRPC in the Endcap Region

During the HL-LHC phase, the instantaneous luminosity in the CMS experiment is expected to increase up to $5-7\times10^{34}$ cm^{-2} s^{-1}. The forward region of CMS will be equipped with iRPC during the LHC shut-down periods to cope with the expected high particle rate. The iRPC in the stations RE3/1 and RE4/1 will cover the region of $1.8 < |\eta| < 2.4$ (Fig. 4-1). The chambers of these stations, with a good intrinsic time resolution, would improve the rejection of background hits and low transverse momentum tracks.

The geometry of iRPC is new, so to estimate the expected rate of the background, it is necessary to study the sensitivity of the chamber. The GEANT4 [8] modeling toolkit was used to model the geometry of iRPC and then to study its sensitivity. The sensitivity (S) indicates how the detector reacts to particles reaching it. It is converted into a probability that a given kind of particle, at given energy reaching the detector surface, will produce a signal that the detector could observe. The ratio of the number of detected particles (N_{Hit}) to those reaching it (N) gives the sensitivity of the detector to this background as indicated in Equation 4.1.

$$S(E) = \frac{N_{Hit}}{N(E)} \tag{4.1}$$

The results of the simulation of several kinds of background particles are given in Figure 4-2.

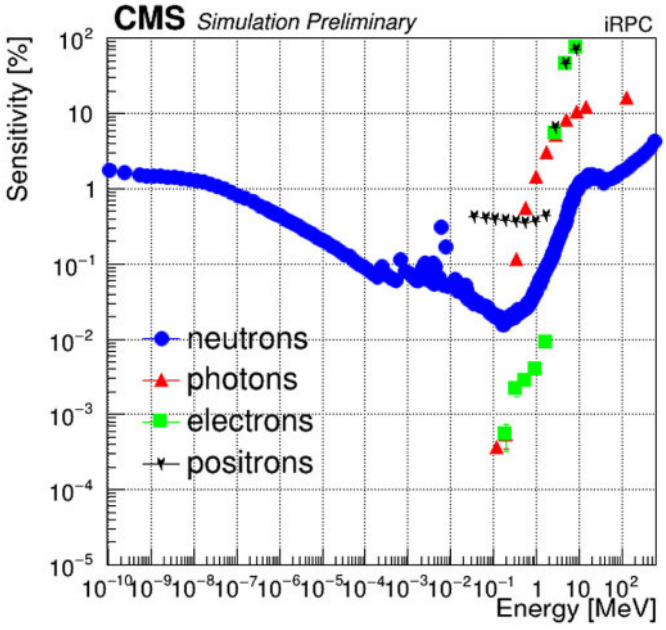

Figure 4-2: The sensitivity of iRPC was studied with different particles as a function of the kinetic energy of the incident particles [79].

The average background rate seen in iRPC has been estimated using the average sensitivity values: n(0.47%), γ(2%), e(7%).

The FLUKA [15] simulation foresees a maximum rate of 660 Hz/cm^2 for RE3/1 and around 500 Hz/cm^2 for RE4/1 (Fig. 4-3). When including a safety factor of three, the values approach $\sim$ 2000 Hz/cm^2 and $\sim$ 1600 Hz/cm^2 respectively.

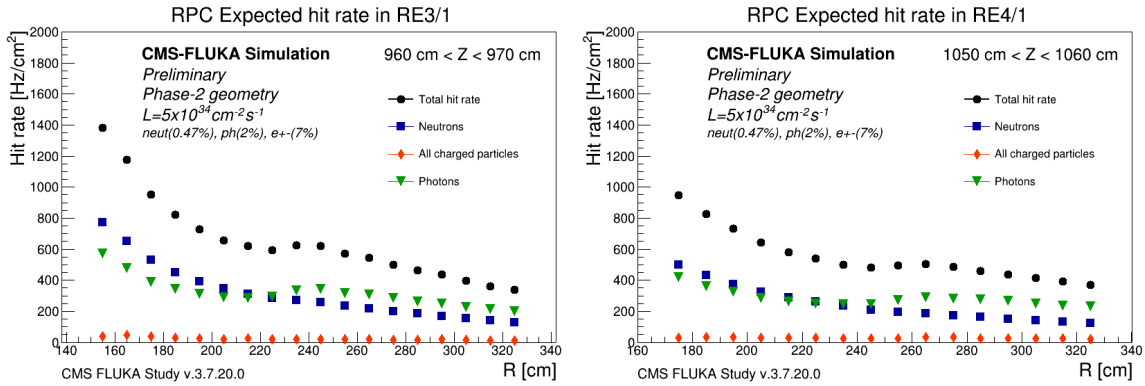

Figure 4-3: The expected particle rates in the iRPC of RE3/1 (left) and RE4/1 (right) during the HL-LHC as a function of the distance (R) from the center of the CMS beam pipe [78].

The expected average rate in the iRPC stations is relatively high in comparison to the average rate (RE4/2: 180 Hz/cm^2, RE4/3: 120 Hz/cm^2) of the others Endcap RPC stations (Fig. 4-4), which demands the iRPC to be of high rate capability.

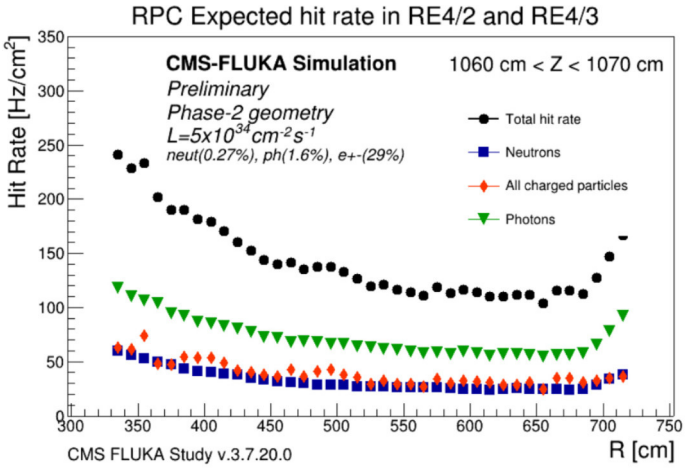

Figure 4-4: The expected particle rates in iRPC of RE4/2 (R332 cm) and RE4/3 (R503 cm) during the HL-LHC as a function of the distance (R) from the center of the CMS beam pipe [66].

According to the preliminary scenario of the installation in the RE3/1 region, the iRPC will be installed directly on the Endcap yoke 3 (YE3) iron disk (Fig. 4-5, left). The chambers in this region will cover the circular neutron shielding attached to the inner part of YE3 and reach the cylindrical neutron shielding surrounding the flange that separates the yokes YE2 and YE3 (Fig. 4-5, middle). The RE4/1 chambers will

be installed also in a high $|\eta|$ region, over the ME4/1 chambers. In this case, the aluminum mounting frame (8 mm) will be installed to the back of the CSCs, to which the iRPCs will be attached (Fig. 4-5, right). The chambers will be directly screwed to this frame, and the iRPCs and the frames will be fixed separately [88].

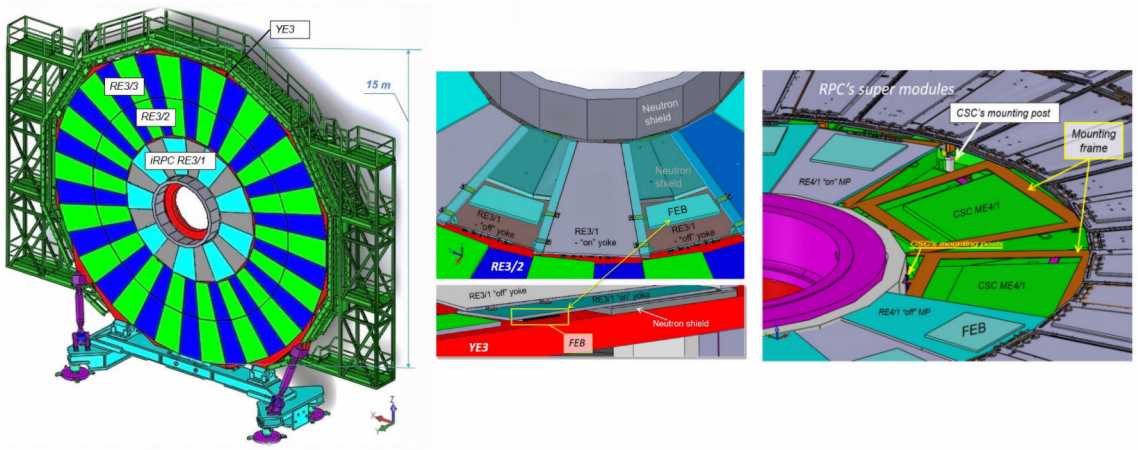

Figure 4-5: Detailed scheme of installation of the RE3/1 chambers on the YE3. 3D-drawing of the RE3/1 chambers fixed on the YE3 (left). The FEBs mounted behind RE3/1 chambers (middle). Schematic view of the RE4/1 chambers mounted on the mounting plate (right) [88].

4.2 The Chamber Layout

The prototypes have the standard layout shown in Figure 4-6. An iRPC prototype is made of a double-gap detector where each gap is made of two 1.4 mm High-Pressure Laminate (HPL) electrodes and separated by a gas gap of the same thickness. Front-End Board (FEB) was developed to read out the two ends of pickup strips printed on a PCB panel placed between the two gaps. The two gaps and the strips PCB are protected against electromagnetic interference by a copper layer, and all are placed in an aluminum (honeycomb) cassette.

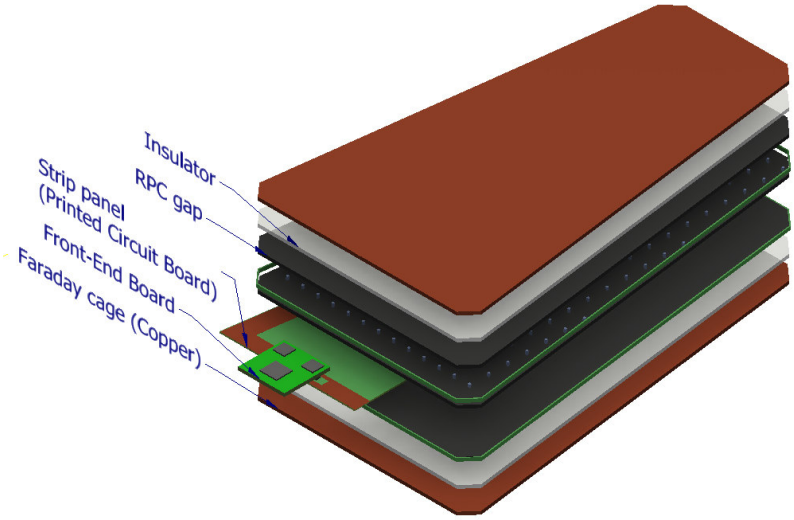

Figure 4-6: Layout of improved Restive Plate Chamber.

The parameters of the detector are summarized in Table 4-7.

Table 4-7: The iRPC parameters.

The number of gas gaps	2
High pressure laminate thickness	1.4 mm
Resistivity	$0.9 \sim 3 \times 10^{10}$ Ωcm
Gap thickness	1.4 mm
The number of PCBs	2
The number of FEBs	$(2-8)$[1]

[1]The number of FEBs depends on the versions of the FEB and PCB.

4.2.1 Gaseous Detectors

Each gap of the iRPC is made of two HPL panels of Bakelite [48] coated each by a graphite layer on its outer face. The panels are separated by spacers that determine the thickness of the gap. The high voltage is applied to the graphite coating to provide the required electrical field inside the gap.

Considering the mechanical constraints of the existing muon Endcap, the dimensions of RE3/1 and RE4/1 chambers will be different. The dimensions of the new gaps are optimized accordingly (Fig. 4-8). In a chamber with two gaps, the spacers (dots in Fig. 4-8) separating high-pressure laminate panels are not placed in the same positions for these two gaps. This is done to reduce the dead zones of the detector. Thus, the spacers' different arrangement in the gaps allows keeping effective all the chamber's surface. Indeed for each position point of the detector, at least one gap would be sensitive.

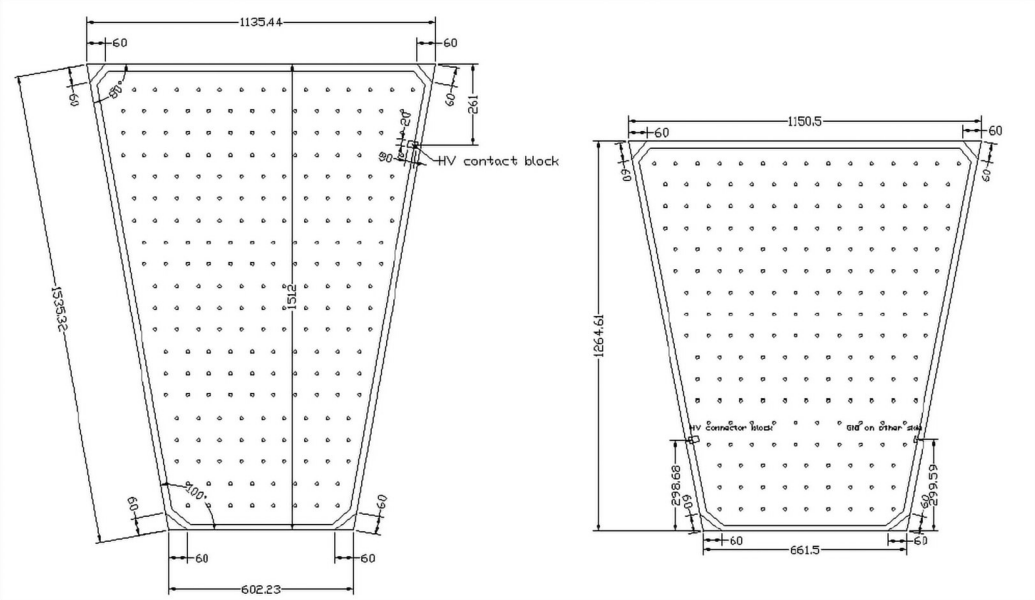

Figure 4-8: Dimensions of the HPL plates of RE3/1 (left) and RE4/1 (right) iRPCs.

Gaseous detectors like RPC operate through the ionization process (See Ch. 3.4.5), which results in the production of electron-ion pairs within the gas volume. The external electric field accelerates the electrons, which, in turn, leads to further ionization within the gas and amplification of the charge. The drift of the charge in the gas gap towards the anode induces a charge on the receiving strips, leading to the RPC signal. The high resistivity causes a drop within the electric field, locally in the zone of ionization, and leaves the rest of the volume sensitive to the passage of other charged particles. As a gas detector, the RPC has several modes of operation to provide useful signals (Fig. 4-9).

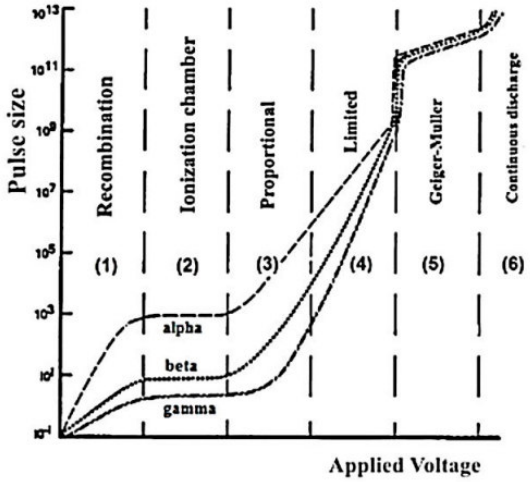

Figure 4-9: Six-region curve for gas-filled detectors [77].

Several configurations of the RPCs are possible to provide operation in the proportional mode, but we will use here as an example one with a simple structure that can be operated in avalanche, streamer, and spark mode. In this structure, a gas layer is sandwiched between two resistive electrode plates. The electrode plates are painted with graphite, used to distribute the high voltage to the electrodes. The electronics can be placed on either side of the chamber behind an insulating layer made of polyethylene terephthalate (Fig. 4-10).

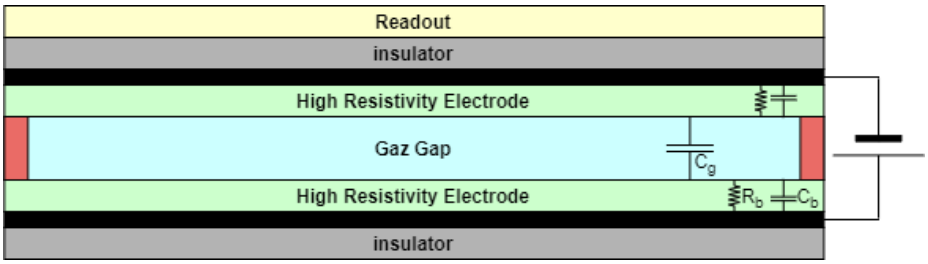

Figure 4-10: The diagram of a typical RPC.

A simplified electrical model of an RPC can be obtained (Fig. 4-10) by noting C_b the capacitance of the Bakelite, R_b its resistance and C_g the capacitance of the gas.

The resistance and the capacitance of the Bakelite electrodes are given by:

$$R_b = \frac{\rho d}{S}; \quad C_b = \epsilon_0 \epsilon_r \frac{S}{d}, \tag{4.2}$$

where ρ is the bulk resistivity of the Bakelite; d is the thickness of the electrode; S is the electrode surface area; ϵ_0 is the permittivity of the vacuum; ϵ_r is the relative permittivity of the Bakelite.

The avalanche mode (Fig. 4-11) is the first operating mode when the voltage between the electrodes is increased. The gas ionization creates a few pairs of electron ions that are then accelerated by the electric field. The electrons, which are much faster than the ions due to their lower mass, ionize more gas molecules. This multiplication of charges is called an avalanche. This process will create a fast signal of the order of a nanosecond that can be collected.

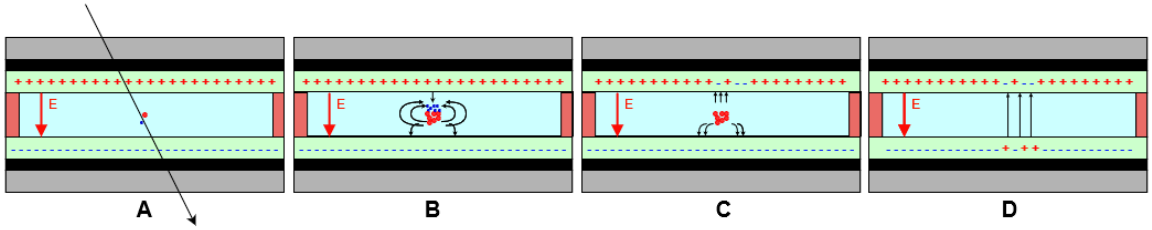

Figure 4-11: The diagram of an avalanche mode of RPC. (A) The passage of a particle ionizes molecules in the gas. (B) The size of the avalanche influences the local field. (C) The electrons reach the anode. (D) The ions reach the cathode. The charge is induced.

The operation of an RPC in the streamer (Fig. 4-12) and spark (Fig. 4-13) modes is similar to that of a spark chamber. The ionization of the particle creates electron-ion pairs. The electrons drift and multiply. At some point, if the gas multiplication factor is high enough, new avalanches begin with the electron-ion pair created by photons through photoionization and contribute to the generation of a complete avalanche.

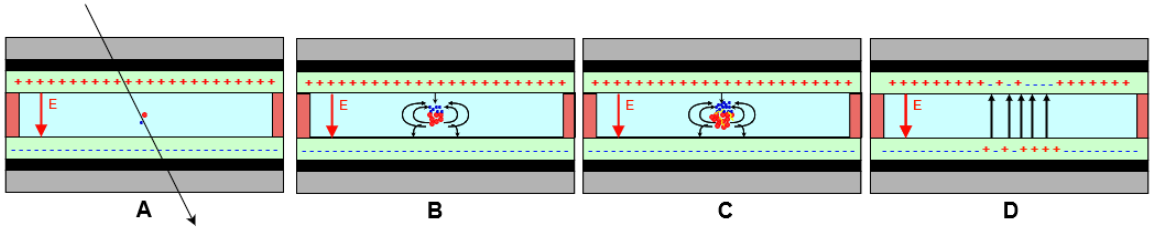

Figure 4-12: The diagram of a streamer mode of RPC. (A) The passage of a particle ionizes molecules in the gas. (B) The size of the avalanche influences the local field. (C) Photons contribute to the development of the avalanche and spread the avalanche. (D) The ions reach the cathode. Charges are induced in the readout electrodes.

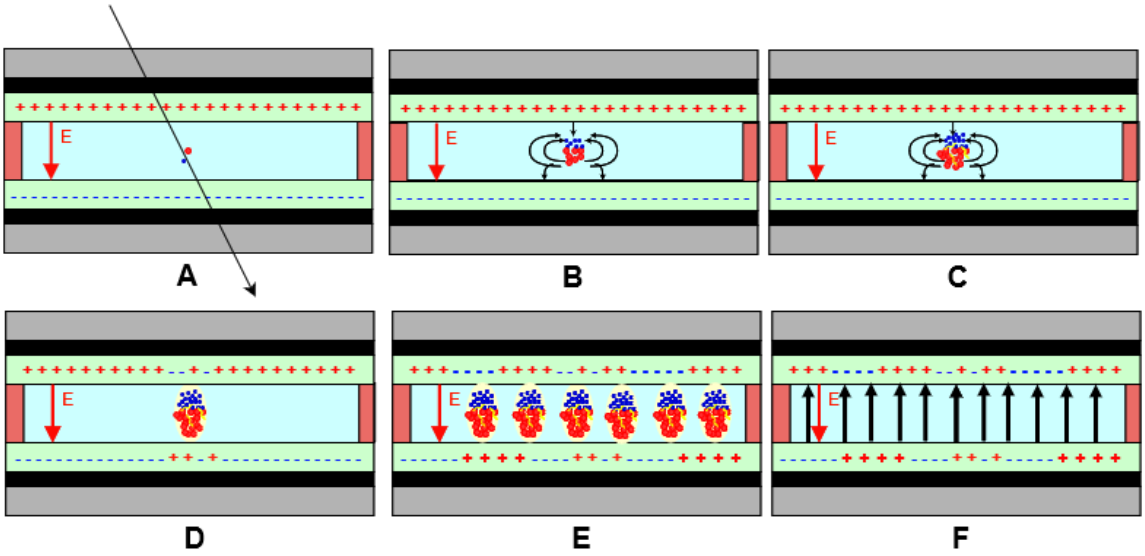

Figure 4-13: The diagram of a spark mode of RPC. (A) The passage of a particle ionizes molecules in the gas. (B) The size of the avalanche influences the local field. (C) Photons contribute to the development of the avalanche and spread the avalanche. (D) Plasma can be created between the electrodes and produce a spark. (E) The flashes are created by migrating electrons and photons. (F) The electric field is strongly lowered in the whole gas gap.The chamber is blind.

To operate the RPCs within the avalanche mode [118, 24, 84], the following gas mixture is used:

$$95\%\ C_2H_2F_4, 4.5\%\ iC_4H_{10}, 0.3\%\ SF_6 \tag{4.3}$$

The tetrafluoroethane is a gas with low ionization potential that provides the electrons of the avalanche when a charged particle crosses the gap. The isobutane is used to absorb the photons produced within the avalanche in order to avoid the development of secondary avalanches and thus to avoid false positives (reduce cluster size and secondary clusters). Finally, the sulfur hexafluoride is used to contain the size of the avalanches and prevent streamers and sparks.

As mentioned before, a high electric field in the gap gets the charged clusters to shift towards the electrodes. The electrons have a much higher drift velocity than positively charged ions because of their much smaller mass. At the same time, ions move in the opposite direction and are accelerated in the direction of the anode, ionizing even more molecules along their path. The process continues, and an electron avalanche develops towards the anode with its growth controlled by the equations (Eq. 4.4, Eq. 4.5).

$$\frac{d\overline{n}}{dx} = (\alpha - \beta)\overline{n} \quad \frac{d\overline{p}}{dx} = (\alpha)\overline{n}, \tag{4.4}$$

where α is the rate of creation of secondary ion-electronic pairs created at a distance

dx (Townsend's coefficient); β is the rate of electron capture at a distance dx by electrically negative ion with the formation of attachment factor (attachment coefficient).

If the initial conditions $\overline{n} = 1$ and $\overline{p} = 0$ are set, then we obtain the average number of electrons and positive ions produced at a distance x.

$$\overline{n}(x) = e^{(\alpha-\beta)x} \quad \overline{p}(x) = \frac{\alpha}{(\alpha-\beta)}(e^{(\alpha-\beta)x} - 1) \tag{4.5}$$

Townsend's coefficient depends on the applied electric field. Figure 4-14 shows this dependence for a given gas mixture.

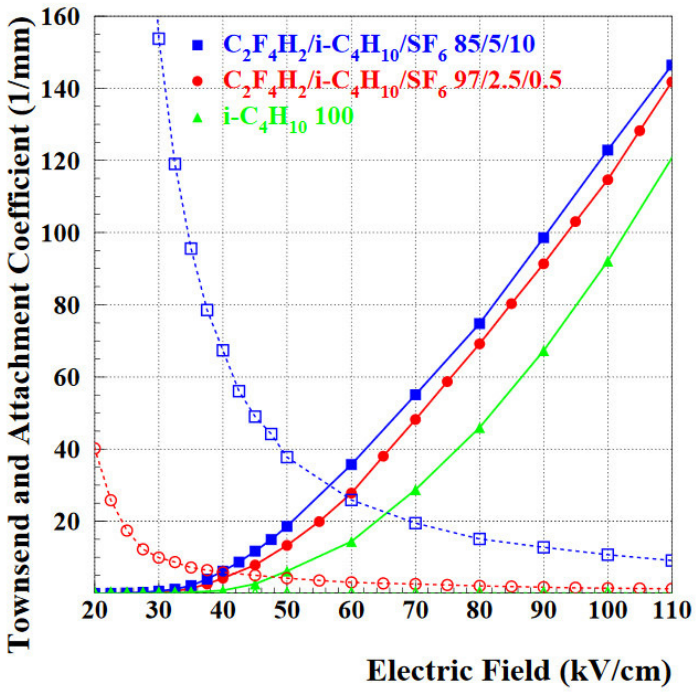

Figure 4-14: Townsend and attachment coefficient [98].

An example of electron Townsend avalanches in a parallel plate counter is shown in Figure 4-15. The avalanche grows exponentially when the number of electrons has reached about a certain size (about 10^2):

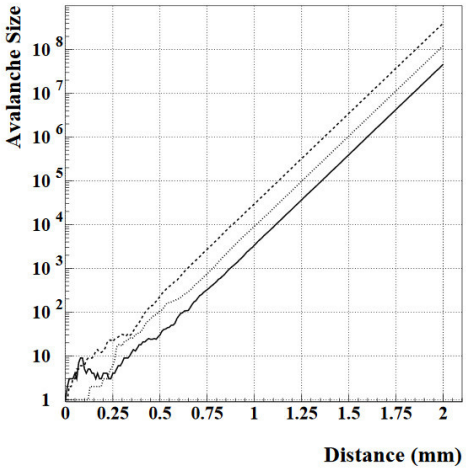

(a)

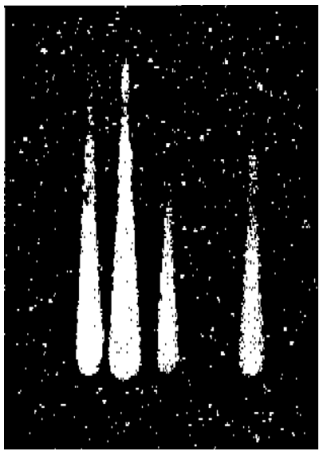

(b)

Figure 4-15: (a) Avalanches started by a single electron.at x = 0 for $\alpha = 13/\text{mm}$, $\eta = 3.5/\text{mm}$ [99]. (b) The photograph of electron avalanches in a parallel plate counter [96].

The avalanche produced by the charged particle induces a signal on the electrodes of the chamber. The resistive anode will absorb the produced electrons and ions and then transfer them to the resistive coating, thus evacuating the charge. The charge movement within the gas detector will generate a current on the electrodes. Ramo's theorem gives the induced current due to the charge movement by [97]:

$$i(t) = \vec{E}_\omega(\vec{x}(t))\frac{Q}{V_\omega}\dot{\vec{x}}(t)), \tag{4.6}$$

where $\vec{E}_\omega(\vec{x}(t))$ is the electric field in the detector at the position $x(t)$ when the given electrode is put to the voltage V_ω and the others grounded; Q is the charge of electrons.

The avalanche electrons thus induces on the pickup strips a signal to be detected by the electronics (Fig. 4-16).

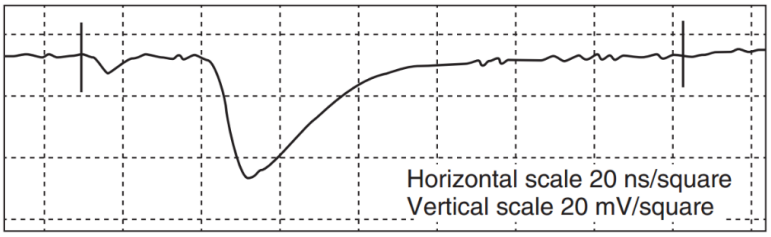

Figure 4-16: Example of an RPC signal showing an avalanche precursor followed by a streamer pulse [101].

When detectors are operating at high background loads a large amount of charges are created leading to a drop in the voltage. The time needed to establish the electric

field in the gap becomes longer, and during this time the detector is less efficient. The voltage drop can be expressed by the induced charge as follows:

$$dV = Q\frac{\rho L}{S}\Phi, \tag{4.7}$$

where dV is the drop of the voltage; Q is the produced charge; ρ is the bulk resistivity of the electrodes; S corresponds to the HPL surface; L is the cross-sectional area corresponding to the HPL thickness; Φ is the flux of the background particles.

According to the previous formula, the magnitude of the voltage drop produced by an avalanche can thus be reduced by reducing the resistivity, the avalanche charge or the thickness of the HLP. In the iRPC project it was decided to reduce the electrode's thickness from 2 mm with a resistivity range of $(1 \sim 6) \times 10^{10}$ Ω cm to 1.4 mm with lower resistivity range ($(1 \sim 3) \times 10^{10}$ Ω cm) allowing to evacuate the created charge faster.

Also, with a thinner (1.4 mm) gas gap, the charge produced by the passage of charged particles is smaller, and the efficiency plateau is reached at a relatively lower high voltage. The dependence of the high voltage values associated with two RPC efficiency references (50% and 95%) on the electrode thickness is plotted in Figure 4-17.

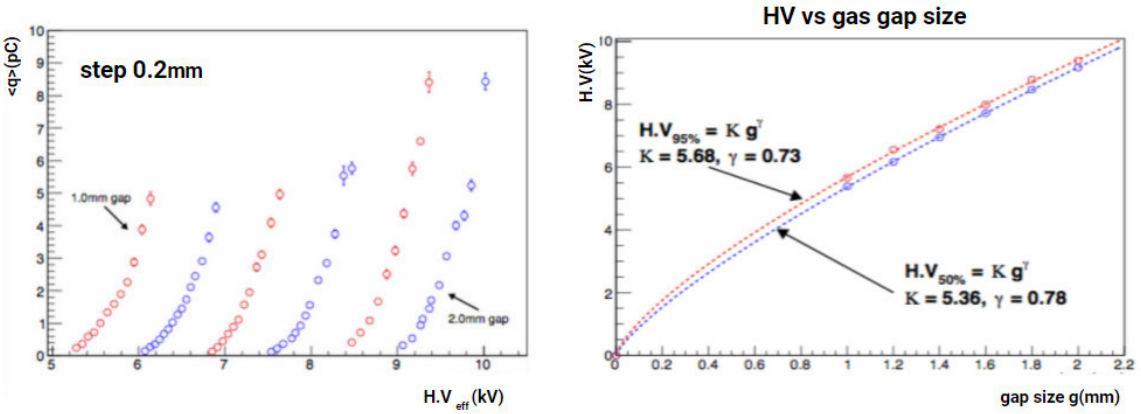

Figure 4-17: Left: Mean charge distributions of all six gaps at various HV. Right: Values of $HV_{eff=0.50}$ (blue) and $HV_{eff=0.95}$ (red) as a function of the gap thickness [93].

This change of gap thickness improves the iRPC rate capability and allows it to exceed 2 kHz/cm^2, which is a factor of three higher than the maximum particle rate expected in the top pseudorapidity region of the RE3/1 and RE4/1 ($\eta \sim 2.4$). However, new gas detectors require new strips PCB and new readout electronics with a better sensitivity to detect smaller avalanche charges that may be detected only with readout electronics with a lower threshold (See Ch. 4.3.2) with respect to the one used in the standard CMS RPC.

4.2.2 Strip Panels

In order to exploit the time information in the position determination and to reduce, at the same time, the number of electronic channels, two different types of Printed Circuit Boards (PCB) [70] strips PCB were conceived and produced. Both were tested for the prototype. Both are made with strips running along the double-gap detector. The first one uses strips whose ends are soldered to coaxial cables, through which the signal is transmitted to the electronics. The second, thanks to more advanced technology, uses return lines for each strip. These return lines are placed on the PCB's edge, and like the strips themselves, are buried in the dielectric material of the PCB. This scheme enables reading the signals directly from the PCB through a connector without using coaxial cables. A schematic illustration of the two types of strips PCB is shown in Figure 4-18.

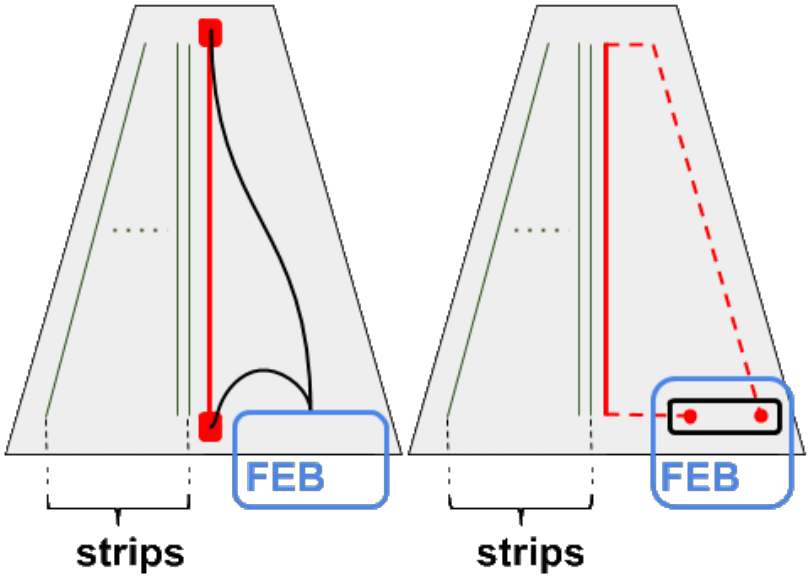

Figure 4-18: Illustration of PCB with return lines (right) and coaxial (left) cables.

The strips PCB with coaxial cables (Fig. 4-18, left) uses a standard approach to transfer the signals from the PCB. The readout from both ends of the strip requires soldering coaxial cables to both ends of each strip with a perfect impedance matching between strips and cables.

To measure the strip impedance, three different methods were used. Direct measurement at 2 MHz gives a value of 44 Ω. Another direct measurement with potentiometric line adaptation provides a value of $Z_c = 46$ Ω, and finally, a reflection method gives the value of $Z_c = 41$ Ω.

From these different measurements, one can estimate the average impedance of one strip to be around 44 Ω, which cannot be perfectly matched with commercial coaxial cables that have only 50 Ω or 75 Ω [23].

For the second solution of PCB (Fig. 4-18, right), the strips have return lines that help collect signals from both ends with only one connector. Return signals

are transferred via shielded return strips embedded in the middle of the PCB. These return strips were designed, so their impedance matches that of the pickup strips.

However, signals that were transmitted through the return line have their amplitude slightly diminished. A signal transmission study with PCB using a common 600 μm FR4 material with a dielectrics constant about 4.3 [91] and with a PCB using a new material EM888 with typical dielectrics values 3.7 [54], was made. In EM888 material, the amplitude loss due to the propagation of the signal along the strip is expected to be less than with FR4. The transmission loss versus the frequency for materials with different dielectric constant (ε) are shown in Figure 4-19. Thus, the EM888 is indeed more effective in terms of signal transmission with less attenuation.

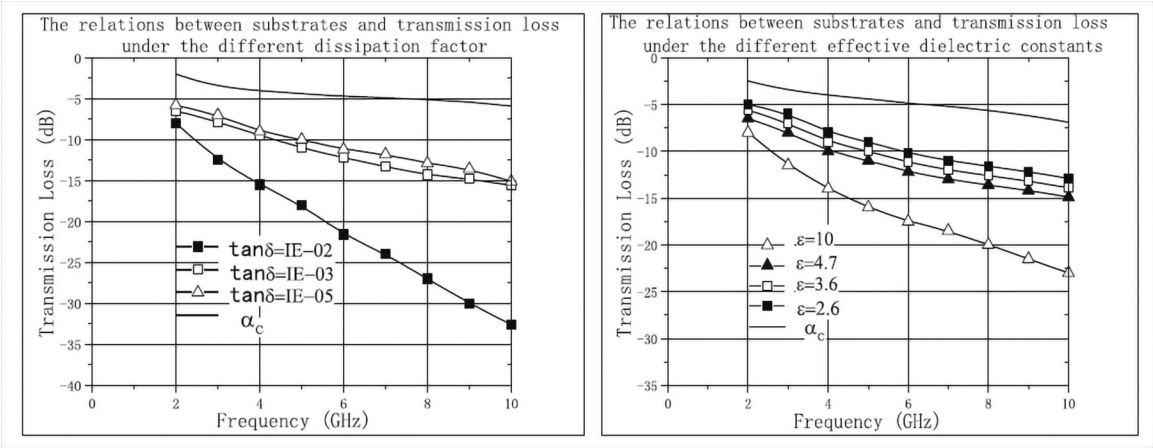

Figure 4-19: The relations between effective dielectric constant, dissipation factor and transmission under the different frequencies [103].

In this study (Fig. 4-20 and Fig. 4-21), the charge was injected into one side and measured from the other side of the strip. This injection gives the worst possible scenario for amplitude reduction of signals passing through the pickup strip in addition to the return line.

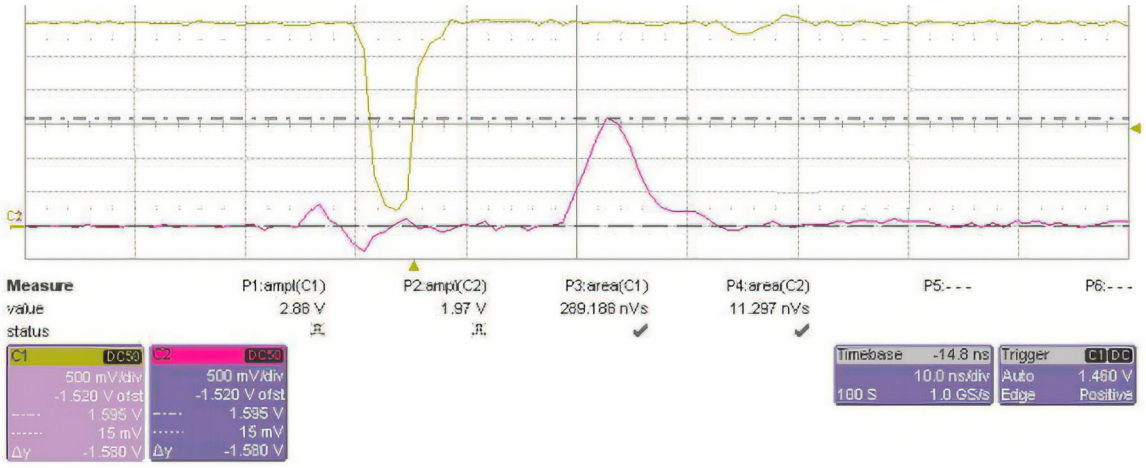

Figure 4-20: Signals measured from opposite sides of a PCB with 48 strips PCB made of FR4 material.

Figure 4-20 shows the waveform of the injected signal (yellow) with an amplitude of 2.88 V and the collected signal on the opposite side (red) with an amplitude of 1.97 V, which represents 32 % signal loss.

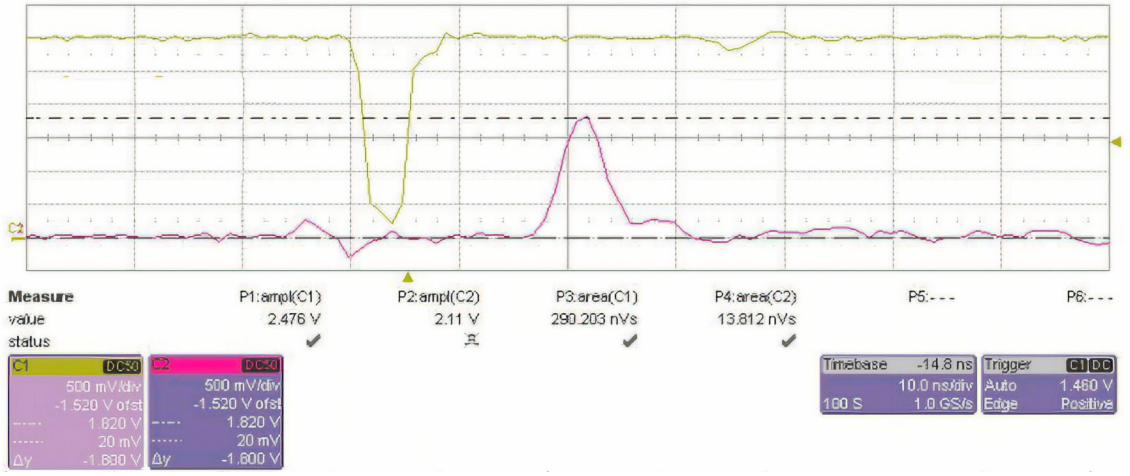

Figure 4-21: Signals measured from opposite sides of a PCB with 48 strips PCB made of EM888 material.

Figure 4-21 shows the waveform of the injected signal (yellow) with an amplitude of 2.48 V and the collected signal on the opposite side (red) with an amplitude of 2.11 V for a new PCB with EM888 dielectric material, which represents 15 % signal loss.

This confirms the expectation that EM888 presents an important improvement with respect to the signal transmission justifying its future use.

During the R&D phase, two types of return strip PCBs were produced. Pictures of both, as well as their main dimensions, are shown in Figure 4-22. The difference in connectors position is primarily due to issues of assembly and integration of the

RE3/1 and RE4/1 stations. In addition, placing the connector location as far away as possible from the high background rate is a big advantage, so the electronics are less exposed to irradiation.

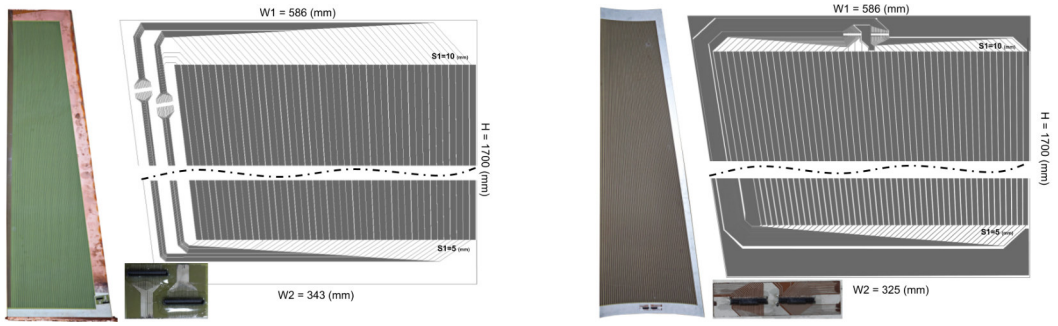

(a) (b)

Figure 4-22: (a) A photo of the first version of the strips PCB and its schematic drawing. (b) A photo of the second version of the strips PCB and its schematic drawing.

Therefore, on the final strips PCB (Fig. 4-23), the signals from the detector are read out from the connector that will be placed in the middle of the PCB top side, thanks to the Front-End Board (FEB). It is worth noting here that the FEB input impedance is precisely adjusted to avoid signal reflections.

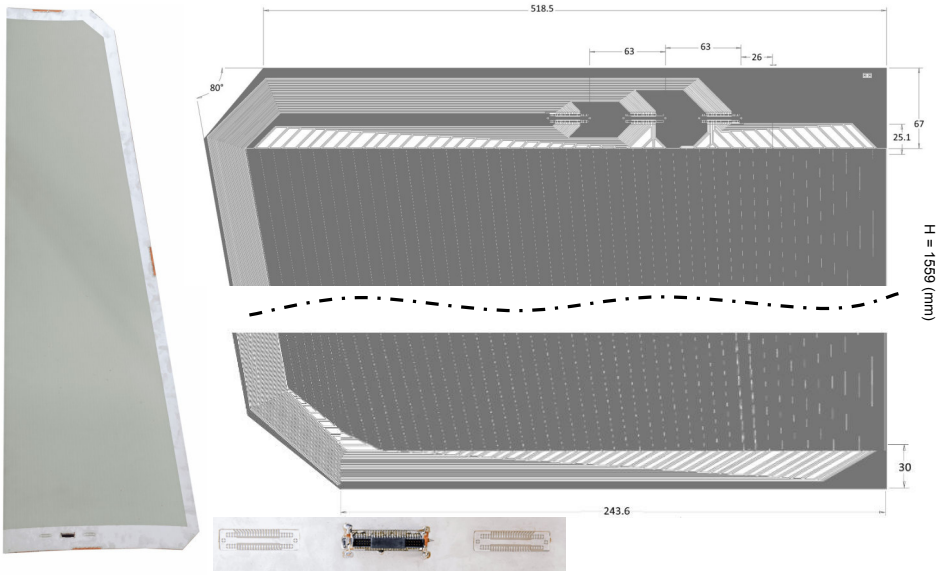

Figure 4-23: A picture of the third version of strips PCB accompanied with its schematic drawing.

4.2.3 The Faraday Cage

The operation of the iRPC in the RE3/1 and RE4/1 stations should be correctly protected against the electromagnetic noise from the associated electronics and other detectors. With a Faraday cage, the external electric field leads to the redistribution of free electrons into the conductive material. This charge creates a field that compensates the external field in such a way that no external field is present inside the cage. Consequently, the noise generated by the external field in the detector and the electronic readout system is drastically eliminated.

The need to transfer the signal from strips to the FEB placed on the cassette and the gas pipes' presence prevents the complete wrapping. However, when using the proposed strips PCB with return lines, only two small apertures in the Faraday cage for FEB connection in addition to a few tiny windows for gas inlets are needed. The Faraday cage of the first prototype (Fig. 4-24, left) and the last prototype (Fig. 4-24, right) are made with 0.1 mm copper foils. Although the Faraday cage mentioned above achieves the required noise reduction. We plan to replace the copper foils with copper plates in the final version of the chamber in order to avoid impedance variation along the strips due to possible changes in the distance between the gaps and the less stiff copper foils. This distance is an important parameter of impedance control.

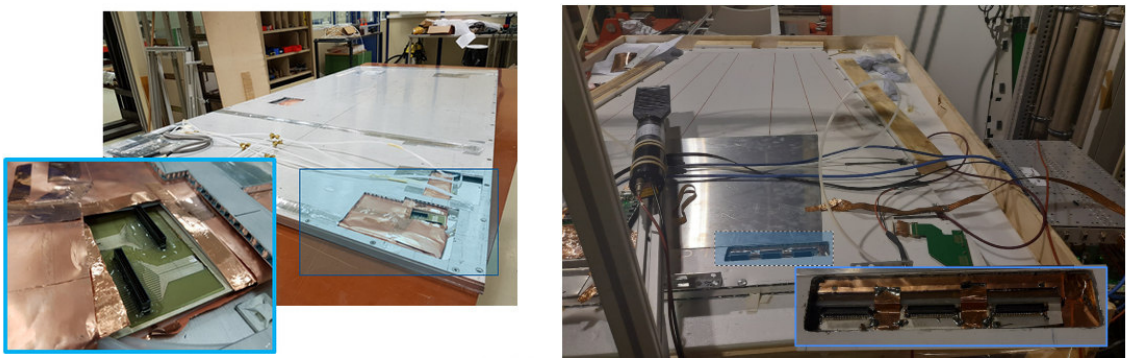

Figure 4-24: Photos of the technical apertures in the Faraday cage of the two versions of prototyp, both using PCB with return lines.

The evaluation of the influence of the Faraday cage and grounding on the noise can be illustrated from the electronics threshold level values used for our measurements. This threshold level was fixed as a five sigmas shift from the mean value of the pedestal (See Ch. 4.3.2) for the different stages of the chamber shielding (Fig. 4-25).

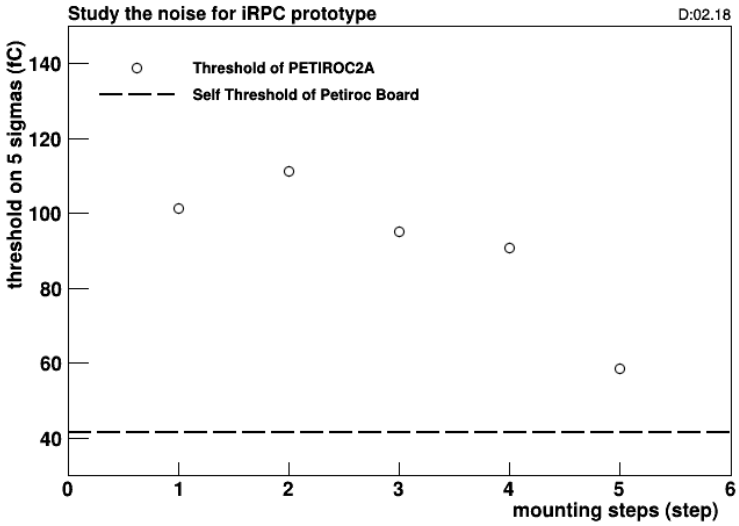

Figure 4-25: Threshold values of the electronics for different stages of chamber shielding (mounting steps at different stages of production). The threshold is fixed as a five sigmas shift from the mean value of the pedestal.

In Figure 4-25, measurements of the pedestal for the setup corresponding to the five stages of the chamber shielding are shown. The line is the threshold of electronics without connection to the PCB. The first step of assembly shows the minimum threshold for electronics without any protection of PCB with Faraday cage. On the second step, PCB was placed between two gaps. Step three gives the threshold for a completed Faraday cage but with no grounded cassette. Step four is the complete cage with a plugged electronic and wrapped area of the connector with copper. The last step is a complete cassette with the full grounding. In conclusion, we can summarize that the Faraday cage is an important piece of the prototype to reduce noise. Indeed, with the Faraday cage, the electronics can be operated at a threshold as low as 60 fC.

4.3 Front-End Electronics

The new 1.4 mm chambers are conceived such that the amount of deposited charge associated with the passage of charged particles is reduced with respect to the present 2 mm RPC used in CMS muon chambers. The Front-End Board (FEB) has to be able to detect signals with a charge as low as 100 fC and also needs to be fast and reliable, and it must sustain the high irradiation environment.

Thus, FEB is one of the key components of the iRPC, providing the readout of the signals. The performance of the chamber is largely dependent on the performance of the electronics. Electronics can be implemented using various technologies. Combinations of an Application-Specific Integrated Circuit (ASIC) for discriminating signals and processing them in Field Programmable Gate Arrays (FPGA) using a high-resolution Time-to-Digital Converter (TDC) make it possible to achieve the

required characteristics. In Figure 4-26, two FEB versions that were developed are shown. FEBv0 board contains one PETIROC ASIC plus FPGA (CYCLONE 2) and an Ethernet-based communication system. It was conceived to read out the strips PCBs with return lines. FEBv1 was intended to come closer to the final board to be compatible with CMS DAQ, and it includes two PETIROC 2A(B) plus a more powerful FPGA (CYCLONE V). An ethernet-based communication system was also used to read out the return strips PCB.

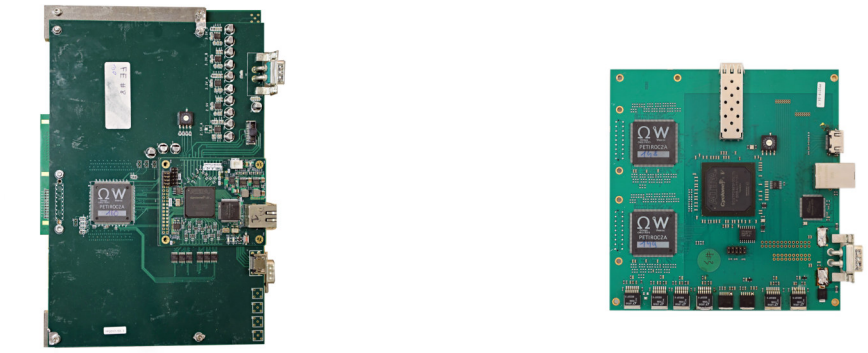

Figure 4-26: Left: Front-End Board version 0. Right: Front-End Board version 1.

The two main parts of the FEBs, which are the PETIROC ASIC and the TDC on the Field Programmable Gate Arrays (FPGA), will be presented in the following chapters.

4.3.1 The PETIROC

To fulfill the requirements, a new Application Specific Integrated Circuit (ASIC) is needed. The PETIROC designed in 0.35 μm SiGe technology developed by OMEGA group was found to be adequate for our application [56]. The die size (chip size) of this is 4.6x4.2 mm and can be provided as a naked die or in a QFP208 package. The layout includes analog and digital parts (Fig. 4-27). The ASIC allows us to reach a low threshold and to provide an excellent time precision measurement that we can use to determine the position along the strips used to pick up the detector signal.

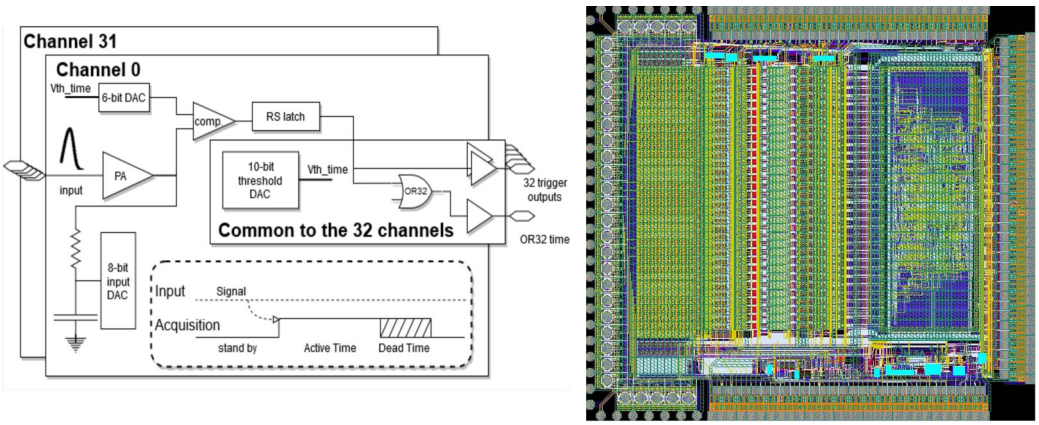

Figure 4-27: Left: General ASIC block scheme. Right: ASIC layout [56].

A fast trigger line is made of a 1 GHz bandwidth common-emitter preamplifier with a comparator. A fast discriminator follows each preamplifier. The ASIC uses a common 10-bit Digital Analogue Converter (DAC) system to ensure a global triggering level adjustment in the ASIC dynamic range. Furthermore, an individual 6-bit DAC is used in each channel to achieve the same response of all the channels for a given injected charge.

The ASIC is operated in its latch mode (Fig. 4-28). Within this operation mode, when the signal produced by the passage of a charged particle crossing the iRPC passes the threshold of the ASIC's channel connected to the closest of the two strip's ends, the discriminator of this is neutralized during a period that could be fixed by software with typical values between 20 ns − 30 ns. This period is the maximum time needed for the signal to reach the ASIC's channel connected to the other end of the fired strip. After this period, the ASIC with all its channels[2] is reset during a time interval, whose value is chosen to allow a full stabilization of the ASIC. For the different FEB prototypes developed so far, 10 ns was the lowest possible value that was possible to obtain. The main actor of this limit is the re-triggering effect. Since the electronic is set to a minimum threshold, there is a probability that the channel is reactivated several times (See Ch. 5.4) after receiving the signal. The structure of the ASIC readout time is illustrated in Figure 4-27.

To take into account the test results (See Ch. 5), two different versions of PETIROC chips were developed. Version 2B has an additional mode with respect to PETIROC2A. This new mode allows the lowering of the ASIC channels' threshold by reducing the bandwidth of the chip preamplifier (Fig. 4-28).

[2]The reset mode is global and involves all the ASIC PETIROC A(B) channels to be reset.

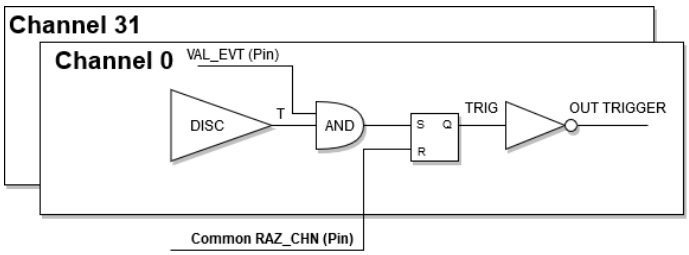

Figure 4-28: The block scheme of PETIROC 2A and 2B reset system.

In addition to the possibility to modify the bandwidth, the second (version 2C) is expected to have a new feature that allows resetting individually each channel thanks to a logic added to the channel's chain (Fig. 4-29).

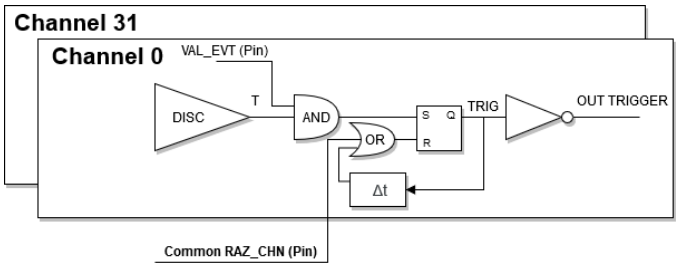

Figure 4-29: The block scheme of PETIROC 2C reset system.

The diagrams of the previous figures show the ASIC functionality of signal processing after its discrimination by a PETIROC 2(A,B) (Fig. 4-28) and PETIROC 2C (Fig. 4-29) channels. The signal processing implementations for versions 2A and 2B have only a common reset (RAZ) signal and provides a common restart of the channels. In version 2C, it is possible to set an individual reset time (Δt) and a restart of the channel after a delay. This modification intends to limit the impact of the reset dead time to only the fired channels (See Ch. 5.2.3). The assessment of inefficiency of FEB related to this dead time can be simplified as follows:

$$ineff = rate * N * surface * reset, \tag{4.8}$$

where $ineff$ is fraction of ineffective time during the operation of chip; $rate$ is the cluster rate (See Ch. 4.5.2) in $\frac{\text{Hz}}{\text{cm}^2}$; N is the number of connected strips to the chip; $surface$ is the surface of one strip; $reset$ is the rest time in seconds. In the case of PETIROC 2C N is the number of fired strips (mean value is three) due to the passage of a particle, but for PETIROC 2A(B),N is the number of connected strips to one chip.

Thus, the 2C version logic allows obtaining an individual reset for each channel, which reduces the chamber's inactive area during resetting, increasing the rate capability, since, at a high rate, only the fired channel has to be reset instead of all the PETIROC's channels.

4.3.2 Calibration of the PETIROC

To ensure the same threshold level for each FEB's channel, the comparators' operation levels need to be aligned with the help of 6-bits DACs. This alignment involves several steps: scanning all channels, choosing the reference position, and aligning all channels. Thus, by scanning the channels threshold in DAC units, we can determine the comparator's level of response to electronic noise. The curve obtained for each channel is called a pedestal. In the standard case, with the absence of an external pickup noise, the derivative of this curve can be described by a Gaussian function, which allows us to determine the mean value and the sigma for each channel. Using this, we can align all channels to the same position (mean value) and set each channel's threshold with a shift of a given number (usually five) of sigmas with respect to the common mean value. The latter is determined as the average mean values of all channels. The following plots (Fig. 4-30) show an example before and after the alignment of pedestals to achieve the uniformity of the channels' response.

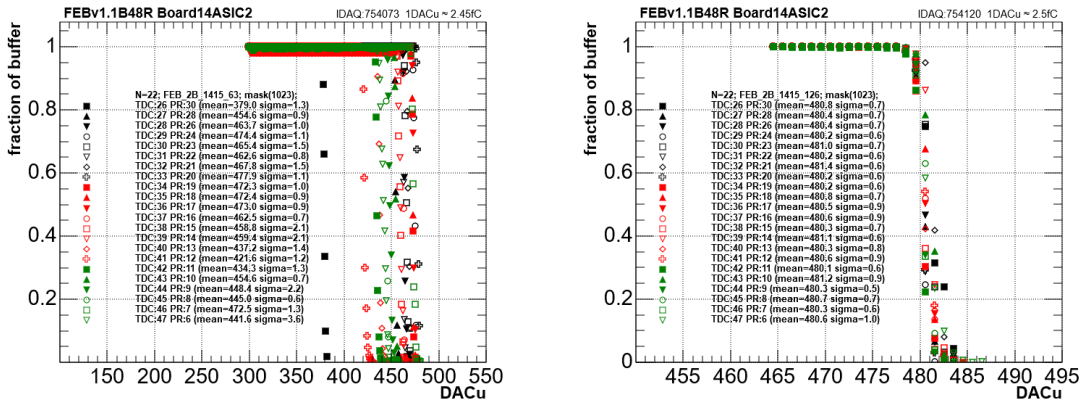

Figure 4-30: Example of alignment with 6-bit DACs. Left: Before alignment. Right: After alignment.

In addition to the 6-bit DACs used for the pedestal alignment, the common 10-bit DAC, is used to control the global threshold, as shown in Figure 4-31. The relation between DAC units and the signal levels is found to be linear.

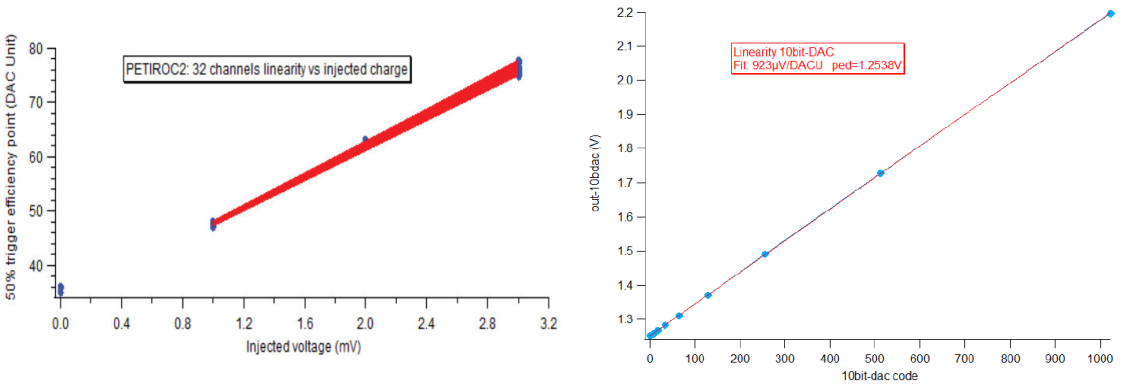

Figure 4-31: Left: 6-bit DAC linearity. Right: 10-bit DAC linearity [115].

Figure 4-31 shows the dependence of the signal level in volts on the DAC unit in PETIROC 2A chip where the output voltage versus the 10-bit DAC unit value is presented. It can be clearly seen that linearity is present in the entire output voltage range. S-curves measurements have been performed on 32 channels with 0,1,2 and 3 mV injected signal amplitudes. The corresponding linearity slopes for those channels their intercepts show a small dispersion among the channels (<2%).

The relation between fC and DAC unit was also measured from a test we performed where a signal was directly injected into PETIROC2A channels in two different modes (Fig. 4-32). The first mode was done by activating the channel where we did the injection. This exercise isolates the channel and protects it from perturbation that may be induced by the other channels. The second mode was done with all channels active.

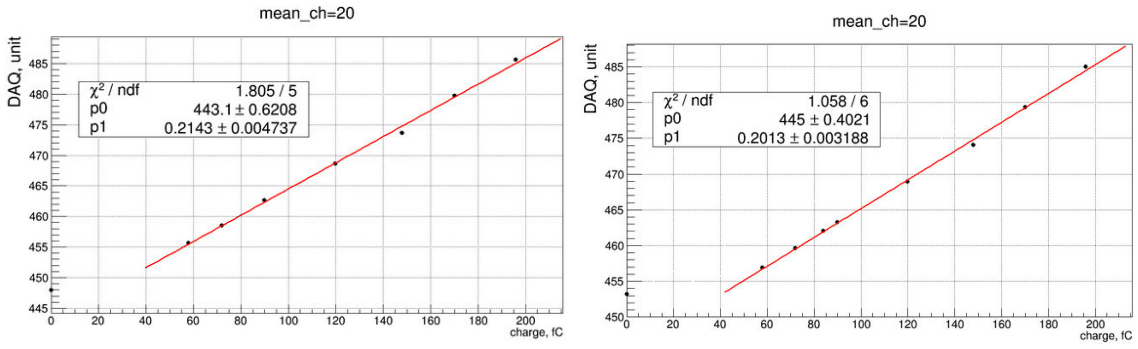

Figure 4-32: Calibration of channel 20 with signal injection while all other channels are masked (left) and all channels are active (right).

Also, it was observed that some channels of PETIROC2A ASIC have degraded linearity below 80 fC. This means that they can not be used with a threshold lower than 80 fC. An example of such a non-linearity behavior at low charge is given in Figure 4-33 for channel 20.

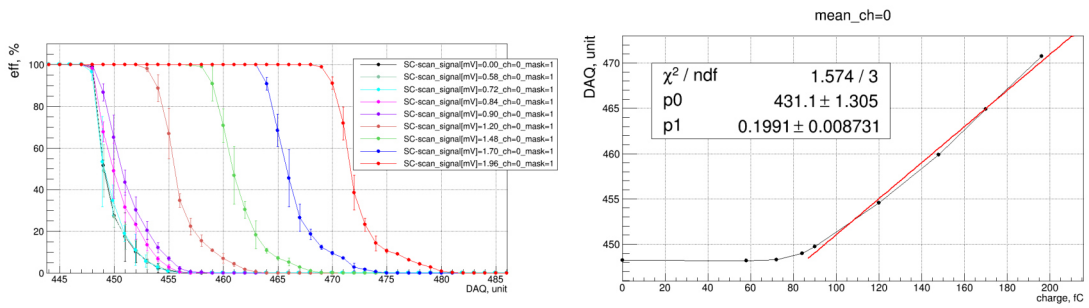

Figure 4-33: Calibration of channel 0 with an injection of the signal when all other channels are masked.

In addition to testing the ASIC when we inject a charge into the chip, we conceived a setup that includes a board and a strips PCB where we can inject a charge directly into the strip of the PCB. The purpose was to validate the whole chain. The relation between fC and DAC unit for this study is shown in Figure 4-34.

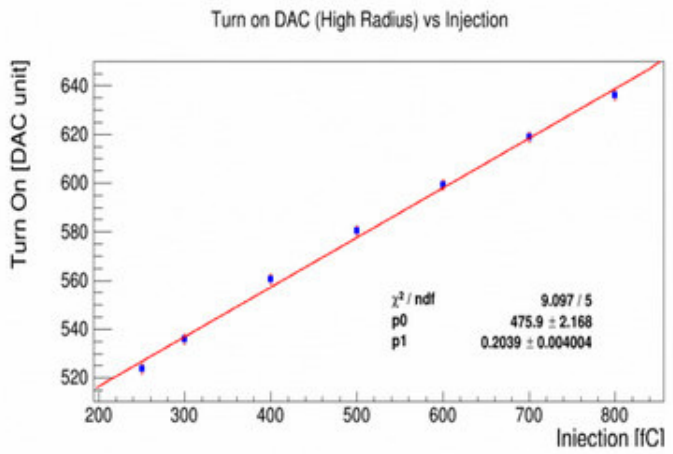

Figure 4-34: Calibration of a 10-bit DAC with an injection of a charge into the strip.

The result of tests with the injected signal into the strip agrees with the direct charge injection to the chip channel.

4.3.3 The High-Resolution Time-to-Digital Converter

The ASIC is controlled with a Cyclone Altera FPGA (slow control, commands, etc.). The same FPGA was configured to include a Time Digital Converter (TDC) firmware. The time measurement is carried out by a High-Resolution TDC Implemented using an improved tapped-delay-line technique [72, 33]. The TDC architecture is based on the principle that general-purpose FPGAs have many dedicated carry lines (Fig. 4-36) that can be used as delay cells for high-resolution time measurements. A simplified block diagram of the TDC is shown in Figure 4-35.

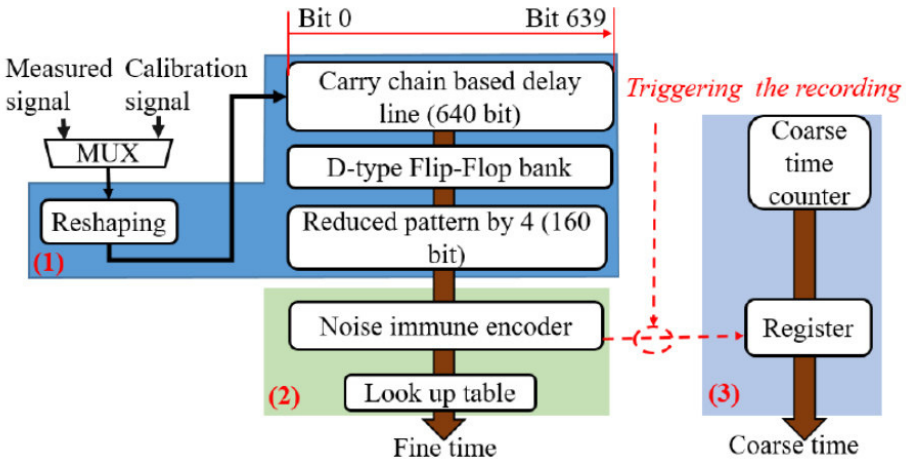

Figure 4-35: The block diagram of the Time-to-Digital Converter implemented in a single FPGA device [32].

Time is estimated by using coarse and fine time counters. Fine time measurement by a multi-bit adder carry chain line is shown in Figure 4-36.

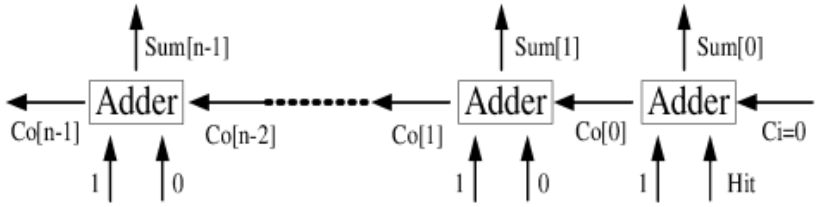

Figure 4-36: The diagram of the carry chain of a multi-bit adder [72].

If there is no hit signal, all bits would be a logical one. When there is a hit signal, each bit will change to a logical zero step by step. The changed bits indicate the elapsed time of the hit signal passing along the carry chain. At the next rising edge of the system clock, the sum bits will be latched.

An important step is to keep a uniform delay between the sum bits and the input of their corresponding register. A basic logic element containing a Look-Up Table (LUT) based calibration scheme was developed to correct non-linearity behaviors, and a programmable register is used to form the 1-bit adder, which generates the sum bit and the register for latching the sum bit.

The coarse timestamp of the TDC consists of a 24-bit register. The 24-bit register is triggered by the fine timestamp converter's detected signal to record the coarse time counter's value and translate it into a coarse timestamp.

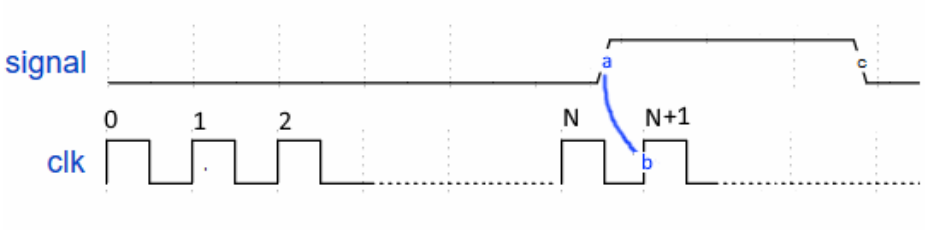

Figure 4-37: The diagram of course time measurements.

In the example presented in Figure 4-37, the coarse time counter takes the value N, and the fine time is estimated at the interval a-b. The total time measurement can be expressed as follows:

$$T_{out} = (N_{coarse} + 1) * clk - T_{fine} \tag{4.9}$$

where T_{out} is the result of the complete time measurement; cls is the time duration of the clock; N_{course} is the number of clocks of the coarse counter and T_{fine} is the result of the fine time measurement.

4.3.4 Calibration of the Time-to-Digital Converter

The TDC uses a delay chain line for time measurement. It is important to control the linearity of the Look-Up Table (LUT). A linearity analysis is performed with two parameters: the Differential Non-Linearity (DNL) and the Integral Non-Linearity (INL), which are defined by 4.10.

$$DNL_i = \frac{(lut[i] - lut[i-1])}{lut_{step}} - 1; \quad INL_i = \sum_{j=0}^{i} DNL_j, \tag{4.10}$$

DNL_v is the non-linearit value at a given step; INL_v is the integral of DNL_v up to i step; $lut[i]$ is the function of the center bin, defined using the width of the TDC bins W_k as [116]:

$$lut[k] = \frac{W_k}{2} + \sum_{n-1}^{k=0} Wk. \tag{4.11}$$

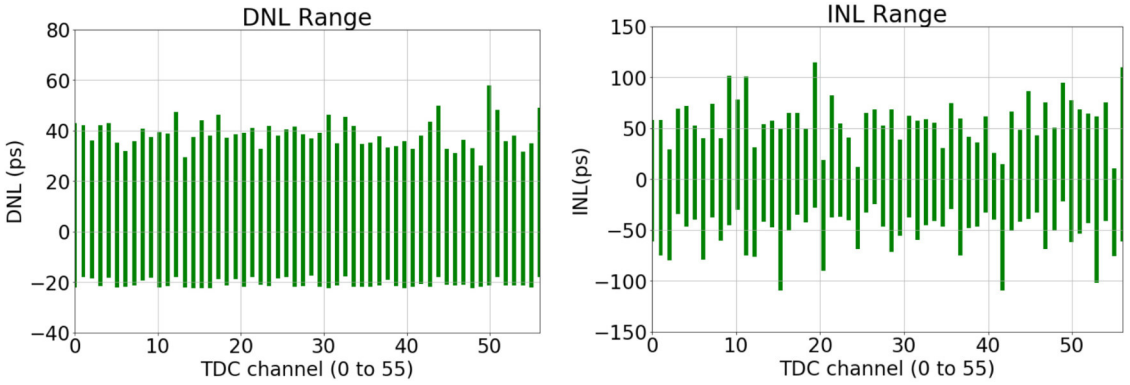

Figure 4-38: Left: Differential Non-Linearity of the TDC channels. Right: Integral Non-Linearity of the same channels.

The previous histograms show the range from minimum to maximum values for DNL (Fig. 4-38) for all TDC channels that were implemented in the FPGA.

4.4 The Readout System

RPC's standard readout design based on 4 or 5 pickup strips partitions[3] could not achieve the required spatial resolution in η. We propose another approach to measure the coordinate that relies on the Time Difference of Arrival (TDoA) method [89] that uses two signals obtained from High Radius (HR) side and Low Radius side (LR), as illustrated in Figure 4-39.

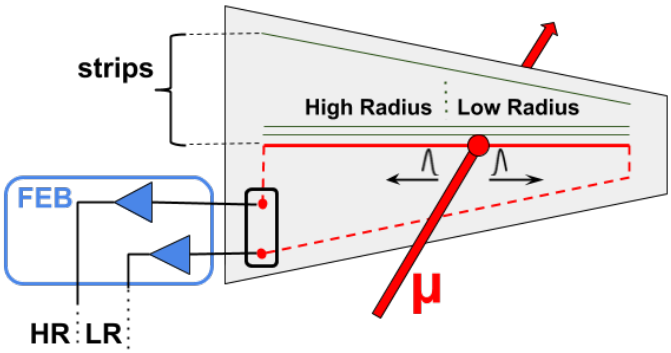

Figure 4-39: Schematic illustration of the way the iRPC works.

The time of arrival method is one of the straightforward ways to realize the measurement position along the strip. TDoA uses information about the difference of arrival time from both ends of the pickup strip (Fig. 4-40). To estimate the position along a strip (Y), one can use the following formula:

$$Y = \frac{L}{2} - \frac{v * (t_2 - t_1)}{2} \tag{4.12}$$

where Y is the position along the pickup strip. L is the total length of the strip. v is the transmission speed of the signal. t_1 and t_2 are the time arrival of the signal at the two ends of the strip.

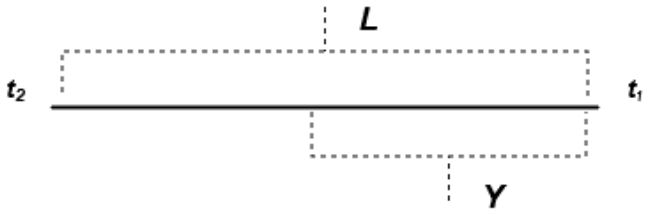

Figure 4-40: Schematic description of TDoA.

The resolution of the standard method is limited by the chamber design and is given by the RMS of a flat distribution ($L/\sqrt{12}$). In our technique and knowing the signal speed in the strips, one can find the time resolution and consequently the

[3]The approach for the position measurement is based on segmenting the pickup strips in several η partitions where each is read out by an electronic channel[108].

position resolution σ_Y in case of independent time measurements, as in our case, as follows:

$$\Delta t = t_2 - t_1 \rightarrow \sigma_{\Delta_t} = \sigma_{t_1}^2 + \sigma_{t_2}^2 - 2\sigma_{t_1}\sigma_{t_2} \rightarrow \frac{\sigma_{\Delta_t}}{\sqrt{2}} \rightarrow \sigma_Y = \frac{v * \sigma_{\Delta_t}}{\sqrt{2}}, \tag{4.13}$$

The difference between the two readout methods mentioned above is illustrated in Figure 4-41.

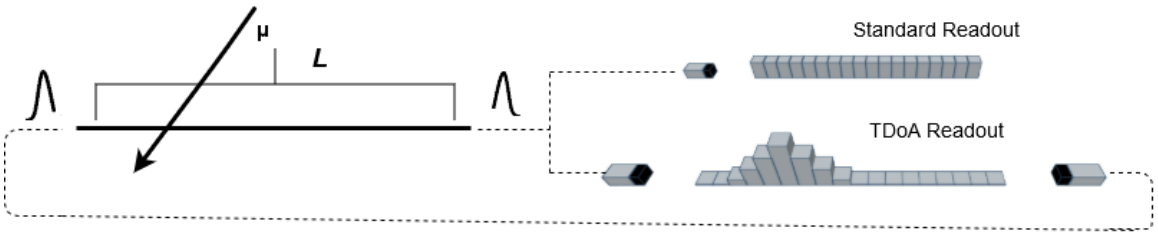

Figure 4-41: Schematic description of TDoA and standard readout (Statistical View).

The resolution of position along the strips when signals are read out from both ends of the strip and processing their arrival times by TDoA method is only limited by the electronics performance and to a less extent the detectors' one (See Ch. 5.5).

Based on this approach, our Front-End Board was conceived to provide two different arrival times (t_1 and t_2) corresponding to the arrival time of the signal to the two ends of the strip. Their difference provides then the position of the signal along the strip. Using the signal speed propagation, one can use the sum of the two times to check that this corresponds to the strip's total length. Once the position is determined, one can use it to estimate the time of the particle hitting the detector with respect to a reference time t_0 provided by the LHC machine.

These two simple operations could be done directly in the same FPGA and therefore implemented in the final version of the readout electronics system. In our tests, these two operations were performed off-line. To illustrate how to read a signal from the iRPC, we can consider the scheme of Figure 4-39 that shows how the signal is read out after a charged particle has passed (a muon for instance). The avalanche's charge induces a signal on the strips, and then the FEB will register two different arrival times for each strip. These times are then used to measure the particle's position.

4.4.1 iRPC Data

The validation of the readout system can be made with the help of a trigger system (See Ch. 5.1) consisting of several scintillator-PMs. This scintillator-PMs configuration provides a trigger signal that can be injected into one channel of TDC. Thus, recorded events correlated with the external trigger correspond to charged particles crossing the detector in the same region. To select these events, we start by plotting the hits profile as a function of the difference of their arrival time and that of the trigger signal ($T_{side} - T_{trig}$). We determine the two time windows for which there is a significant accumulation. These two time windows correspond to hits collected from the two sides of the strips. We then check that the time difference of hits belonging to the two time windows is coherent with a signal seen from the two ends of a strip and produced by particles crossing the detector where the scintillators are placed.

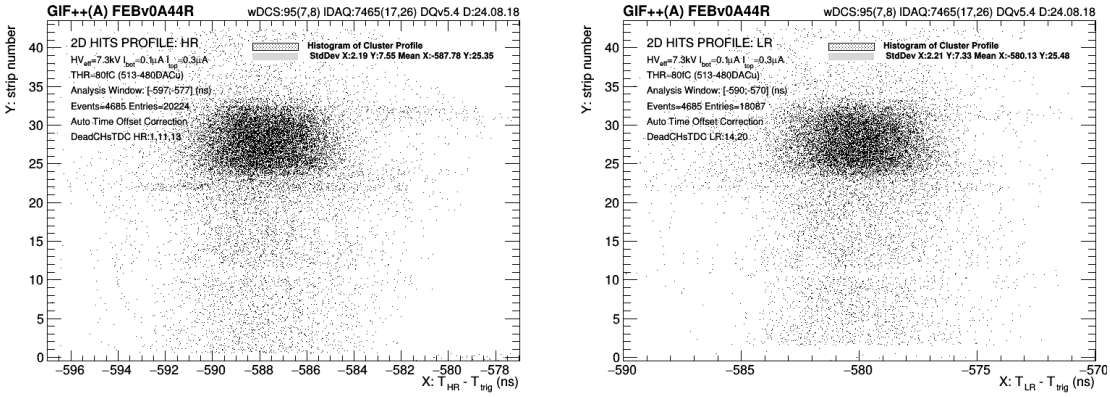

Figure 4-42: Example of hits profile showing the number of strips vs ($T_{side} - T_{trig}$). Left: Profile of hits associated to the High Radius channels. Right: Profile of hits associated to the Low Radius channels.

The histograms of all received hits by all the strips in the associated time delay relative to the trigger are present for the High Radius side (Fig. 4-42, left) and Low Radius side (Fig. 4-42, right). They show that the position of scintillators overlaps the strips numbered 24-34 (Y-axis). The position along the (X-axis) is determined by the trigger time delay with respect to the signal arrival time. In this case, the trigger signal is occurring with a delay of about 580 ns with respect to the strips signals detected from the High Radius side.

When the arrival times of two hits collected from the two sides of a strip are in the time interval corresponding to the external trigger, their time difference $t_2 - t_1$ is then determined as shown in Figure 4-43.

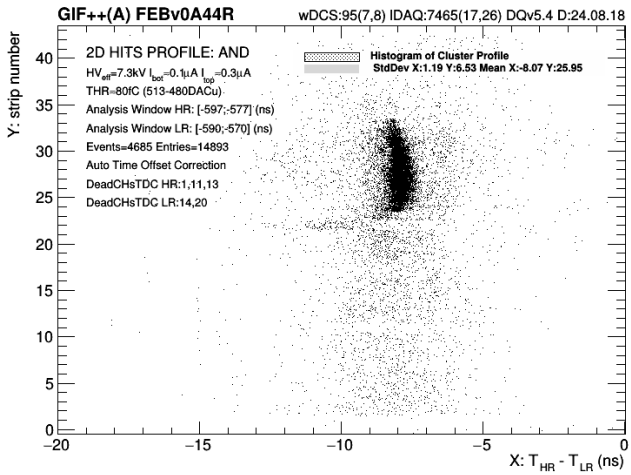

Figure 4-43: Example of hits profile in iRPC prototype. The fired strips are shown against the arrival time difference $t_2 - t_1$.

From the distributions shown in Figure 4-42 and Figure 4-43, we see that several strips may be fired by one particle that is behind the trigger signal. The number of strips fired by a particle is called multiplicity. This is presented by the histograms of Figure 4-44.

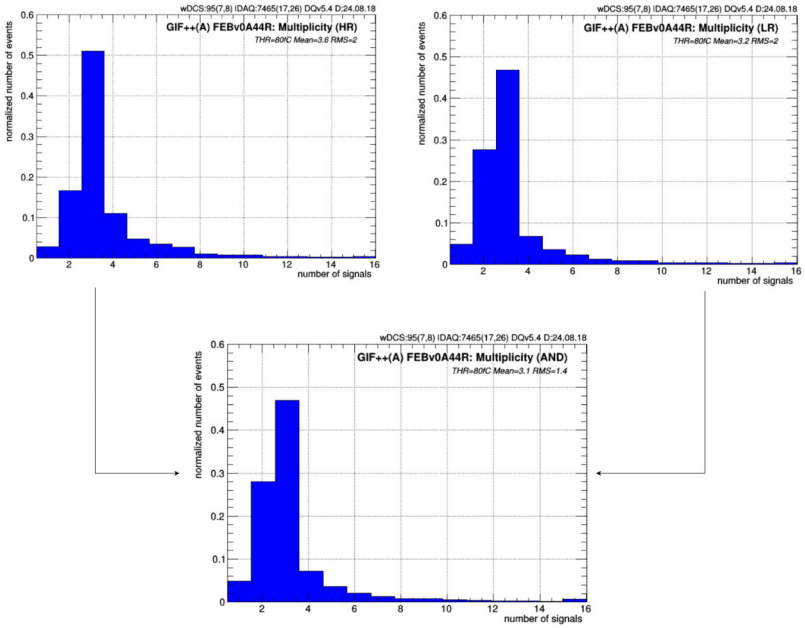

Figure 4-44: Example of a hits multiplicity in test beam data of an iRPC equipped with FEBv0 board. A charge threshold of 100 fC was applied.

The multiplicity of the tested iRPC was found to be approximately equal to three strips per trigger. Also, it is essential to mention that the multiplicity for strips with two signals from both ends is dominated by the number of hits of the side that

receives the smaller signal[4]. The number of hits per trigger depends on the strips PCB's geometry and the charge threshold. The charge, in turn, depends on the gas gap's thickness. It's important to mention that to reconstruct positions from this type of raw data, we have to associate hits in clusters.

4.4.2 Offsets Correction

An important part of the calibration is to remove the time offset between channels that are due to the different time delays in each channel TDC as well as the different lengths of strips[5]. This could be done in two ways: direct injection of signal that to be carried out with the calibration tools to be used in the final version of the chamber. The other possibility is to determine the values of offset shifts with the help of trigger setup. If the scintillators cover a given Y position of all the strips, the muon beam's profile should be aligned on the mean value of the time (or position) of the reference strip.

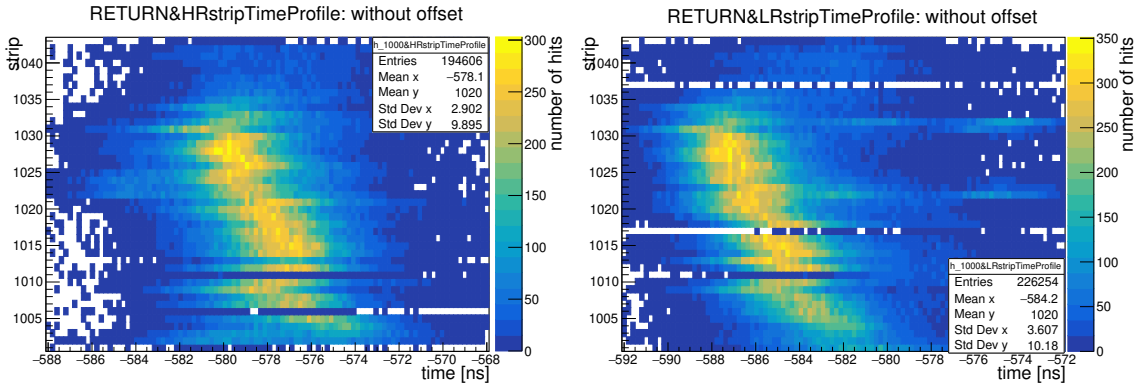

Figure 4-45: Profiles of the arrival time of HR channels (left) and LR channels (right) with respect to the trigger time before offsets alignment.

Before calibration, strips have a relative shift among each other (Fig. 4-45). With sufficient statistics to estimate the mean of hit time distribution in each separate channel accurately, the offset correction for channels can be estimated using the formula 4.14.

$$offset_{ch_i} = mean_{ch_i} - mean_{ch_{ref}}, \tag{4.14}$$

where ch_i is the channel index; here ch_{ref} is the reference channel (the channel found with the highest number of hits).

An example of time profiles with offset correction is shown in Figure 4-46.

[4]This is usually the Low Radius side.

[5]The total strip length including the return part were conceived to have almost the same value. However the geometrical constraints do not allow to have them identical.

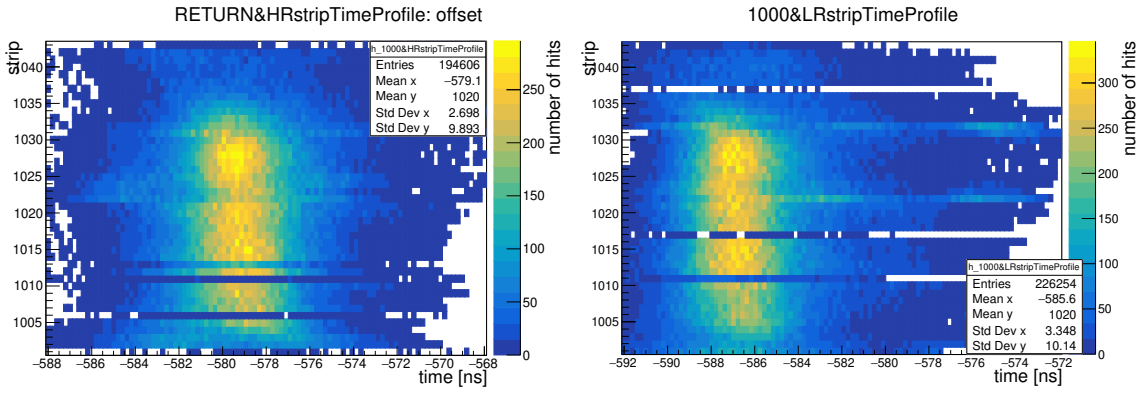

Figure 4-46: Profiles of the arrival time of HR channels (left) and LR channels (right) with respect to the trigger time after offsets alignment.

This alignment procedure with the trigger setup has not given an excellent correction of the offsets because of the scintillator's width, which was about $1 - 2$ cm. The result obtained with this calibration method indicates a value of about 0.2 ns of time resolution on the time difference (Fig. 4-47).

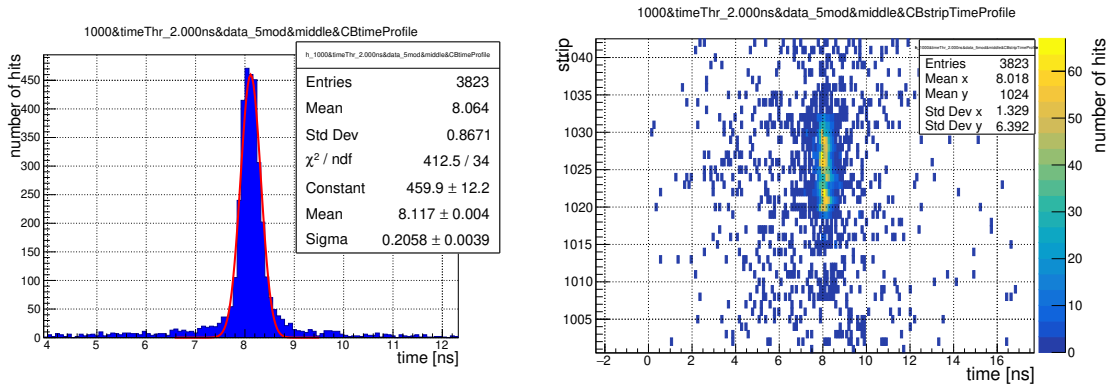

Figure 4-47: Left: Time distribution of iRPC after offsets correction. Right: Time-strip profile of iPRC after offsets correction.

Once we correct for the time offsets present among the different channels a clustering algorithm maybe be applied.

4.5 Two Dimension Clustering Algorithm

Using the arrival time difference method for the position determination requires a new clustering algorithm since one particle may fire several strips at the same time. The present algorithm is based on space clustering within one bunch-crossing. The new approach of reading iRPC strips gives time information that can be used to improve the clustering algorithm.

One of the possible algorithms that can be used is based on the following steps. The first step consists of calculating the arrival time difference (Δt) for all strips that are fired from both ends, and the second step is to perform clustering in time and space for all strips. It is essential to point out that when one side has more fired channels than the other side, we do not take into account these single-side-fired strips. This information loss may cause a slight bias in the cluster size measurements. As a result, we consider another clustering method, which allows the processing of all hits.

The new clustering approach (Fig. 4-48, Eq. 4.15) is based on grouping all hits from one side on the one hand and those of the opposite side on the other hand separately. Next, we associate the clusters of the two sides. In this case, we keep all the hits in the clustering process. When the chamber is fired, all collected hits are split into the two detector's corresponding sides, forming two data sets. The sets are processed independently in different threads to find intermediate single side clusters. Then, clusters of the two sides are associated with each other in the last step: finding optimal couples of clusters for HR and LR sides by minimizing the signal arrival time difference associated to the cluster of each side.

The output of this clustering is to keep only associated clusters to be used for position reconstruction. Also, we can keep groups of one-sided clusters (without a matching cluster from the opposite side), which cannot be used for position measurement but can be exploited for further detector studies such as signal loss along the strips and detector noise. The present algorithm has several parameters that must be fine-tuned and set with the correct values. These parameters include three different time thresholds for the association of fired channels. The first two thresholds we call LR and HR thresholds. These two values are related to the first step of clustering fired channels of each side independently. The last parameter is the time threshold for the association of a couple of clusters from both HR and LR sides. This parameter is mainly related to the studied area as well as the detector resolution.

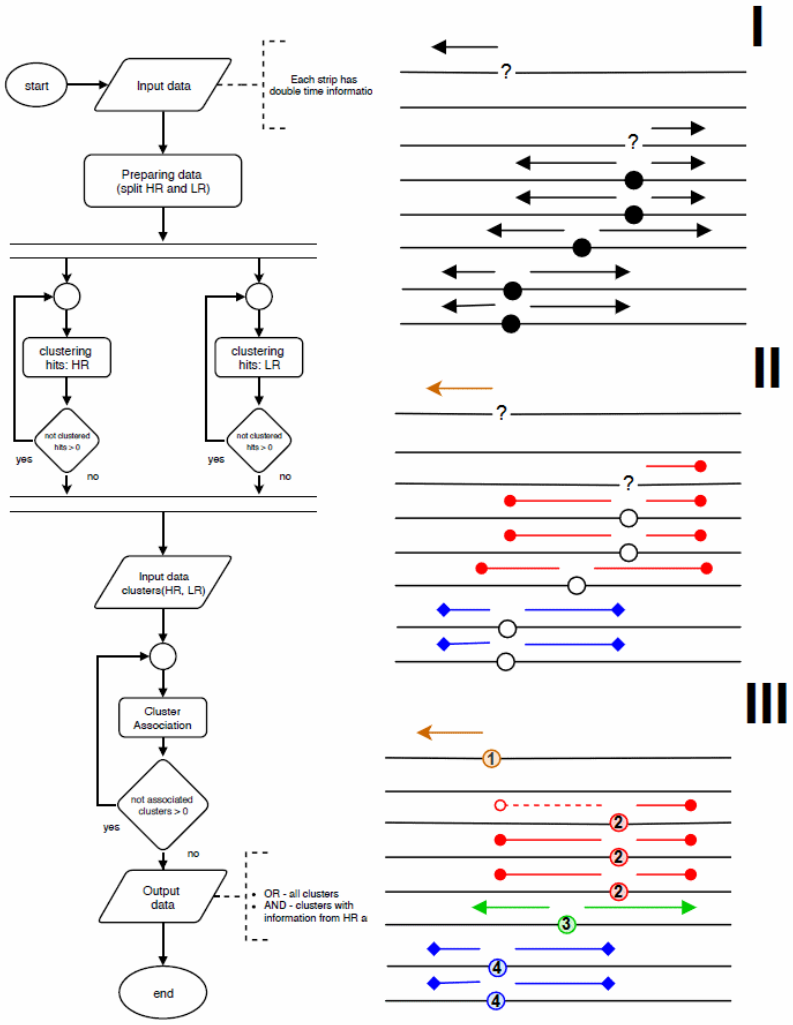

Figure 4-48: Left: Block scheme of two-dimension clustering algorithm. Right: Example of clustering: I is input data; II is High and Low radius clustering; III is the clustering result.

An example of clustering data for several scenarios is shown in Figure 4-48. It should be noted here that this example is showing several groups of fired strips for illustration purposes.

In Figure 4-48, received signals are shown as arrows, strips are lines, and dots indicate the position of the hits determined by the information of both detector sides, while question marks (?) indicate the position of a hit with only one-sided information. At the first stage, we collect signals for the fired strips. The second stage is grouping hits by the side. During this stage, signals are merged in clusters based on time arrival information. In the third step, all clusters are associated with matching pairs from the opposite side.

If necessary, it could be split back in the case of a couple of positions for individual strips outside the given time threshold of the last step. At the end, the procedure provides the information of the different categories of clusters: The first is the single-

sided clusters without information of position along the strip (y position); the second is the clusters with some of the strips without position information; the third is the clusters that were split back in the third step of the clustering; Fourth is the standard clusters which are two-sided fulfilling the time constraints.

The algorithm of the above mentioned approach can be written in the following way (Eq. 4.15, Eq. 4.16), the same clustering procedure applied for High Radius (h) and Low Radius (l), and the result of this clustering is processed to associate them (a).

$$l_n, h_n = (min_{(i,j\in N(S)),(i\neq j)}(abs(t(s_i) - t(s_j))) < \text{limit}) \wedge (p(s_i) = p(s_j) \pm 1))) \quad (4.15)$$

where, l_n and h_n are clusters for low radius or high radius (Set of strips); $p(strip)$ is function of position (strip number); $N(set)$ is return number of object in set; $t(strip)$ is return time of arrival of hit, i and j are the indices to account for all combinations of strips.

$$\begin{gathered} a_n = max_{(i\in N(H)),(j\in N(L))}(H_i \cap L_j) \wedge \\ (min_{(i\in N(H)),(j\in N(L))}(abs(t(H_i) - t(L_j))) \in [low; high]) \wedge \\ (max_{(ii\in N(h)),(jj\in N(l),)(p(h_{ii})=(p(l_{jj}))}(abs(t(h_{ii}) - t(l_{jj}))) < limit) \end{gathered} \quad (4.16)$$

where, a_n is the associated cluster (Set of strips); low, $high$ are given time ranges for which the association is possible; $p(strip)$ is the position determined by the strip number; $N(set)$ is the return number of the object in the set; $t(cluster)$ is the return time of arrival of the cluster.

4.5.1 Definition of Time of Arrival and Center of Cluster

The typical mean value of number of strips fired per one particle, i.e the multiplicity, is three (Fig. 4-44). Therefore it is necessary to define the center of each cluster. Two different definitions of the center could be given. One is the "average" and the other is the "central". In the case of the former we introduce the two following definitions:

$$\Delta T = \frac{1}{n}\sum_{i=0}^{n-1}\delta t_i = \frac{\delta t_0 + \delta t_1 + \cdots + \delta t_n}{n} \quad \text{CP} = \frac{1}{n}\sum_{i=0}^{n-1} s_i = \frac{s_0 + s_1 + \cdots + s_n}{n} \quad (4.17)$$

where, ΔT is the cluster delta time; δt_1 is the strip delta time; CP is the values of cluster position in strip number units; s_i is the strip number and n is n the umber of strips with both signals (HR, LR) or strip with only one side signal.

In the case of the central approach the two previous quantities are given by equation 4.18 and equation 4.19.

$$\Delta T = \begin{cases} \delta t_j, j = \frac{1}{n}\sum_{i=0}^{n-1} i; n = \{2k : k \in Z\} \\ \frac{\delta t_{j+0.5}+\delta t_{j-0.5}}{2}, j = \frac{1}{n}\sum_{i=0}^{n-1} i; n = \{2k+1 : k \in Z\} \end{cases} \quad (4.18)$$

$$CP = \begin{cases} s_j, j = \frac{1}{n}\sum_{i=0}^{n-1} i; n = \{2k : k \in Z\} \\ \frac{s_{j+0.5}+s_{j-0.5}}{2}, j = \frac{1}{n}\sum_{i=0}^{n-1} i; n = \{2k+1 : k \in Z\} \end{cases} \quad (4.19)$$

CP is the cluster position in strip number units; s_j is the strip number; n is the number of strips with both signals (HR, LR) or the strip with only one side signal.

The proposed clustering method considers the vast majority of issues that arose during the development of prototypes. Ultimately, it will be further optimized with the improved calibration of the front-end electronics, which will optimize the clustering parameters by accurately aligning all channels. The study presented here corresponds to the area of the iRPC associated to the trigger's scintillators one (Fig. 4-49) whose hit profiles were shown in Section 4.4.1 and where the two definitions were applied and compared.

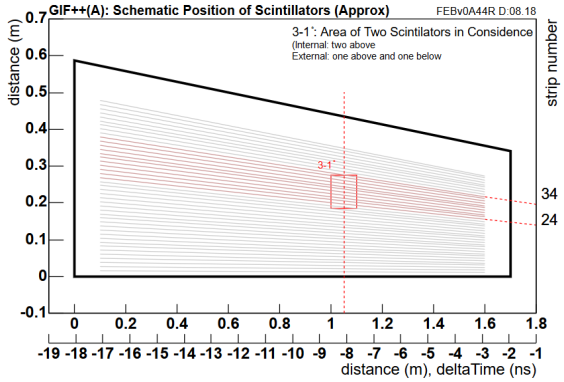

Figure 4-49: Schematic of the scintillators position with respect to the studied iRPC.

Figure 4-49 shows the location of the beam profile corresponding to the trigger zone, built using both the central and the average approaches.

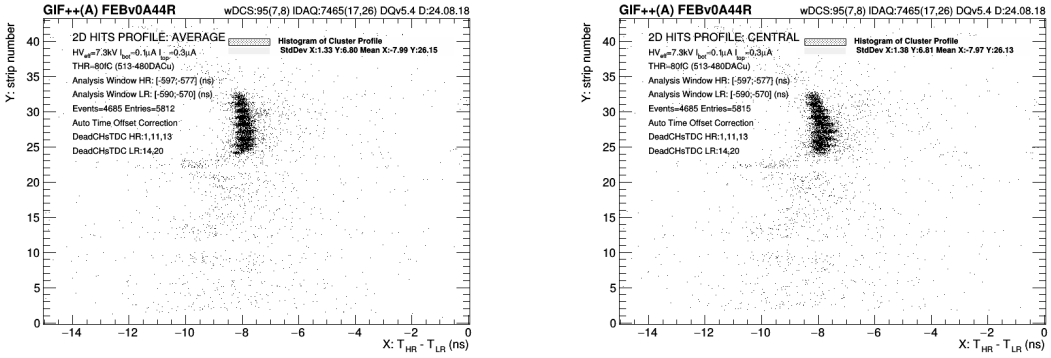

(a) Average definition.

(b) Central definition.

Figure 4-50: Cluster profiles with different definitions of position and time.

It should be mentioned that the "central" definition is based on using the signals that have the highest amplitudes. These signals are less impacted by the walk time effect that is more important for low-amplitude signals. Figure 4-51 shows the distribution of signal delay between strips from the same cluster made of three strips. The top three plots show examples of events with a different number of signals per

event. The three lower plots correspond to the same events, but the time of arrival is indicated for the opposite side.

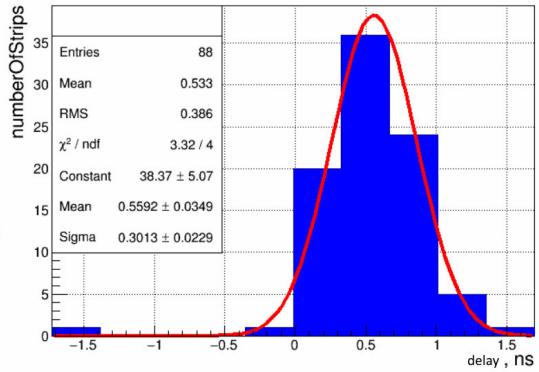

Figure 4-51: The distribution of the relative time delay of the strips belonging to same cluster.

The average delay value is found to be 0.53 ns. A few examples of events with different kinds of clusters are shown in Figure 4-52, where the upper figures correspond to HR side and the lower to the LR one. The Y-axis is the strip number, and X-axis is the time of arrival. The color distinguishes the signals that belong to the same cluster. From these examples, we can see that the central strip (Fig. 4-52, right) occurs before the others.

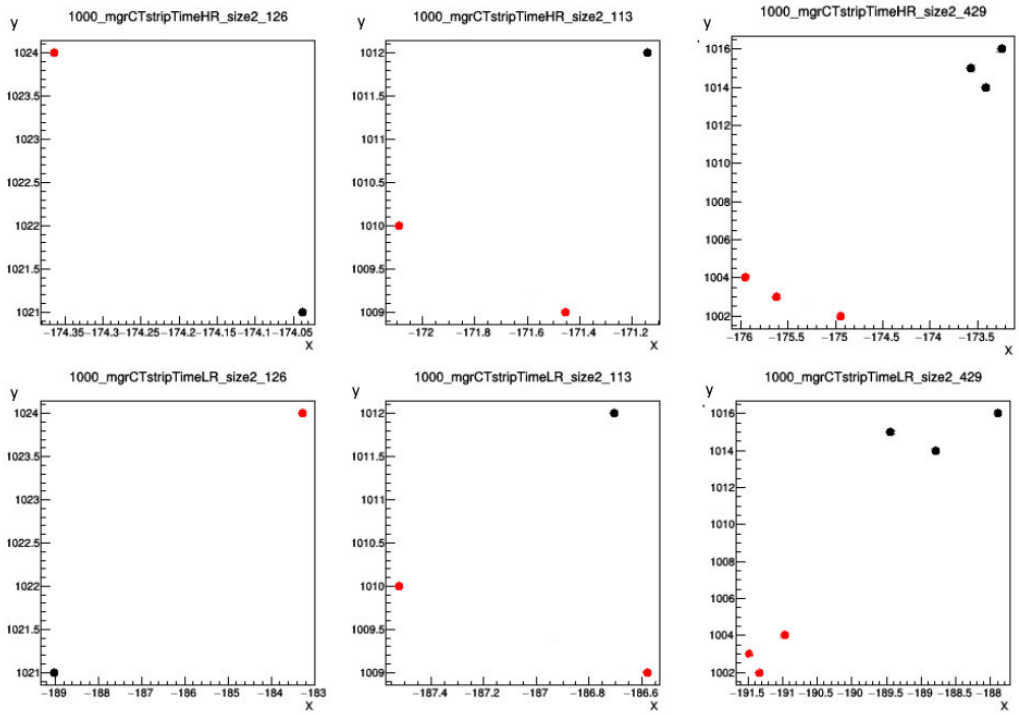

Figure 4-52: Examples of clusters. Left: Cluster size is one. Middle: Cluster size is two. Right: Cluster size is three.

4.5.2 Definition of Number of Clusters and Cluster Size

The cluster size and the number of clusters are important outputs of the clustering. Taking into account the signal delay due to different amplitudes and the alignment error, thresholds could be applied to the optimal value (about 0.7 ns) for each side allows us to cover all the possibilities of associating the couples of clusters from both sides (Fig. 4-53).

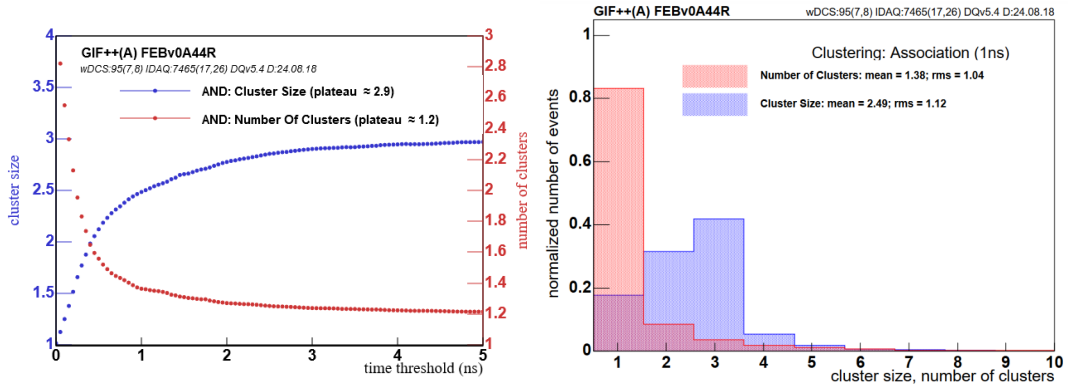

(a) Optimization of the time threshold.

(b) The cluster size and the average number of clusters.

Figure 4-53: Fine-tuning of clustering algorithm.

We can see that from typical triggers (Fig. 4-49) in our tests that the number of clusters per event is not equal to one. All events, with several clusters, have hits outside the main profile area. These hits create "tails". One group of strips without any additional hits should correspond to one particle of our trigger.

The presence of more than one cluster may result from atmospheric showers or interactions produced above our detector. To eliminate such events, a large scintillator that covers all the detector area not instrumented with the trigger setup should be added in a veto mode. In this way, only events associated to the passage of a single cosmic in our detector are kept. To achieve this, we modified our cosmic ray setup in order to have two different configurations of triggers (Fig. 4-54 without a veto (a) and with a veto (b)) signal. The veto configuration includes a large dimension scintillators-PM placed in the iRPC area but outside that covered by the trigger scintillator-PMs so that it can signal and then exclude any cosmic avalanches with multiple tracks of which at least one is located outside the area covered by the trigger sinctillators-PMs.

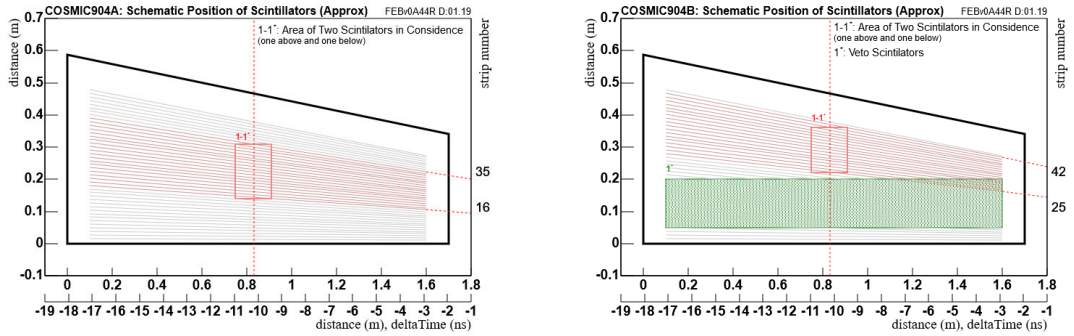

(a) without veto. (b) with veto.

Figure 4-54: Setup of scintillators.

With the veto system, the number of clusters per trigger is about one (1.03 to be compared with 1.38 without the veto). The cluster size and the number of clusters for spatial clustering after using the veto system are shown in Figure 4-55).

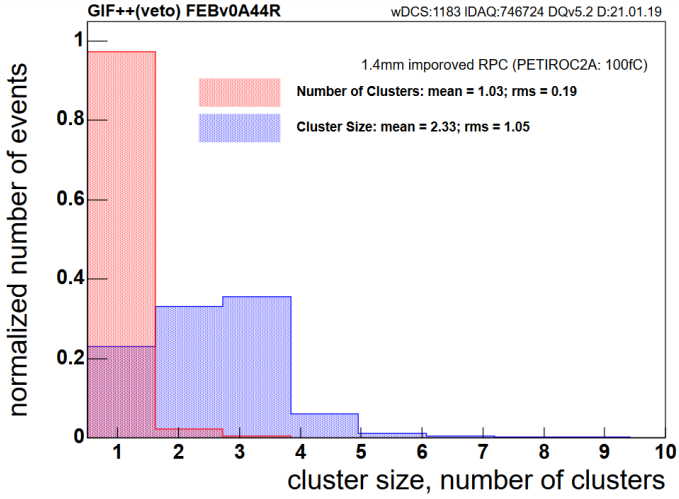

Figure 4-55: The cluster size and number of cluster from a trigger with veto.

.

Chapter 5

Capability and Performance of iRPC

The new prototype was characterized by several studies in different facilities at CERN and at IP2I that allowed us to have a list of iRPC characteristics such as operation threshold, time resolution, efficiency, rate capability, electronic noise and other parameters.

5.1 Facilities and Monitoring Detector Parameters

The characteristics of the developed detectors were studied in various conditions, which allowed us to measure and analyze all these detectors' parameters. The common setup consists of several scintillator-PhotoMultipliers (scintillator-PMs) and organizes according to the scheme shown in Fig. 5-1. They are placed before and after the chamber with respect to the beam direction.

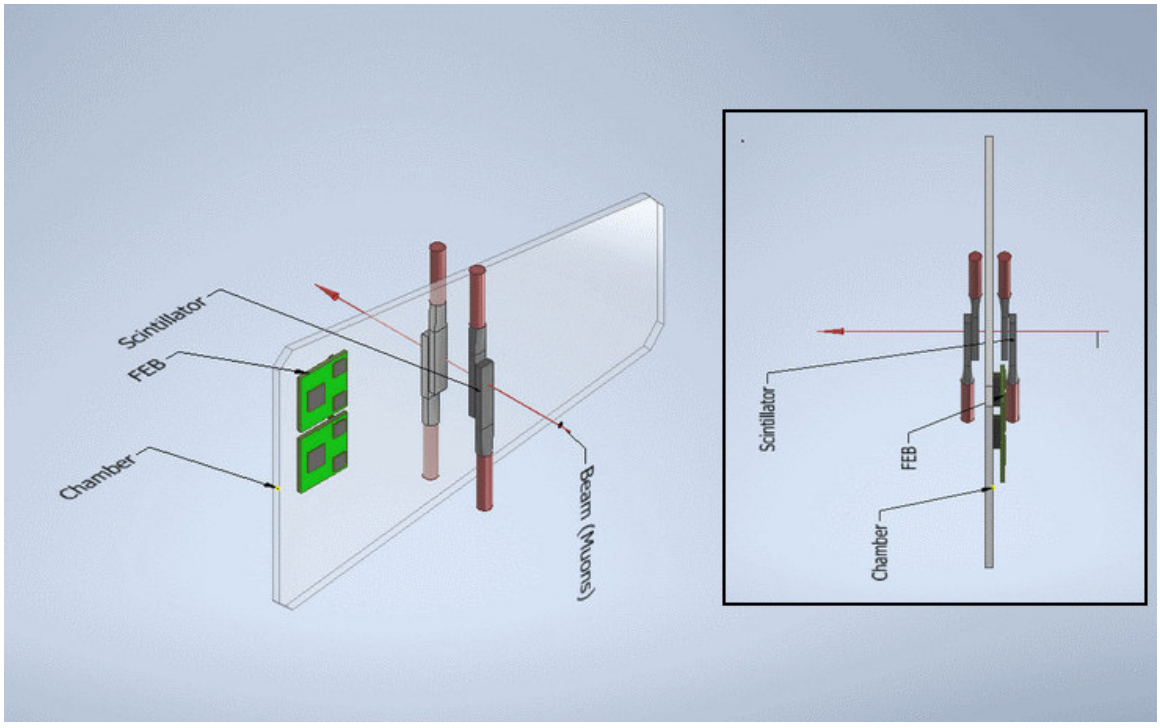

Figure 5-1: Schematic illustration of the scintillator-PMs setup.

The trigger logic (Fig. 5-2) of the setup generates a trigger signal (TTL level) when all scintillators-PMs give signals that have a coincidence in time.

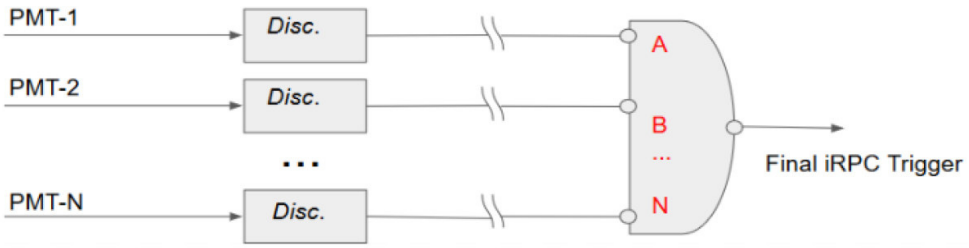

Figure 5-2: Example of a trigger logic of the scintillator's setup.

Mainly, iRPCs were tested with cosmic muons and beam from the SPS line. Rate capability analysis of chambers at a high background rate was carried out at GIF++ installations.

5.1.1 The Cosmic Setup

When a high-energy primary particle coming from space collides with the upper atmosphere's nuclei, it generates many particles that later interact in their turn. Among these secondary particles, there are short-lived positive and negative pi-mesons, which break down into positive and negative muons, respectively (Fig. 5-3). These muons may be tagged using a scintillator-PM system as a trigger and can then be used for the performance study of the iRPC.

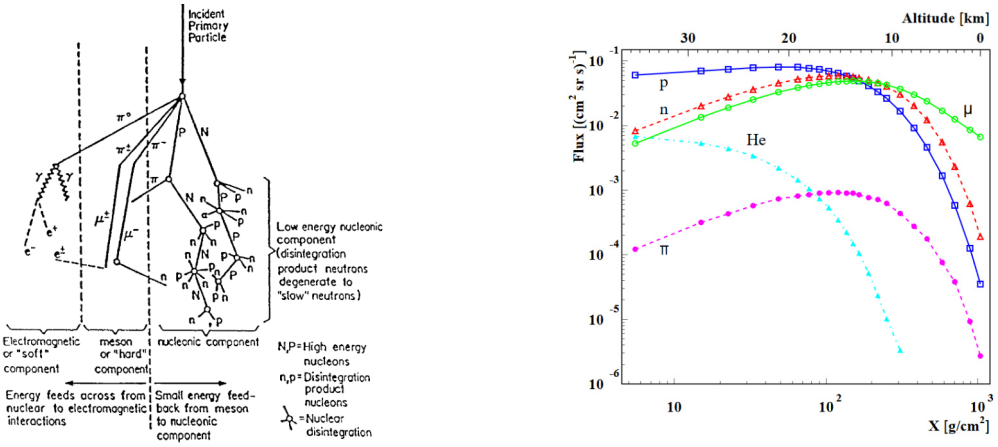

Figure 5-3: Left: A schematic representation of the typical development of the secondary cosmic radiations within the atmosphere arising from an incident primary particle [105]. The lines are drawn to guide the eye. Right: Total fluxes of muons, pions, protons, neutrons and helium nuclei as a function of atmospheric depth and altitude above sea level [67].

A typical cosmic setup includes two scintillation counters according to the scheme shown in Figure 5-1, but oriented horizontally to ensure the highest possible number of atmospheric muons. The profile of cosmic collected data is shown in Figure 4-43.

5.1.2 The GIF++ Setup

The GIF++ Facility

In order to test the detector at different background rates, the prototype was exposed to 100 GeV (mean energy) muons at the SPS H4 beamline and background gamma rays provided by the 13.9 TBq ^{137}Cs source at the Gamma Irradiation Facility (GIF++) [65] (Fig. 5-4). When the beam was absent, the iRPCs were tilted at an angle of 45°C to maximize the exposure to both cosmic rays and the source gammas.

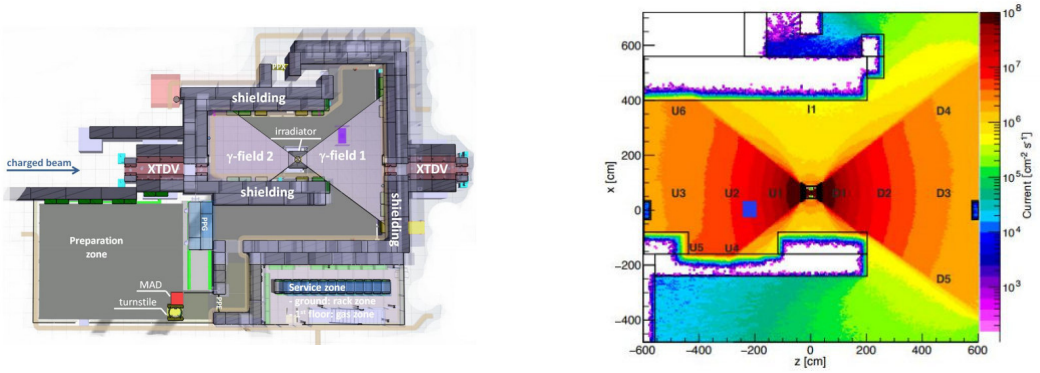

Figure 5-4: Left: The floor plan of the GIF++ facility with entrance doors MAD (Material Access Door), PPG (Personal Protection Gate), PPE (Personal Protection Entrance), PPX (Personal Protection Exit). When an electron beam is used by the GIF++ facility's halls downstream, a beam pipe is installed along the beamline between the vertical mobile beam dump (XTDV). Right: Photon flux in the plane through the source (XZ plane) at y = 0.65 m; attenuation filters at factor 1. With angular correction filters, the flux of 662 keV photons is made uniform within the YZ planes [94].

In 94.4 % of cases, the decay of $137Cs$ occurs with intermediate formation of excited barium-137 state (whose half-life is 2.55 min), which in turn passes to the basic state with the emission of a gamma of 661.7 keV. The total energy released at beta decay of one cesium-137 nucleus is 1175 keV:

$$^{137}_{55}\mathrm{Cs} \rightarrow {}^{137\mathrm{m1}}_{56}\mathrm{Ba} + e^- + \bar{\nu}_e; \quad {}^{137\mathrm{m1}}_{56}\mathrm{Ba} \rightarrow {}^{137}_{56}\mathrm{Ba} + \gamma \tag{5.1}$$

Thanks to appropriate collimators, the radiator covers two zones of ±37° horizontally and ±37° vertically. These two zones are called Upstream and Downstream, depending on their position in the bunker, with the muon beam direction. They can be irradiated independently by using two attenuating systems, consisting of 3 planes of 3 leaded filters each (A1, A2, A3, B1, B2, B3, C1, C2, C3). The shape of planes is designed to keep a uniform flux at a given z-axis, as Figure 5-4 shown. This is well adapted to the flat structure of muon chambers. On either side, the planes can be lowered or raised directly from the GIF++ control room in order to position the correct filters in front of the radiator (Fig. 5-5).

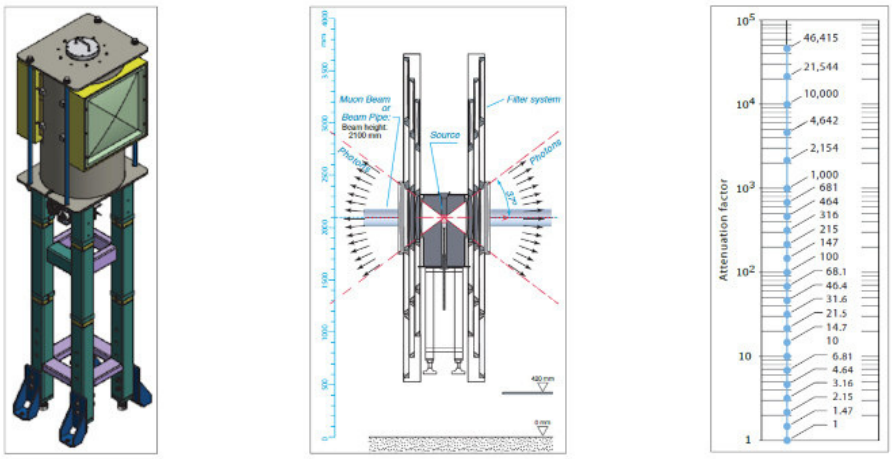

Figure 5-5: Left: The diagram of the irradiator. Right: The configurable attenuation values [94].

The Trigger System

The trigger system of the beam particles was built from four scintillators: two located outside GIF++ bunker area and two located inside the bunker (Fig. 5-6).

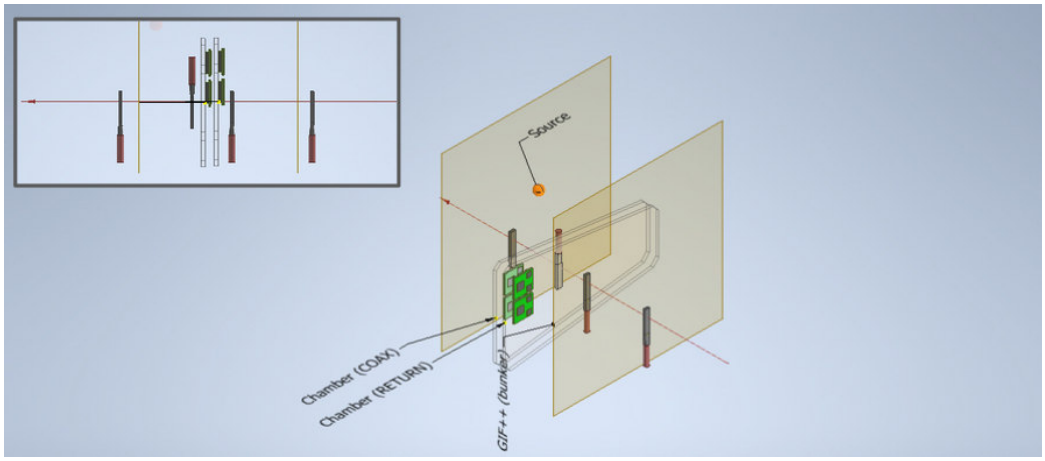

Figure 5-6: Setup in gamma irradiation facility for beam trigger.

The proposed scheme allows us to avoid any accidental triggering due to in-range coincidence signals within the scintillation counters induced by the source's gammas. The above trigger configuration provides the possibility to study the chamber efficiency in the presence of different background loads. Some examples of profiles for the signals obtained from the SPS muon beam with and without background rate are shown in Figure 5-7.

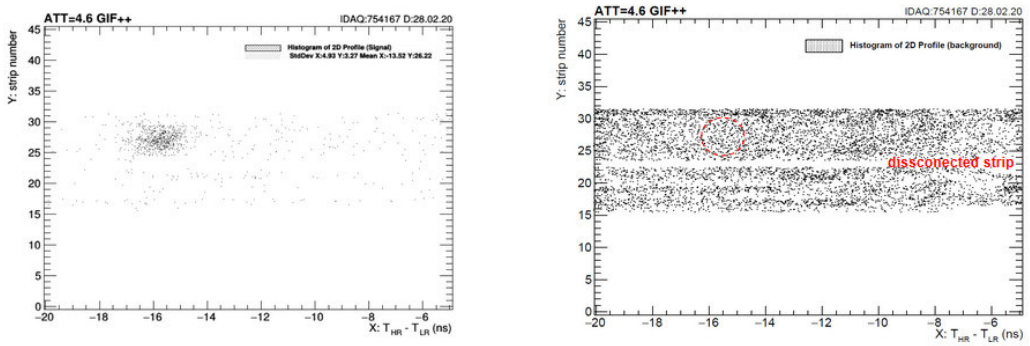

Figure 5-7: Example of profiles from GIF++ setup. Left: The signal profile as seen in our detector. Right: The background profile.

The Study of the Background Rate

To study the rate influence on iRPC behavior, the first step is to estimate the rate correctly. The simplest way is to calculate the number of gamma signals seen in iRPC detector gaps by time and surface unit (Fig. 5-8). The normalization of the obtained value is performed using the detector efficiency to gammas, which is estimated on the basis of the detector efficiency to muons, operated with only one gap[1] (Eq. 5.2).

$$CR = \frac{NC}{surface * time}; \quad rate_{norm} = \frac{CR}{efficiency_{gamma}}, \tag{5.2}$$

where NC is the number of clusters of one run; $surface$ is the active PCB zone; $time$ is the collection time, in case of a uniform flux.

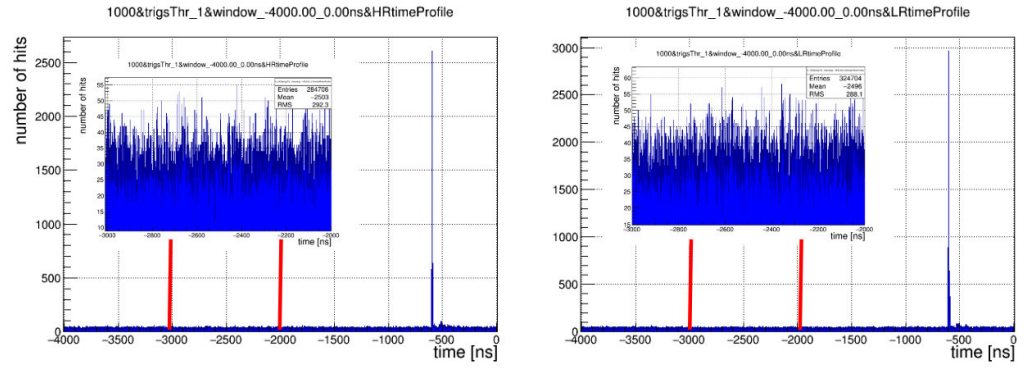

Figure 5-8: Example of a time window used for the estimation of cluster rate. Left: data from the high radius. Right: Data from the low radius.

The rate of gammas converted in the detector ranged from 0 to 3 kHz/cm^2 as shown in Figure 5-9.

[1] γ interacts in one gap only.

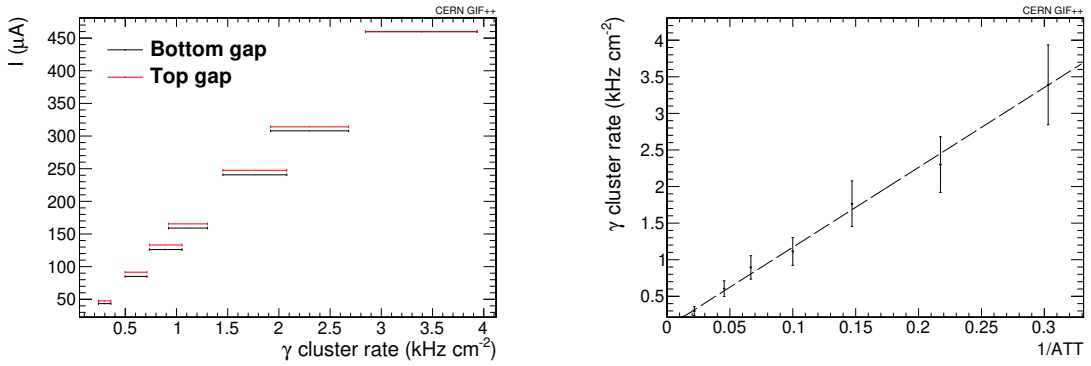

Figure 5-9: Left: The current in gap as a function of the rate of gamma cluster seen by the iRPC chamber. The current show the total charge of particles detected in GAP and absorbed from HRL electrodes. Right: The gamma background rate as a function of reciprocal of gamma attenuation factor (ATT).

5.1.3 Monitoring Conditions

The procedure to study the detector and electronics requires the measurements to be made at stable conditions of the setup. This control is critical, as the measurement can take up several days.

The principal scheme of the HV cables and gas pipeline routing for the detector prototypes is shown in Figure 5-10. In the detector prototypes, gas is circulated sequentially, so gas flows into one gap and out from another. Each gap has an individual power supply and is equipped with an RLC filter to avoid possible HV noise.

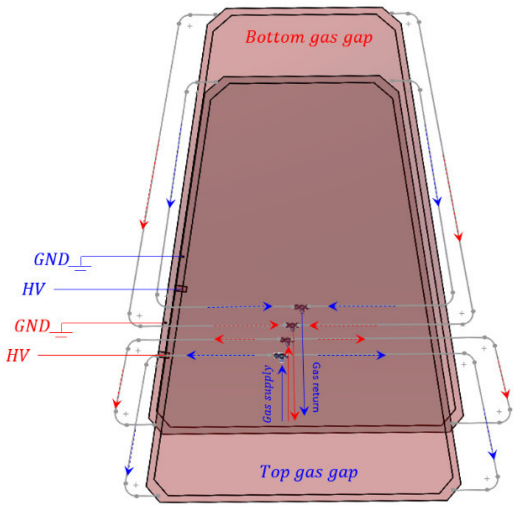

Figure 5-10: The scheme of the HV cables and gas pipeline routing of the prototype.

The high voltage is set with pressure and temperature corrections to avoid changes in the detector performance during measurements. To take into account the pressure

and temperature variations during the tests, effective values of the high voltage were calculated according to the following formula [92]:

$$HV_{app} = HV_{eff}((1-\alpha) + \alpha \frac{P}{P_0}\frac{T_0}{T}), \tag{5.3}$$

where HV_{app} is the high voltage applied; HV_{eff} is the effective high voltage; P is the local pressure; P_0 is a reference pressure (990 mbar); T is the local temperature; T_0 is a reference temperature (293.15 K); α is a correction coefficient ($\alpha = 0.8$).

A high voltage setting procedure is performed before operating the chamber. This procedure consists of increasing the high voltage in the gas gaps (Fig. 5-11) to estimate the current increase versus voltage increase in the same conditions of pressure and temperature.

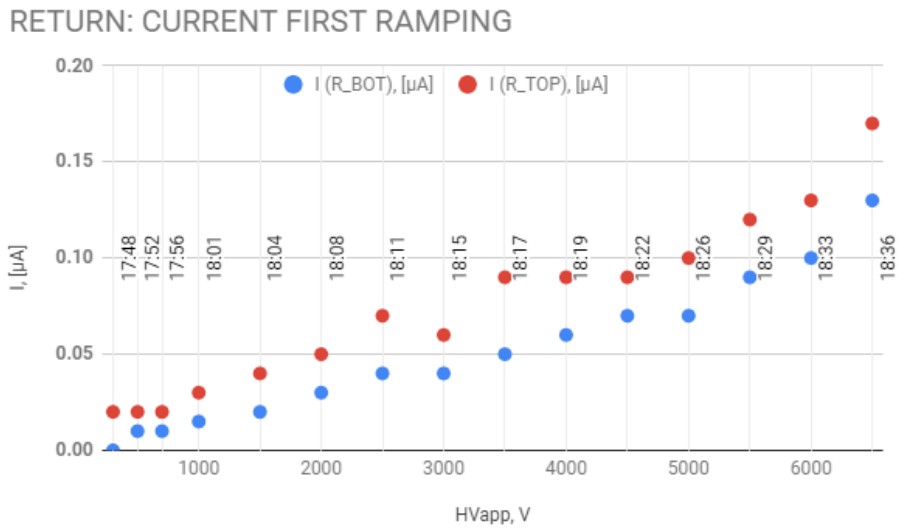

Figure 5-11: Example of current ramping of the bottom (blue) and the top (red) gaps.

The examples of monitoring parameters, such as temperature and gas humidity are given in Figure 5-12.

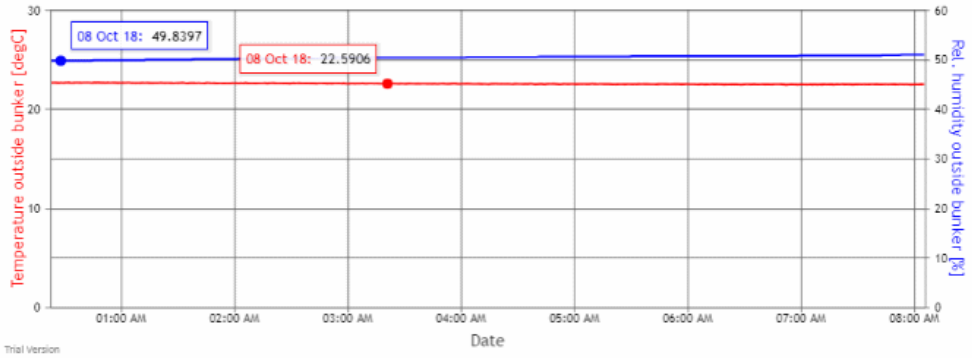

Figure 5-12: Examples of monitoring humidity and temperature.

5.1.4 The Data Acquisition System

The data acquisition is in charge of formatting the data received from the ASICs and the TDC and then sending them to a server to store them. For each event, the transmitted data (Fig. 5-13) include a header, a Global Trigger Counter (GTC), an Absolute Bunch Crossing ID (ABCID) and a payload for each fired channel. The payload (Fig. 5-14) includes the channel number, a coarse time, a fine time, and a Bench Crossing ID (BCID). The BCID is a counter that resets after each trigger.

Table 5-13: The structure of event.

Name	**Memory**	**Format (Example)**
Header	4 bytes	ca fe ba be
GTC	2 bytes	0 1
ABCID	6 bytes	0 7 23 19 f0 9
payload	8 bytes	channel BCID coarse fine
...	...	...
payload	8 bytes	channel BCID coarse fine

Table 5-14: The structure of the payload.

channel	**BCID**	**coarse (4 bytes 2.5 ns)**	**fine (2.5 ns/256)**
e	0 2	8 7c 22 6	38
10	0 7	8 7c 23 95	9d
2	0 2	8 7c 21 ff	f4

The software of data analysis with classes and functions that use ROOT tools [11] was developed from scratch. The analysis structure has a flexible interface that allows changing any parameter or adding a new block of code for a new study when needed. Also, a class based on ROOT TTree [19] was developed. This class reprocesses raw data with the format shown in Figure 5-15.

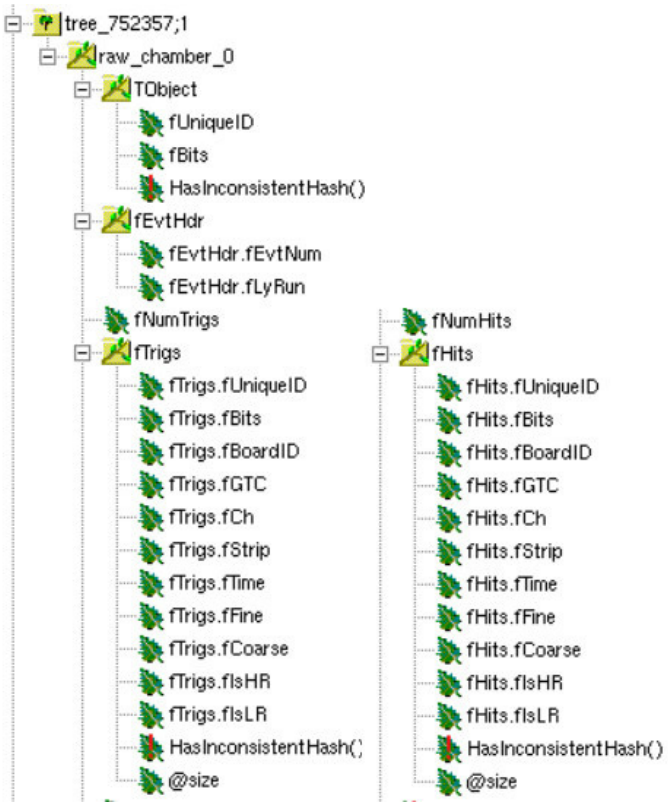

Figure 5-15: Structure of tree.

The connection between the two ends of a strip and the ASIC and TDC channels is used to process the raw data provided by the DAQ system to provide useful information for the analysis.

The tree structure also has additional information such as the operating conditions and study comments that allow us to perform more detailed studies.

5.2 iRPC Efficiency

Efficiency is estimated as the ratio of the number of detected muons to the total number of triggers. To be considered as a detected muon by the chamber, at least one strip should be fired from both ends. The signal arrival time of each of the two ends should be within a time window associated with the external trigger (Fig. 5-16). The width of each of these two windows about ten nanoseconds. This width depends on the area covered by the scintillators along the strips. The position of each of these two windows takes into account the delay in time between the PMs on the one hand and that of RPC signal detection by the channel associated with the strip's end on the other hand. The delay is related to the position of the scintillator-PM with respect to the RPC, the cable length and signal treatment in the scintillator-PM system.

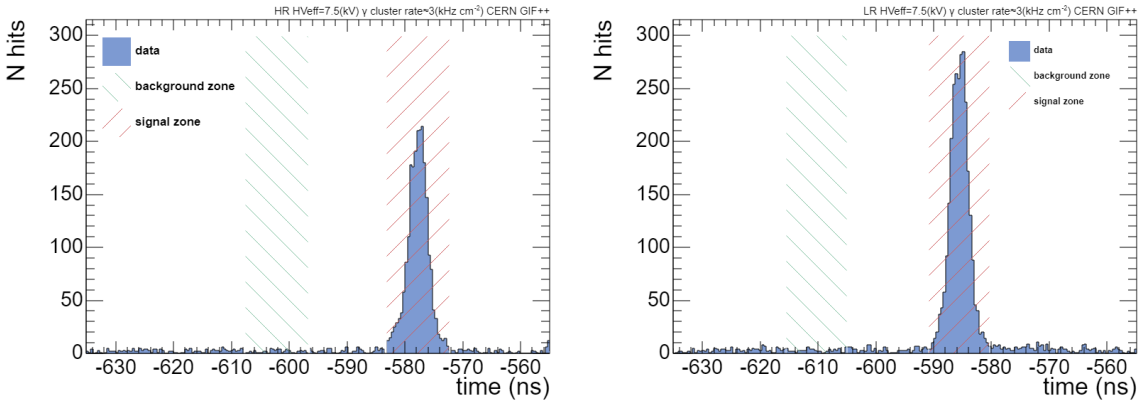

Figure 5-16: Illustration of a time window that was found from fitting a function for a high radius (left) and a low radius (right).

The size of the time window for the muon event counting is determined as the mean ±3 sigmas of a Gaussian fit (Eq. 5.4):

$$f(t) = \frac{1}{\sigma\sqrt{2\pi}} \exp\left(-\frac{1}{2}\frac{(t-\mu)^2}{\sigma^2}\right) \tag{5.4}$$

For each trigger, the signal associated with the passage of the muon counter is incremented if a hit is found in each of the two time windows mentioned above. However, gamma background hits can occur in these two time windows and fake our muon counting. Thus, to estimate the true muon efficiency (Eq. 5.5), we have to subtract this background contribution as follows, assuming that the background hits and muon hits are uncorrelated.

$$\varepsilon = \frac{\frac{N}{N_{trig}} - \frac{N_{bkg}}{N_{trig}}}{1 - \frac{N_{bkg}}{N_{trig}}}, \tag{5.5}$$

where ε is the true muon efficiency; N is the number of the muon events; N_{trig}, N_{bkg} are the numbers of the muon triggers and the number of the gamma background hits expected in the same time window, respectively.

When the charge induced by the passage of a muon is small, it is possible to detect the signal on only one end of the strip. The loss of the signal amplitude from the impact point to the strip's end explains this. To account for this kind of situation, we define the one end efficiency in the same way as before, but here we require the occurrence of a hit in one of the two time windows mentioned above. Thus, in addition to the efficiency defined before, we have two other efficiencies: the High Radius (HR) efficiency and the Low Radius (LR) one.

To determine the optimal HV Working Point (WP) of each prototype, we study their efficiency as a function of the applied effective high voltage. Therefore, High Voltage (HV) scans (Fig. 5-17) are performed. The variation of the environmental pressure (P) and the temperature (T) inside the experimental hall were taken into account using the formula (Eq. 5.3). The goals of the HV scan, as mentioned before,

is to study the efficiency as a function of the high voltage for all the iRPC prototypes to find the best working high voltage for every chamber but also to study cluster size associated to the passage of a muon as well as to estimate the noise rate. A typical efficiency curve as a function of the HV is shown Figure 5-17. This curve is usually well described by a sigmoid function:

$$\varepsilon = \frac{\varepsilon_{max}}{1 + e^{-\lambda(HV_{eff} - HV_{50\%})}}, \tag{5.6}$$

where ε is the efficiency at a given HV_{eff}, ε_{max} is the plateau of this fit function, λ is determined by the slope of the fit function at HV_{eff} corresponding to the 50% of the maximal efficiency. This can be expressed by the following formula:

$$slope = \frac{d\varepsilon}{d(HV_{eff})} = \frac{\lambda \varepsilon_{max}}{4} \tag{5.7}$$

To determine the working point, we use the following definition adopted by the CMS collaboration for the 2 mm gas gap RPC:

$$WP = HV(50\%) - \frac{log(\frac{1}{0.95} - 1)}{\lambda} + 150\ (V) \tag{5.8}$$

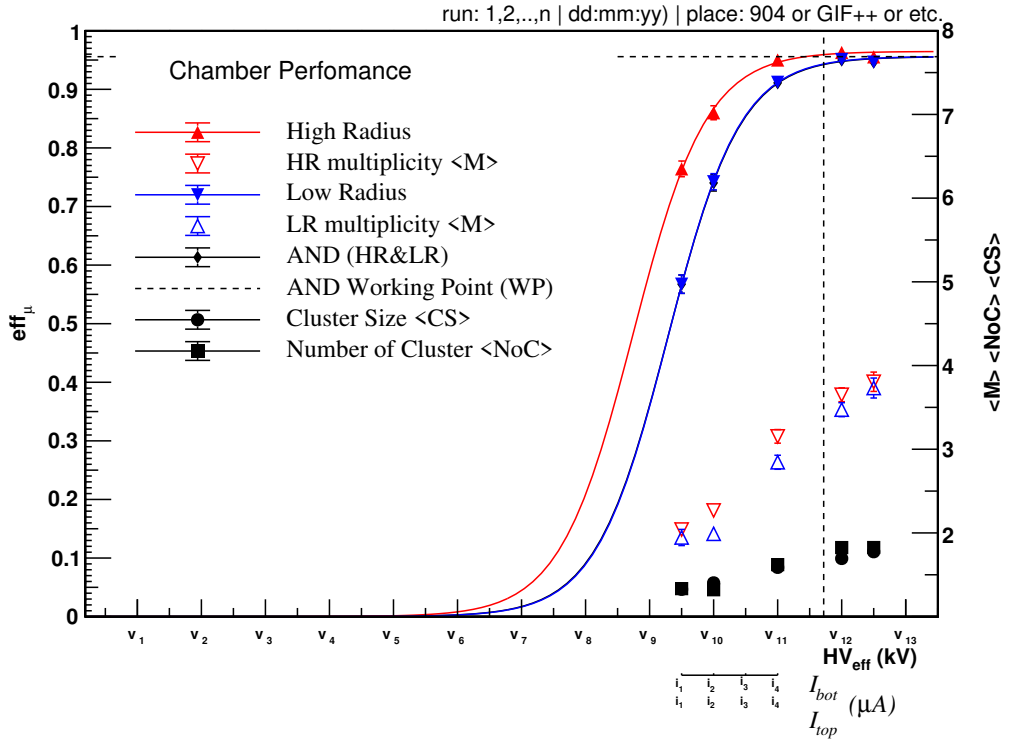

Figure 5-17: Example of a high voltage scan. Red is the efficiency related to the high radius side of the detector. Blue is that of the efficiency of the low radius side of the detector. Dark is efficient when position could be reconstructed.

Figure 5-17 shows three efficiency curves corresponding to the efficiency, the HR and the LR ones as a function of the high voltage. Also shown, the average number of clusters and the average cluster size as well as the average multiplicity associated to HR and LR (See Ch. 4.5.2).

5.2.1 Uniformity of Detector Efficiency

On the test stand, performance measurements were made to check the uniformity of the detector for each gap separately (Figures 5-19, 5-18) and also in the combined mode (double mode) (Fig. 5-20).

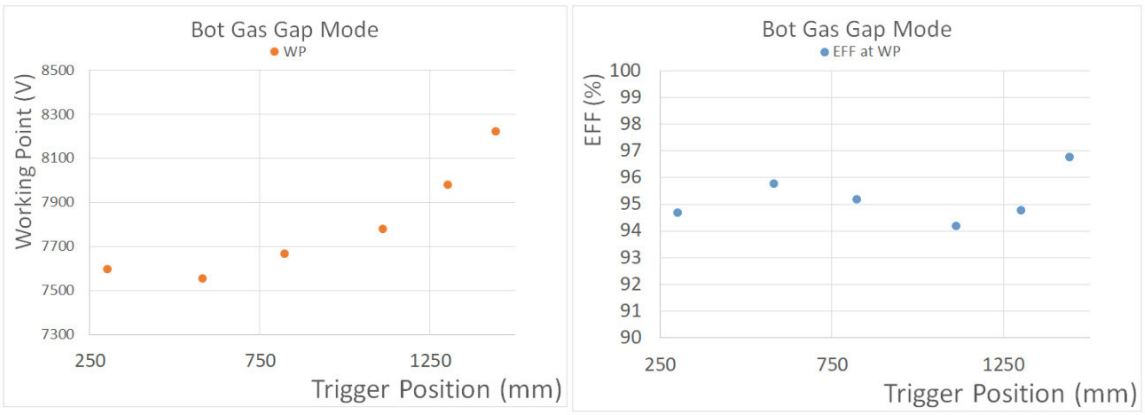

Figure 5-18: Efficiency and working point for the bottom gap for different positions along the chamber.

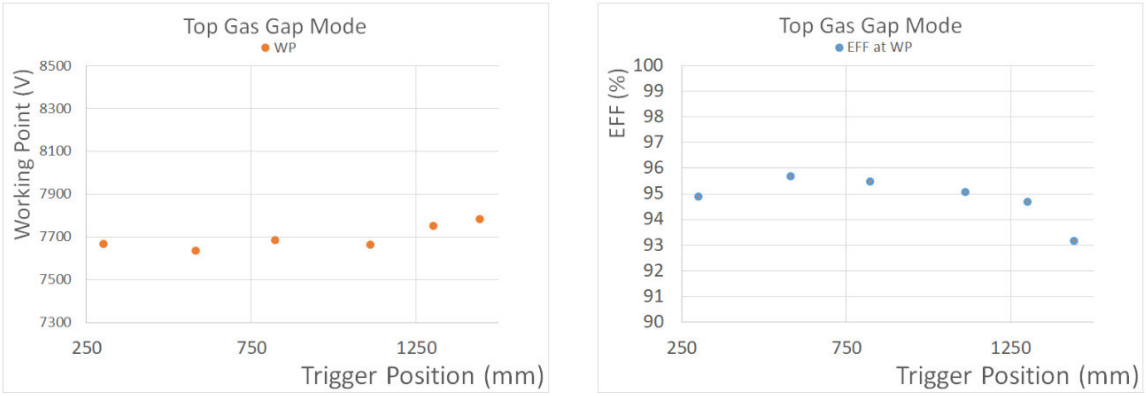

Figure 5-19: Efficiency and working point for the top gap for different positions along the chamber.

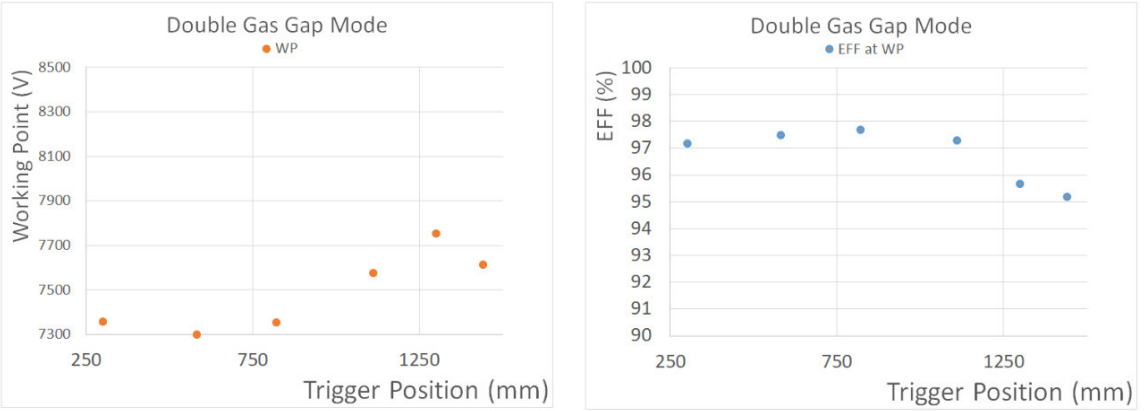

Figure 5-20: Efficiency and working point for the double mode for different positions along the chamber.

The previous plots show the efficiency and operating point dependent on the trigger position along the chamber's length. One can see that the efficiency is slightly degraded in the region located at 800 mm from the HR side.

This study shows that good uniformity of the efficiency is found except in a small part of the chamber, where a bending problem was found after an inspection. This indicates that possible problems with the cassette's mechanical structure may result in additional space between the gap and the strips PCB, which affects the performance of the system. By adding extra pressure to the cassette with several modifications brought to its mechanical structure, we were able to fix this problem. Following this study, the final cassette is designed to use an adequate mechanical structure to keep the gaps in good contact with the strips PCB to ensure uniformity without problematic zones. The following Figures (5-21, 5-22) show different results obtained during the study we conducted to understand and then to solve the gaps bending problem.

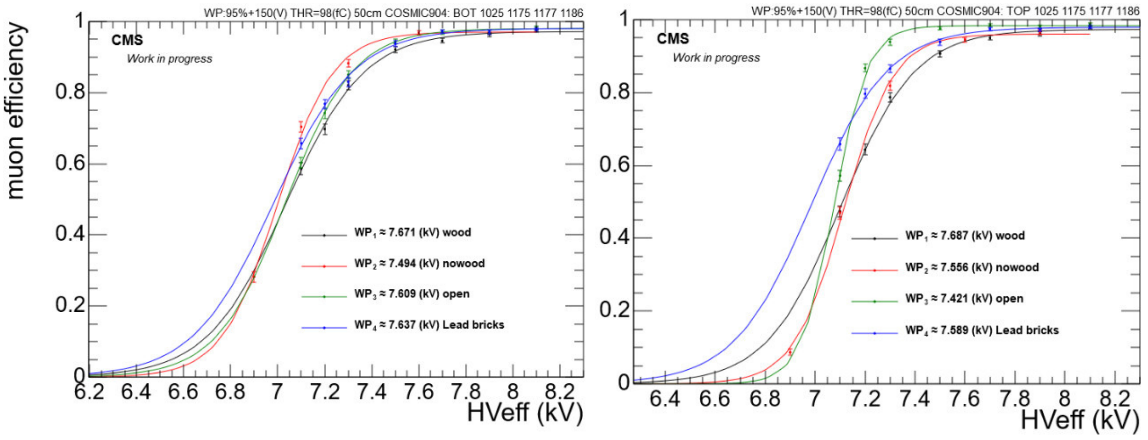

Figure 5-21: Study of the efficiency of the bottom (left) and top (right) gaps corresponding to several modifications on the cassette.

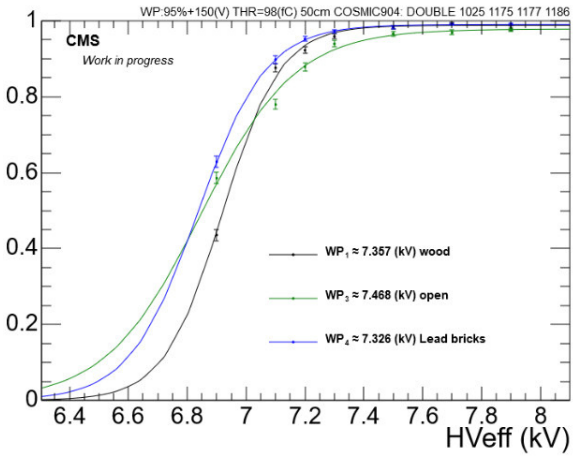

Figure 5-22: Study of the efficiency of the double gap mode corresponding to the same cassette modification as in Figure Figures (5-21, 5-22).

5.2.2 Efficiency of the Detector in the presence of a Background

To estimate the RPC detector efficiency independently of the pressure and the temperature variations during the beam exposure, effective high voltage values were used in our performance studies.

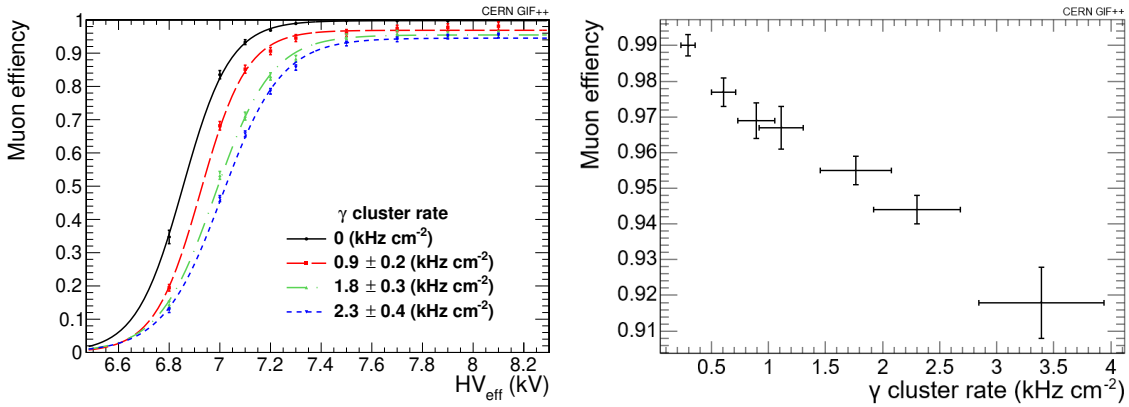

Figure 5-23: Left: Efficiency curves as a function of the effective high voltage for the prototype shown for different background rates. Right: Plateau efficiency of the studied chamber at different background rates.

Figure 5-23 shows the efficiency at different γ rates as a function of the effective high voltage applied to each of the gaps of the studied chamber. These results show that efficiencies around 95% are reached for a particle rate of 2 kHz cm^{-2}. The rate is estimated by counting the number of clusters of fired strips within a given time interval normalized to the instrumented surface and the measured efficiency. The definition of WP was analyzed when studying the dependence of WP on the background levels. This was optimized in such a way that the drop in efficiency at

the operating point with respect to its position on the plateau is independent of the background rate (Fig. 5-24).

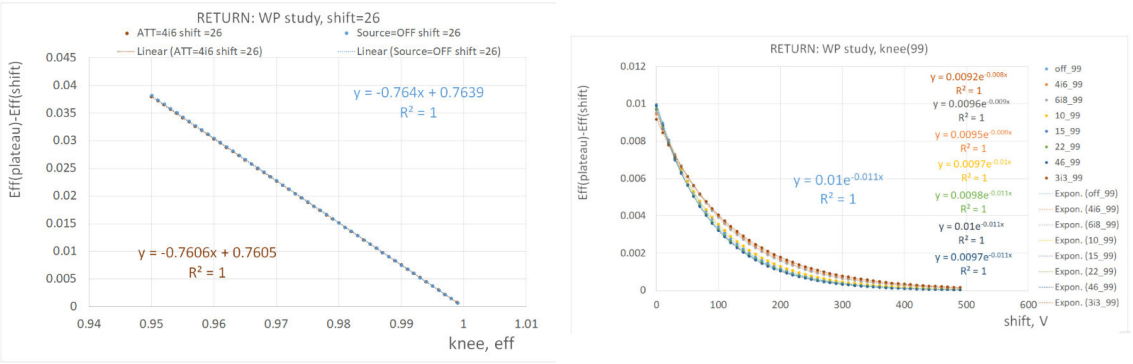

Figure 5-24: The optimization of the working point for the iRPC prototype.

From the results of this study we observe that the previous definition of WP given by formula 5.9 should be modified to take into account that our gas gap is reduced from 2 to 1.4 mm and also to be independent of the particle rate. The new formula could be put as follows:

$$WP = HV(50\%) - \frac{log(\frac{1}{0.99} - 1)}{\lambda} + 26\ (V) \tag{5.9}$$

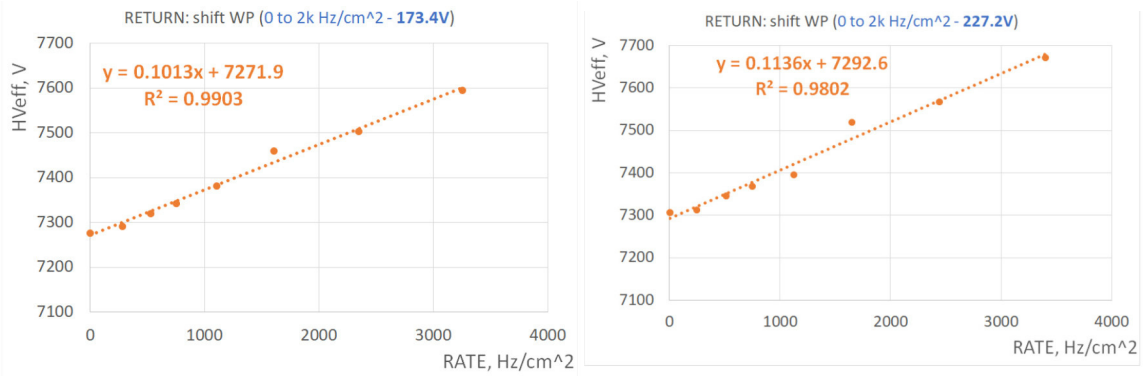

Figure 5-25: Study of WP shift vs background rate. Left: Using the standard (2 mm gas gap RP) definition of WP. Right Using the new definition of WP.

Figures 5-25 show the shift of the WP versus the background. A shift of $\approx$ 200 V is estimated for a particle rate of 2 kHz/cm^2.

5.2.3 Estimation of the FEBs limitation due to the Background Rate

In order to complete our performance study in 2019, we had to use cosmic muons in GIF++ because the SPS (beam) was switched off. Thus, to estimate the iRPC

readout's efficiency with the FEBs, a setup made up with three scintillator-PMTs protected from the gamma source by lead bricks, was used to provide an external trigger for our study (Fig. 5-26).

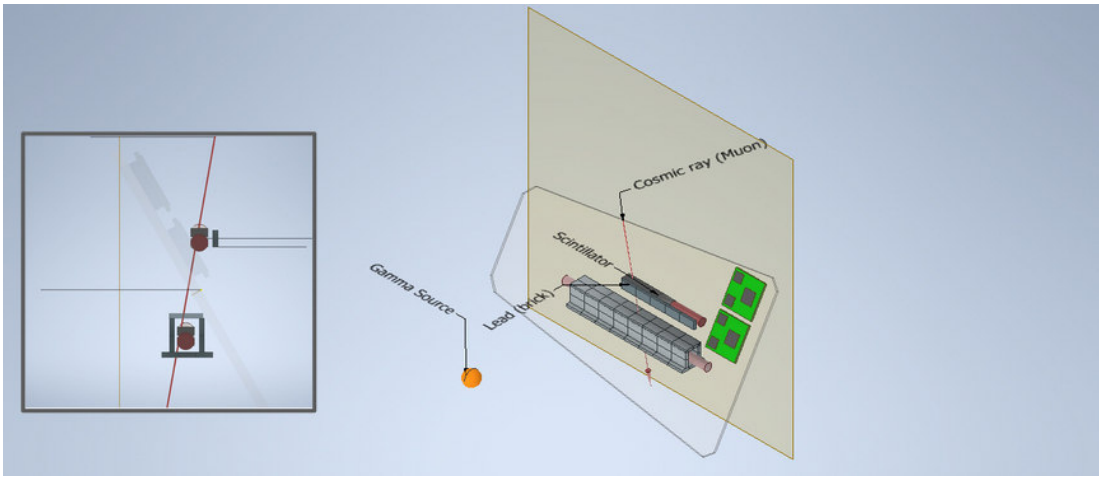

Figure 5-26: The scheme of the cosmic trigger setupused in the Gamma Irradiation Facility GIF++.

Because of the use of cosmic muons for this study, our trigger system configuration did not include any external scintillator-PM. The use of such an external system was not possible due to logistical reasons.

In order to evaluate the amount of fake triggers caused by accidental coincidences of gammas hitting the three indoor scintillators in the same time window of 10 ns, several checks were made.

First, the time window of one scintillator-PM was shifted outside the two others' coincidence time window. During the night 21:31:19 - 10:05:17 (system time), no trigger count was found with this configuration, indicating that the trigger setup has no fake triggers due to gammas coincidence. We also checked that no double counting triggers (due to a possible re-triggering problem of our Scintillator-PM system) were found by investigating the time separating two consecutive triggers.

Also, we compared the trigger counts for a low background rate and a high one. We did not find any significant difference in the trigger rate during the data taking with these two configurations (Fig. 5-27).

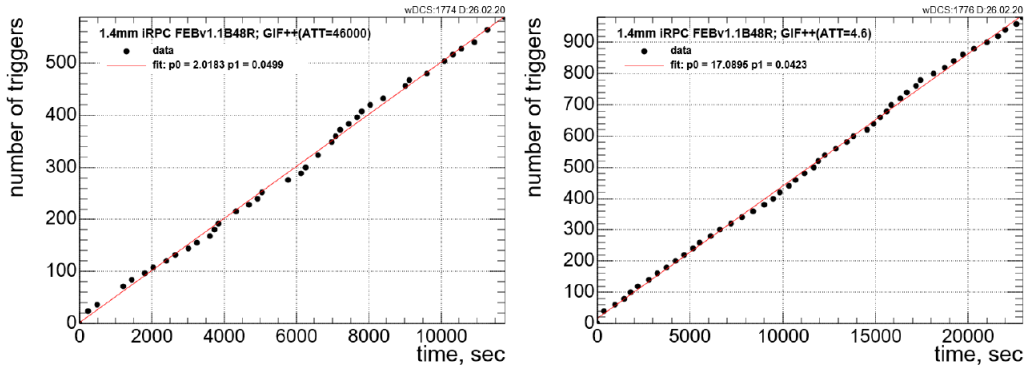

Figure 5-27: Left: Accumulated triggers number versus time exposure with low rate gamma background. Right: The same with a high rate gamma background.

Our trigger system was placed inside the GIF++ bunker and protected from the gamma source by lead bricks. In principle, the source was conceived to produce uniform irradiation in all the points of a plane. Therefore, we expect to have almost the same particle rate all over our chamber. However, the presence of the lead shield protecting the scintillators projects a shadow on the area where the scintillators detect the muons, resulting in different fluxes in the iRPC (Fig. 5-28). Although this setup does not allow us to study the response of our detector to high rate fluxes in the area covered by the triggers, it allows us to study the impact of the electronics dead time in the presence of a high flux on the iRPC efficiency (an average value of up to 2 kHz $\cdot$ cm^{-2}). Indeed, the electronics' dead time is sensitive to the average flux all over the iRPC, even if the detector efficiency is measured in the shielded region where the flux is about ten times lower.

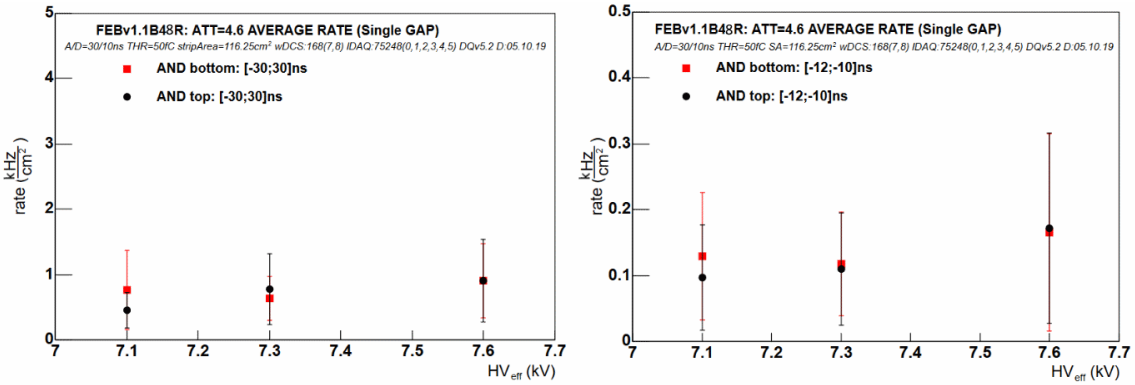

Figure 5-28: Rate Estimation for cosmic setup in GIF++ for the single gap study when signals received from both sides. Left: Estimation rate in the area outside scintillators. Right: Estimation rate in the area of the scintillator.

Figures (5-29, 5-30) show the measured iRPC efficiency with an average low irradiation and a high irradiation of about 2 kHz $\cdot$ cm^{-2} on our chamber versus the effective high voltage (HV_{eff}) on each of the two gaps. The efficiency of the iRPC with a signal detected on the HR side, the LR side, as well as on both of them is

shown for the two irradiation scenarios.

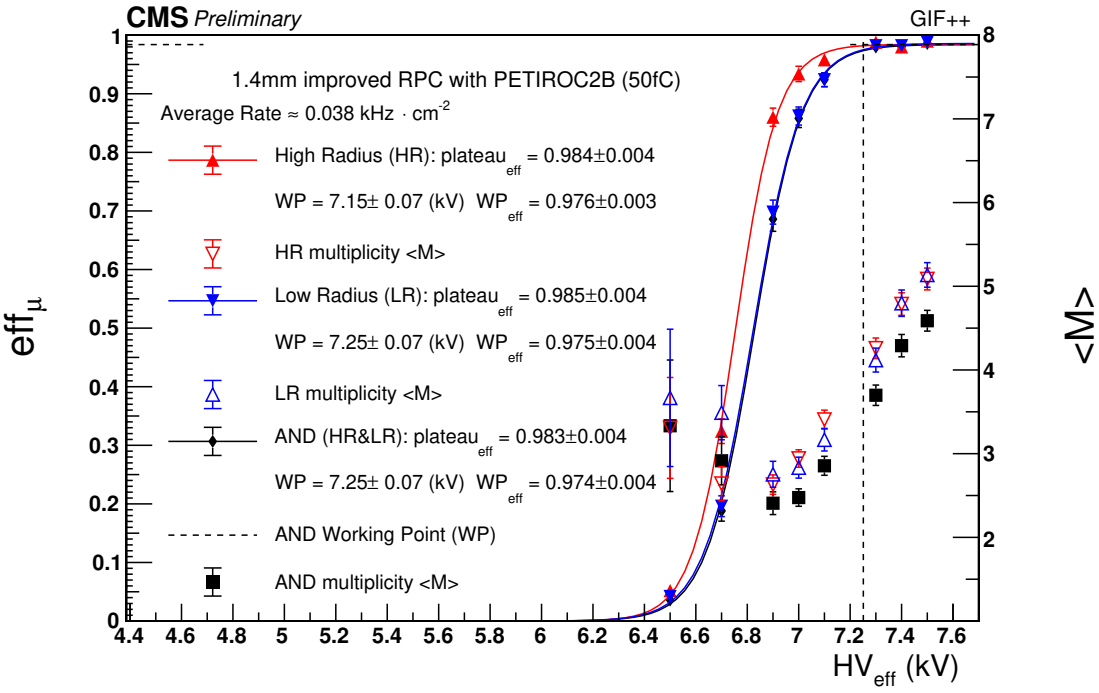

Figure 5-29: Efficiency versus the effective high voltage without the background rates. Also shown the average number of hits per event.

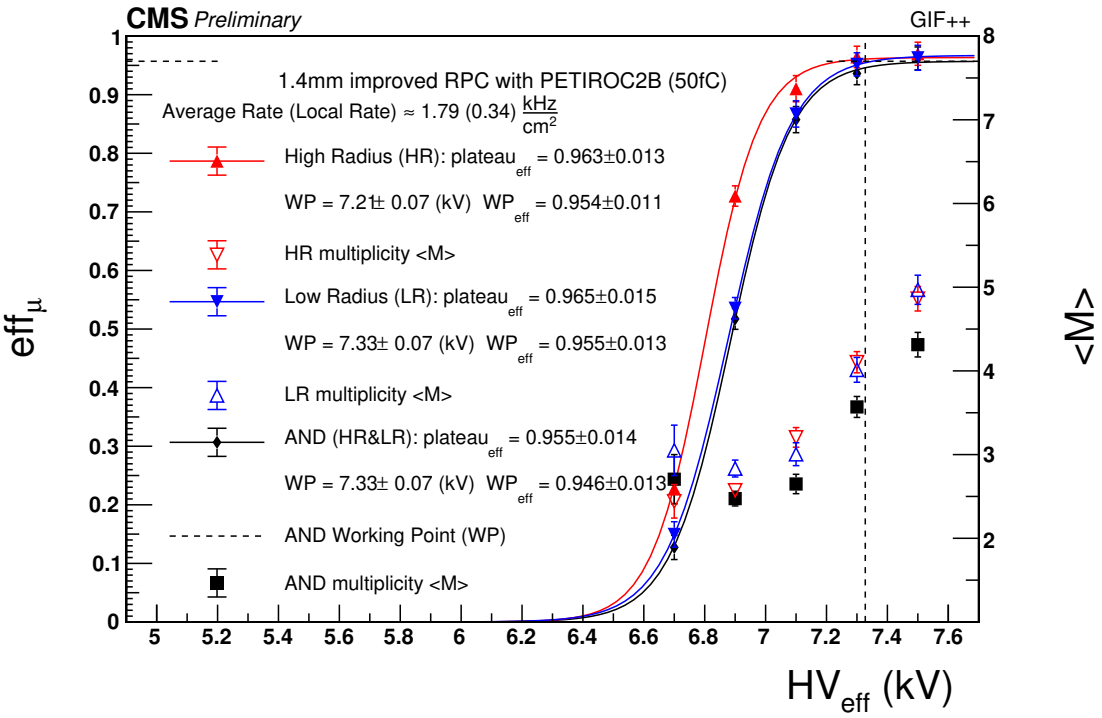

Figure 5-30: Efficiency versus the effective high voltage with a high background rate. Also shown the average number of hits per event.

It is important to note that the efficiency was measured in a position close to the chamber's high radius (HR) side. This corresponds to the worst situation due to the signal loss through propagation along the strip. In this case, the signal has to cross more than 3.6 m to reach the channels associated with the low radius (LR) side of the detector. This explains the relative difference between efficiencies that are observed for the high and low radius sides. This result was obtained with a PCB made of FR4 material. This effect is expected to be reduced with a new material (EM888), which is proposed to equip the future strips PCB.

The cluster size and multiplicity for the given HV points are also studied with high rate fluxes (See Ch. 4.5.2).

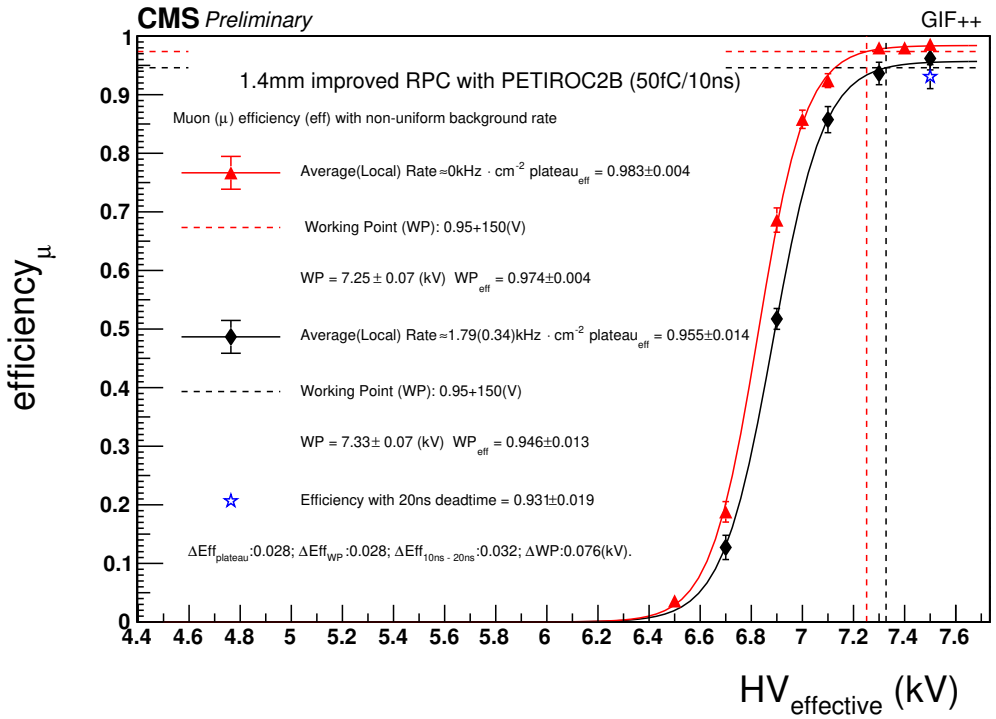

Figure 5-31: Study of the iRPC efficiency loss due to the FEB's dead time in presence of different gamma irradiation fluxes. Red is a low rate. Dark is a high rate.

Figure 5-31 shows a drop in efficiency at 1.8 kHz$\cdot$cm^{-2} of about 2.8% with respect to average low particle rate (0 Hz cm^{-2}) on our chamber. This drop in efficiency is related essentially to the electronics limitation caused by the dead time since the studied (shadowed) area of the detector is not impacted by the reduction due to the high rate flux.

As a cross-check, the efficiency was also measured using a dead time of 20 ns, which resulted in an additional 3% efficiency drop with respect to the one obtained at the same HV point with 10 ns. This confirms our expectations (See Ch. 4.3.1).

5.2.4 Threshold Scan

As already mentioned, the efficiency of reading out signals from the chamber's HR side is better than the opposite one due to the relatively reduced distance the signal needs to reach the first one. The signal of the LR side needs indeed to cross part of the strip and the return line. This effect manifests itself in the efficiency of the chamber and can be shown on the efficiency evaluation plot, where LR curve is shifted relatively to the HR one by 100 V (Fig. 5-31). In order to study the differences in signal amplitude on each end of the strip on the FR4-based PCB, a PETIROC threshold scan was performed with different HV_{eff} values (Fig. 5-33).

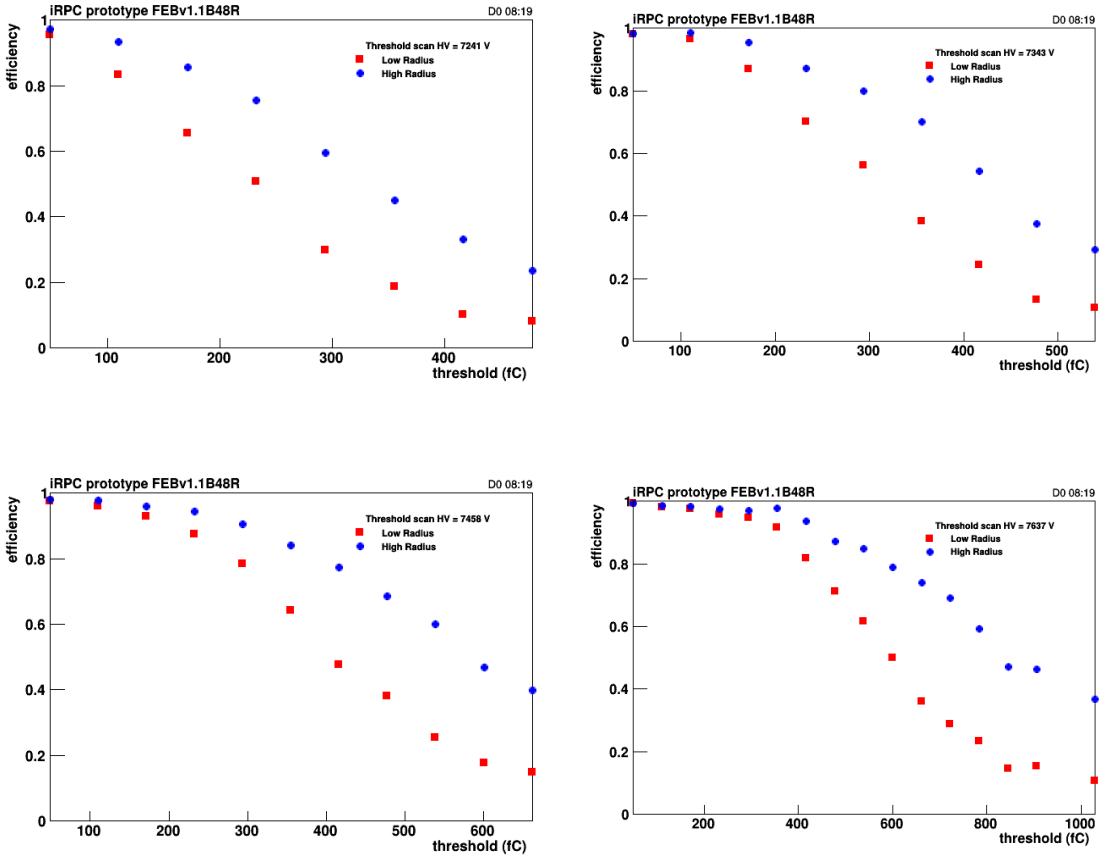

Figure 5-33: A threshold scan efficiency study for different HV values.

From this study, one can see that for a value of 7.3 kV and above, no difference of efficiency is observed between the two sides for a threshold of 100 fC.

For each HV scan, the value at which the efficiency is 50% of the maximum HR and that of the LR one is extracted. This result shows that the 50% efficiency is reached by the HR before, which indicates that, on average, this side sees more charge than the other one.

5.3 Study of the Detector Noise

The study of the combined detector and electronics noise is done by measuring the number of hits during a given time window outside the trigger window, normalized to the active area of the detector (Fig. 5-34).

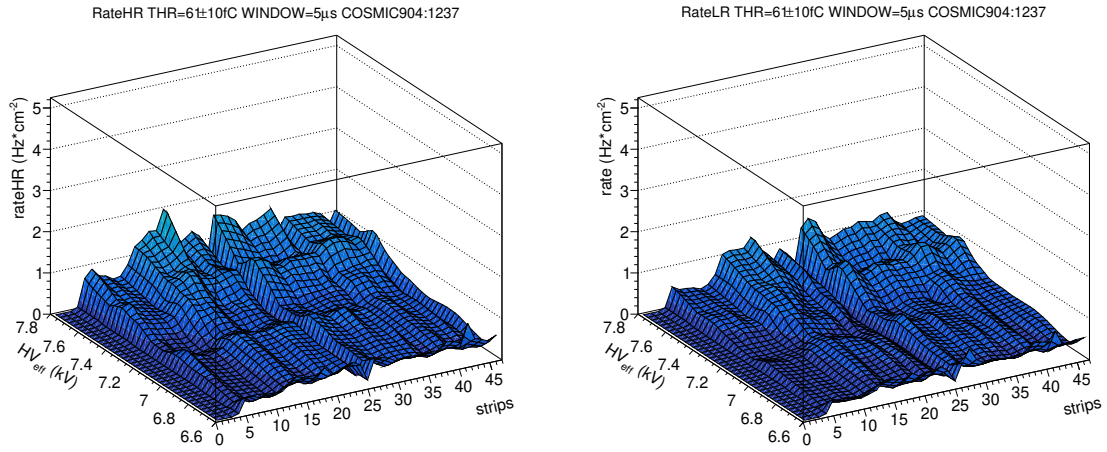

Figure 5-34: Left: Hit rate estimation from high radius for different HV_{eff} values. Right: Hit rate estimation from low radius for different HV_{eff} values.

In order to evaluate the detector noise only, we consider cases for which the two ends of at least one strip were fired (Fig. 5-35). These cases present most probably physical signals since electronics noise concerns channels that are not necessarily correlated with a given strip.

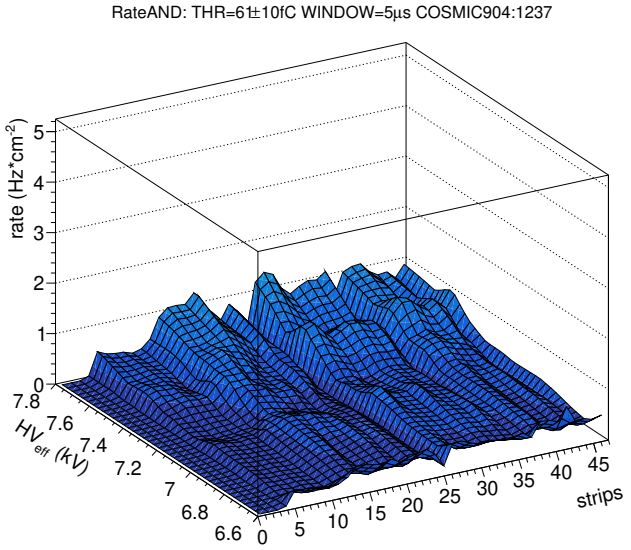

Figure 5-35: The hit rate of strips for different HV_{eff} values.

Concerning the electronics noise, it can be seen that in the range from 0 to 5 kV, where the detector is not effective (negligible avalanche gain), the electronics noise is less than ~ 0.5 Hz/cm^2 (Fig. 5-36).

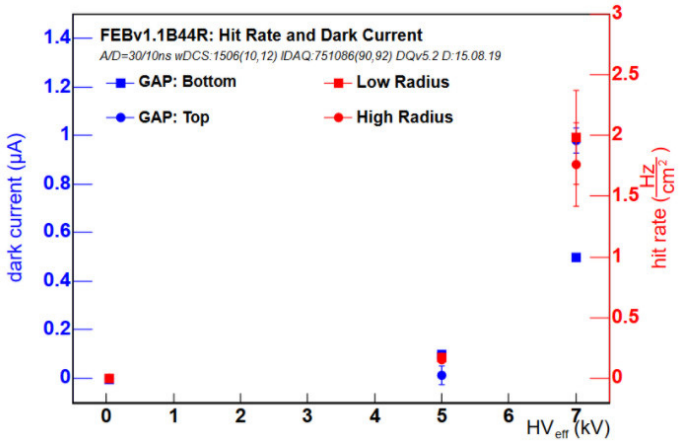

Figure 5-36: Estimated average hit rate of the studied chamber for different HV_{eff} values.

From these studies one can see that the noise contributions of both the detector and the electronics are rather small. The total noise, of less than 2 Hz/cm^2, is negligible with respect to the expected particle rate, which ensures that the detector will operate adequately under the future HL-LHC conditions.

5.4 Re-Triggering and X-Talk study of the readout system

In the analog part of the PETIROC, which includes a preamplifier, an analog-digital converter and a comparator, the re-triggering (Fig. 5-37) behavior of the PETIROC is observed when operated at low thresholds ($<$ 160 fC); to reduce this glitter, the ASIC must be set to operate in its latch mode. In this mode, when the signal produced by the passage of a charged particle crossing the RPC passes the threshold of the ASIC's channel connected to the closest of the two strip's ends, this channel's discriminator is neutralized for a period of 30 ns, but all others are left active. This period is the maximum time needed for the signal to reach the ASIC's channel that is connected to the other end of a fired strip at any point of this strip. After this period, all ASIC's channels are held on reset for a time interval whose length is chosen to allow the ASIC to be stabilized. For the different FEB prototypes developed so far, 10 ns was the lowest value that was possible to obtain. It is worth noting here that this reset time represents a dead time of the whole ASIC. The diagram explaining the different phases of the PETIROC acquisition during the data taking is illustrated in Figure 4-27.

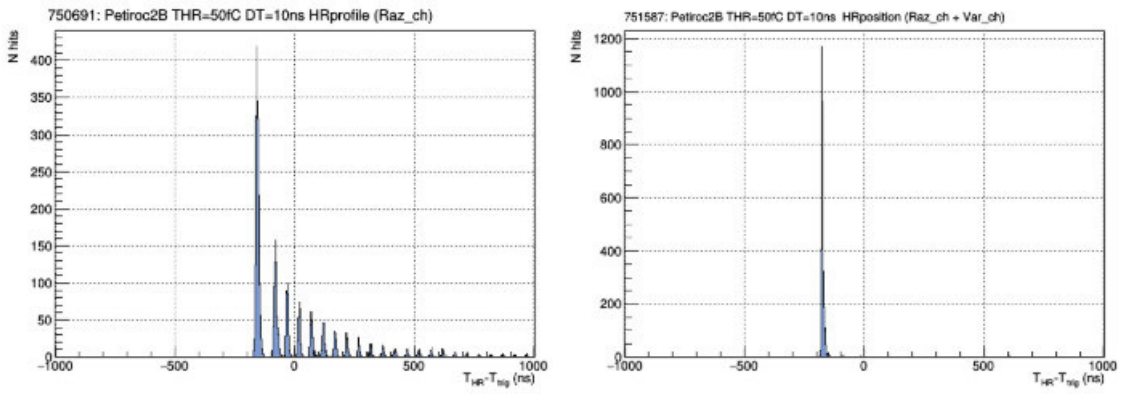

Figure 5-37: Example of re-triggering effect. Left: Data without correction of re-triggering at the given threshold. Right: Data with correction of re-triggering at the given threshold.

The X-talk is the triggering of several adjacent chip channels caused by a signal reaching only one or a few of them. Except for the TDC offset, the hits associated with this X-talk phenomenon are recorded at the same time (Fig. 5-38). They can be easily mitigated since they correspond to channels of two different sides fired at the same time. This simultaneous occurrence is indeed not possible for physical signals in the design of the PCB, where the FEB's connectors are placed on the large side of the PCB. In fact, the time difference of a signal detected on both ends of a strip induced by the passage of a particle is not compatible with zero.

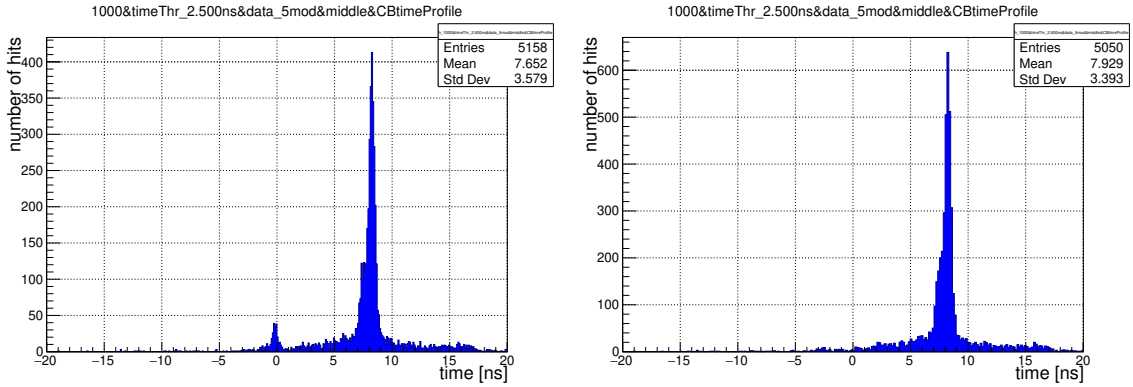

Figure 5-38: A, example of a time profile without (right) and with (left) X-talk effect of data sample with the background.

A study of X-talk events as a function of the threshold shows that the x-talk effect at $80 - 100$ fC becomes less than two percent (Fig. 5-39).

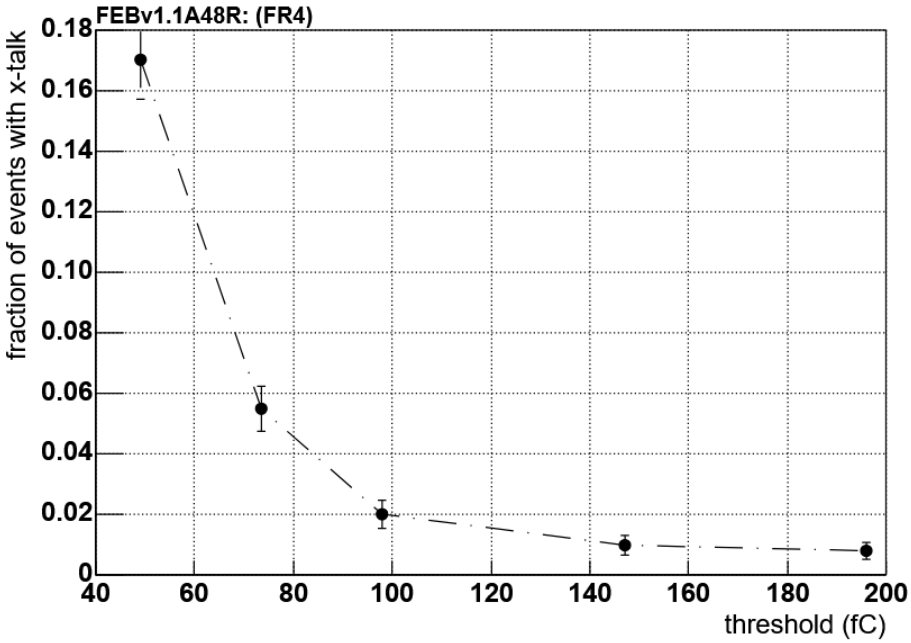

Figure 5-39: Study of x-talk effect vs threshold of PETIROC2A. The estimate of the number of events with x-talk. Line is given for a better view.

Following the observation of these problems related to operating the electronics at low thresholds, new versions of PETIROC, with an adapted bandwidth to reduce the chip's sensitivity, were proposed and later produced (See Ch. 4.3.1).

5.5 iRPC Time Resolution

In this section we try to characterize the fast timing response of our iRPC system. This is achieved by using a 1.4 mm gap detector and the PETIROC chip family. The iRPC resolution will be evaluated along the strip, which determines the accuracy of the hit position and the chamber's absolute time resolution.

5.5.1 Resolution Along the Strip

The measurements of the time characteristics of the chamber were carried out using muon beams provided by the SPS H2 beamline (Fig. 7-7). The chamber was mounted on a 100 micron-precision movable table to move the detector perpendicular to the beam. The scintillators-PM setup scheme is similar to a typical one (Fig. 5-2) using narrow scintillators.

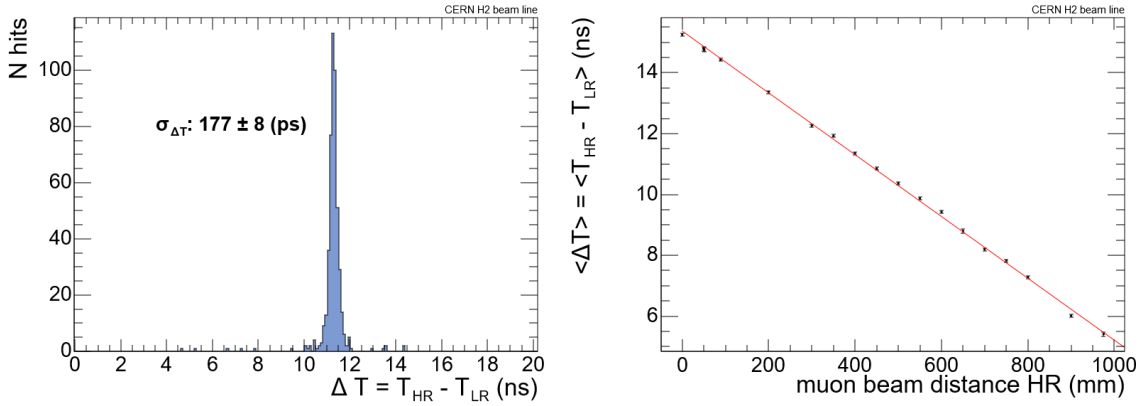

Figure 5-40: Left: Time resolution of the iRPC prototype at the center of the detector. Right: Correlation between the average ΔT measurement and the position of the beam with respect to a fixed reference.

Figure 5-40 (left) shows the observed resolution (177 ps) of the arrival time difference (ΔT) at the center of the detector. This excellent resolution allows the determination of the positions along the strip with a resolution of ≈ 1.7 cm. Figure 5-40 (right) shows the average position of the beam estimated from the arrival time difference as a function of the table position. The maximum deviation is found to be less than 2 cm with respect to the exact values.

5.5.2 iRPC Absolute Time Resolution

To estimate our detector's absolute time resolution, we measured the arrival time difference of the signals of two chambers crossed by the same particle in the same area of the two detectors (Fig. 5-41).

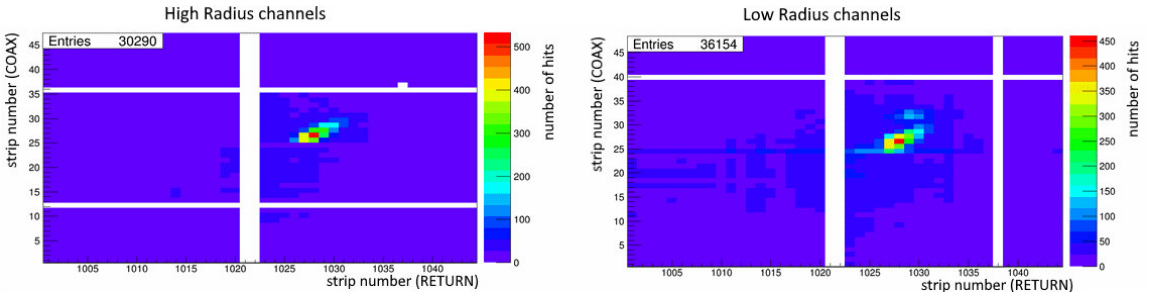

Figure 5-41: A scatter plot of the HR (left) and LR (right) strip end of the Coax chamber versus that of the Return chamber, fired by a muon.

The absolute time resolution is deduced by dividing the estimated resolution of this time difference by $\sqrt{2}$ with the assumption that both electronics are identical and uncorrelated.

$$\Delta t = ((T^{HR}_{prot.1} - T^{HR}_{prot.2}) + (T^{LR}_{prot.1} - T^{LR}_{prot.2}))/2 \tag{5.10}$$

$$\sigma_{t_1} - \sigma_{t_2} = \sigma_{\Delta t} \rightarrow \sigma^2_{\Delta t} = \sigma^2_{t_1} + \sigma^2_{t_2} - 2\sigma_{t_1}\sigma_{t_2}$$
$$< \sigma^2_{\Delta t} > = < \sigma^2_{t_1} > + < \sigma^2_{t_2} > -2 < \sigma_{t_1} * \sigma_{t_2} >$$
$$< \sigma^2_{\Delta t} > = < \sigma^2_{t_1} > + < \sigma^2_{t_2} > -2cov(\sigma_{t_1} * \sigma_{t_2})$$
$$< \sigma^2_{\Delta t} > = < \sigma^2_{t} > + < \sigma^2_{t} > \ if\ detectors\ are\ independent$$
$$< \sigma_t > = \frac{< \sigma_{\Delta t} >}{\sqrt{2}} \tag{5.11}$$

In this way, we can calculate the absolute resolution using two chambers (COAX and RETURN). This was done for two cases (See Ch. 4.5.1): in the first one, the time difference was determined after using the average value of the arrival time of the central strips determined using the "center" clustering method (Fig. 5-42), and in the second case the arrival time is the average of that of all the strips belonging to the cluster obtained with the "average" clustering method (Fig. 5-43). It can be shown that the "central" definition of time difference provides a resolution of the chamber of about 350 ps instead of 380 ps for the average definition.

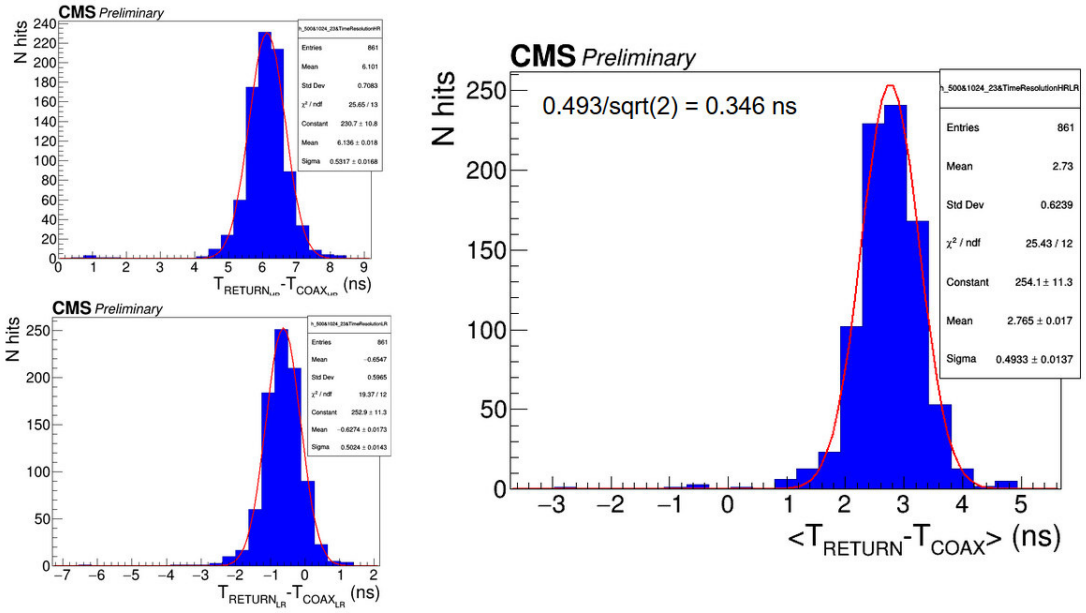

Figure 5-42: Time difference (Eq. 5.10) of two detectors for "center" definition. The RMS value divided by $\sqrt{2}$ provides the 2-gap HPL iRPC absolute time resolution.

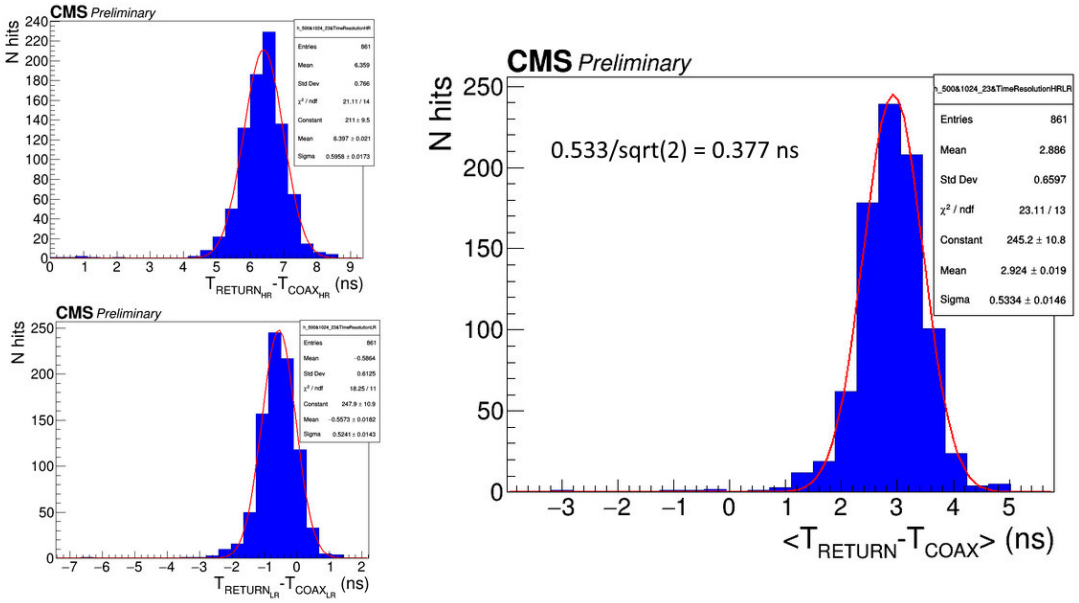

Figure 5-43: Time difference (Eq. 5.10) of the two detectors based on the "average" definition. The RMS value divided by $\sqrt{2}$ provides the 2-gap HPL iRPC absolute time resolution.

The result is shown in Figure 5-43. Thus, one can estimate that the absolute time resolution of each of these two large detectors is about 350 ps.

Chapter 6

iRPC for CMS

The LHC produces millions of proton-proton collisions every second. In order to select the events of interest for physics and discard the background, a trigger system is needed. In the case of CMS, this trigger system requires currently less than 4 μs to determine which events to keep and those to reject [75]. For HL-LHC, this decision time will be extended to 12.5μs to cope with the increased amount of information that will be added for the new trigger [2]. As it was mentioned before, the CMS trigger system is made of two stages: L1 and HLT (See Ch. 3.5). The L1 trigger was designed at the start of LHC, so that information from all detectors are processed separately, which made it difficult to provide useful combinations of the different sub-detectors for track reconstruction and momentum assignment.

The Muon CMS L1 trigger for RUN 2 has been upgraded in such a way that the decision to save the event is made by Muon Track Finders (Fig. 3-26) (MTF) when processing data from all different muon sub-detectors and their combinations. The Barrel Muon Track Finder (BMTF) covers the region of $|\eta| < 0.83$ and receives data from RPC and DT [112]. The Overlap Muon Track Finder (OMTF) receives data from the three sub-detectors in the η intermediate region $0.83 < |\eta| < 1.24$ [22]. The Endcap Muon Track Finder (EMTF) receives data from (i)RPC, CSC, GEM in the region of $|\eta| > 1.24$, comparing all track segments to identify muon patterns in this region and requiring at least two stations to declare a potential muon track.

The addition in the high eta region of of two stations of GEM and two of iRPC should improve EMTF and thus contribute to a better trigger performance in the HL-LHC phase. In the case of missing CSC information, iRPC hits will be very useful in providing the needed hits for tracks reconstruction. In addition, very good timing and position precision of iRPC will provide additional assets. For instance, they can be used to distinguish the hypothetical Heavy Scalar Charged Particle (HSCP) from muons.

6.1 Integration iRPC clustering algorithm

The overall collection of CMS software, referred to as CMSSW, is built around the Event Data Model (EDM) framework. EDM provides the needed tools to process the data and to perform simulations. The new clustering approach presented in the previous chapter needs thus to be integrated into CMSSW. One way to incorporate the processing of iRPC data is based on implementing the clustering algorithm in the same framework as the one of the current RPC clustering algorithm . This approach allows us to chose the adequate clustering algorithm in a straightforward way.

Processing of the iRPC data can be done using several classes (Fig. 6-1) that include the configuration one (iRPCInfo), the class of initialization of each hit (iRPCHit), the class dedicated to clusters (iRPCCluster) and finally the main code that contains the clustering algorithm (iRPCClustering).

The algorithm has been tested with simulated data of single muons. The optimization of the clustering parameters has then been achieved using these events.

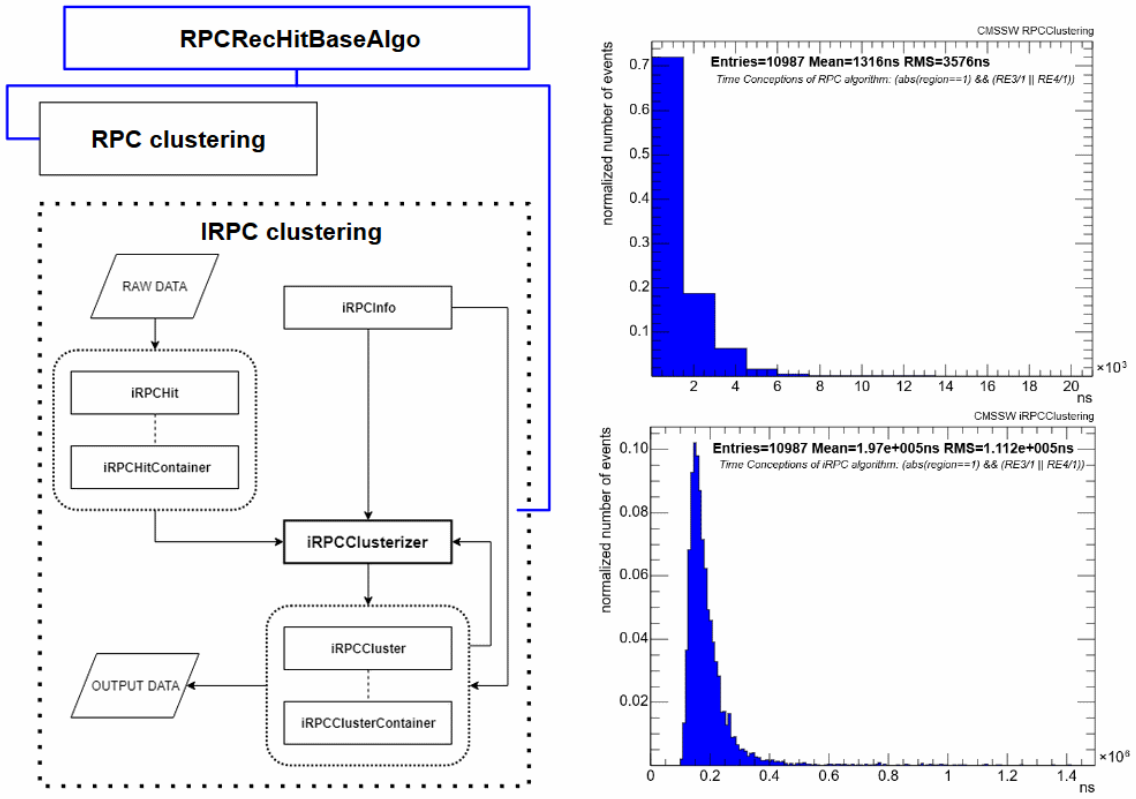

Figure 6-1: Structure of iRPC classes. The time consumption study. The top is RPC algorithm. The bottom is iRPC algorithm.

A comparison of iRPC and RPC's algorithms (Fig. 6-1) shows a considerable increase in time consumption of the new iRPC approach processing with respect to the current RPC version (about 100 times more) due to the time and η based clustering. Some additional steps are needed for the new method that includes the sorting of data and several loops over all of the event's hits. It is important to note that time consumption may be optimized after a detailed revision of the program's function. Optimization is possible because the algorithm that was tested in this study has generalized functions that can be replaced with high-speed counterparts.

One possible way to evaluate the new data clustering algorithm is to calculate and compare the residual[1] for iRPC using the current and the new one. This study's interest lies in that the new chamber has better resolution along the strips (Y) and it

[1]The residual is the distance between the reconstructed track of muon and the center of the cluster.

can also use this information to improve the x resolution since it allows the algorithm to separate clusters as the clusters 2, 3, 4 of the example shown in Figure 4-48.

The algorithms have been tested with simulated data of single muons without pileup. It can be specified that for the new clustering, it is necessary to set the adequate thresholds before processing data (Fig. 6-2).

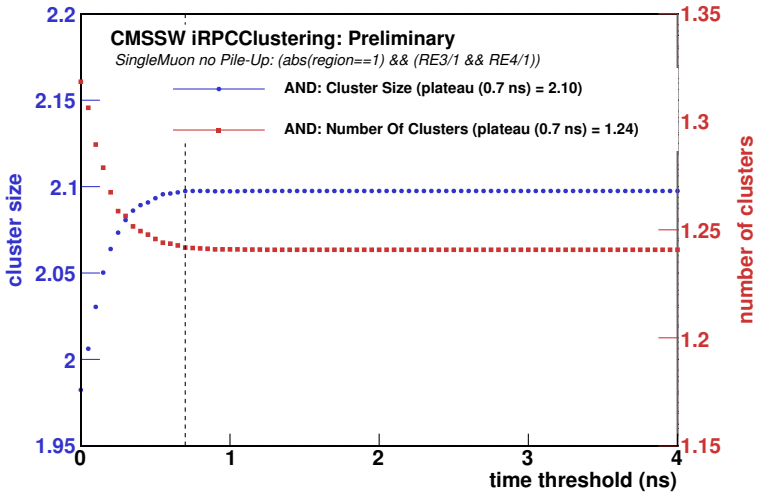

Figure 6-2: The study of threshold with simulation data for CMSSW.

If we select only events that give different results for the two clustering approaches, one with a strip clustering while the other is using the η position of the hits of each strip based on the time information of the two ends of each strip, we find that for about 1.7 % of the events the second algorithm performs better providing smaller residuals. In this case, the average value is almost the same, but the resolution is improved by a factor of 1.10 for x and 1.05 for y. Figure 6-3 shows the histograms for measured residuals for two different algorithms.

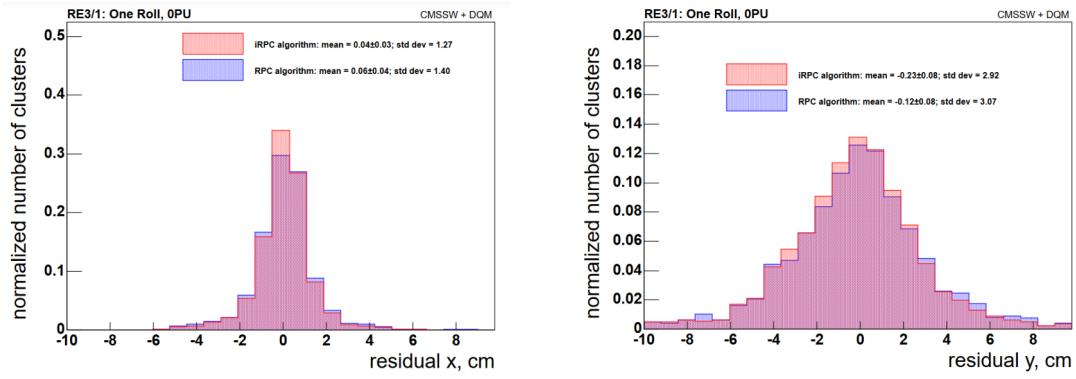

(a) (b)

Figure 6-3: The residual of x (a) and y (b) of the two algorithms (current and new) applied to events in the RE3/1 station.

To consider the impact of the clustering algorithm on data processing in the presence of pileup, we compare the two clustering algorithms mentioned above on similar simulated events[2]. In the case of the pileup study, the algorithm using the η information shows an improvement of the residuals distribution by a factor of 1.58 for x and 1.14 for y as shown in Figure 6-4. Thanks to a better exploitation of the position information, the new algorithm provides better performance in the presence of pileup by separating the contribution of different particles hitting neighbouring strips.

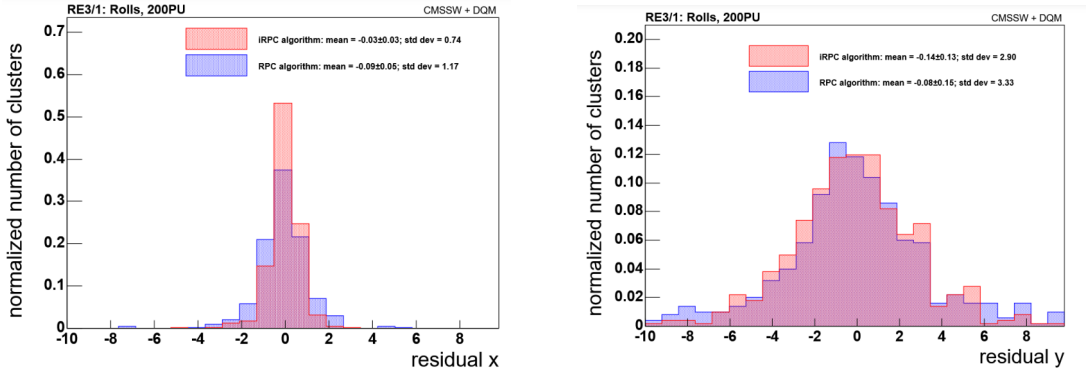

(a) (b)

Figure 6-4: The residual of x (a) and y (b) of the two algorithms (strips-based and the new η-based one) applied to events in the RE3/1 station with pileup.

[2]The comparison of the two algorithms in the case without pileup is done for the chamber with only one partition. The pileup study with one partition iRPC could not be made due to the absence of available simulated events. Only events simulated with iRPC readout segmented in five partitions can be used. The comparison of the algorithms for those two data sets will not affect significantly the residual estimation because hit position along the strip can still be accessed. However, in case of simulation with five partitions, less confusion is present if neighbouring strips are hit at different places within the clustering time thresholds.

6.2 Search of HSCP with iRPC

Several Standard Model extensions predict HSCPs. In some scenarios, they may have a lifetime greater than a few nanoseconds. The speed of these particles would be lower than the speed of light and their charge, Q, is not necessarily equal to the elementary charge $\pm$1e ([52], [57], [16]). These particles can be singly ($|Q| = 1e$), fractionally ($|Q| < 1e$), or multiply ($|Q| > 1e$) charged. They are long-lived in the sense that they will not decay inside the detector. When they go through the entire detector, they look like muons, which are the only known charged particles that penetrate the entire detector. A typical muon track is shown in Figure 6-5 in comparison with other kinds of particles, where one can see that muon passes through the detector.

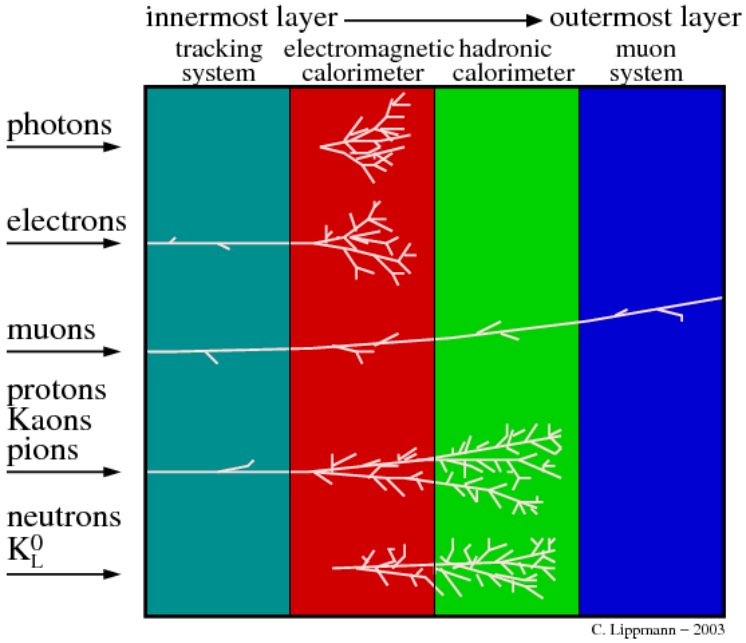

Figure 6-5: Components of a particle physics experiment produce in the detector. Each particle type has its signature in the detector [81].

In the minimal gauge mediated supersymmetry breaking (mGMSB) model, HSCPs behave like leptons. Stable heavy s-leptons may exist in some mGMSB scenarios. In the CMS detector, they are expected to form tracks similar to that of the muons, but with longer flight times before their decay. The mGMSB parameter, which corresponds to the useful supersymmetry breaking scale, is varied from 30 to 510 TeV which approximately leads to a range of staus mass between 100 and 1600 GeV.

A stable massive supersymmetric hadron (R-hadron) is predicted by Split-SUSY or SUGRA models. The R-hadron signal in the detector is similar to the s-lepton signal. The differences are multiple nuclear interactions of the R-hadron in the detector until it reaches the muon system.

One of the other possible theoretical scenarios with parity-like symmetries leads to the so-called magnetic monopoles. Some of them are expected to be non-neutral in such a way that they have electromagnetic and/or strong interactions with the

detectors along their trajectory with a small velocity. One of the simplest scenarios is a pair produced by staus.

The present mass limits of such candidates that are shown in Figure 6-6.

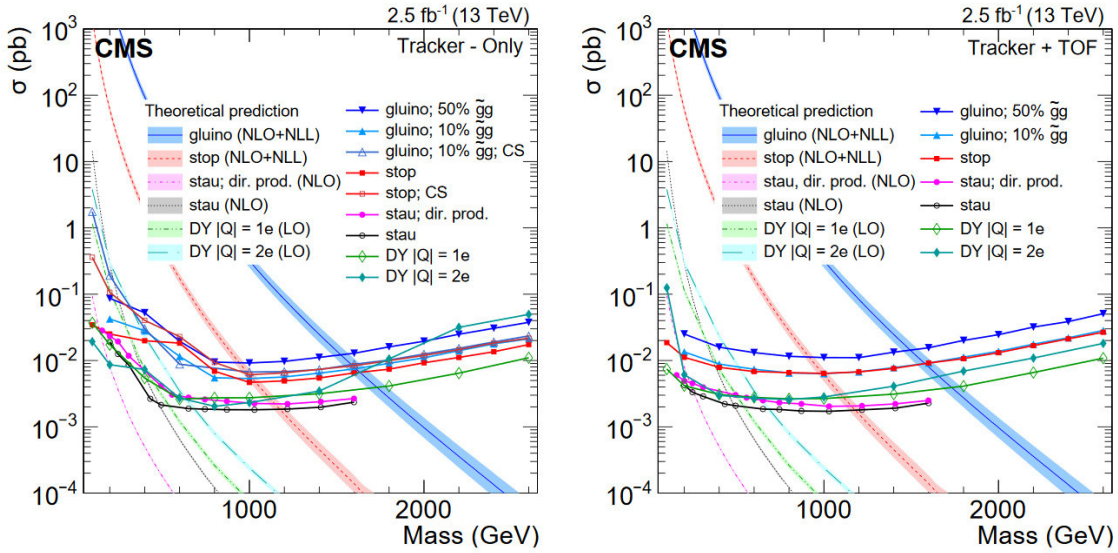

Figure 6-6: Results of the HSCP search as the cross section upper limits at 95% CL for various signal models for the tracker only analysis (left) and tracker TOF analysis (right) at $\sqrt{s} = 13$ TeV. In the legend, "CS" stands for charge suppressed interaction model [74].

So, heavy charged particles exist in different models. In the case of high velocity, such particles are inseparable from muons. At small velocity, they can be separated from muons if precise time information is provided. The CMS detector components are optimized to look for particles with velocities close to the velocity of light within the bunch crossing time window. Slow particle signals may be lost in the detector or attributed to another bunch crossing window.

The HSCP produced at LHC will have a relative velocity v < 1. It is possible, therefore, to distinguish light particles moving at speed close to the light speed from heavy particles thanks to Time Of Flight (TOF) detectors [74].

In the HL-LHC phase, both RPC and, more particularly, iRPC will provide better time resolution. This will improve the $\beta = (v/c)$ measurement, leading to better discrimination of HSCP against muons (Fig. 6-7).

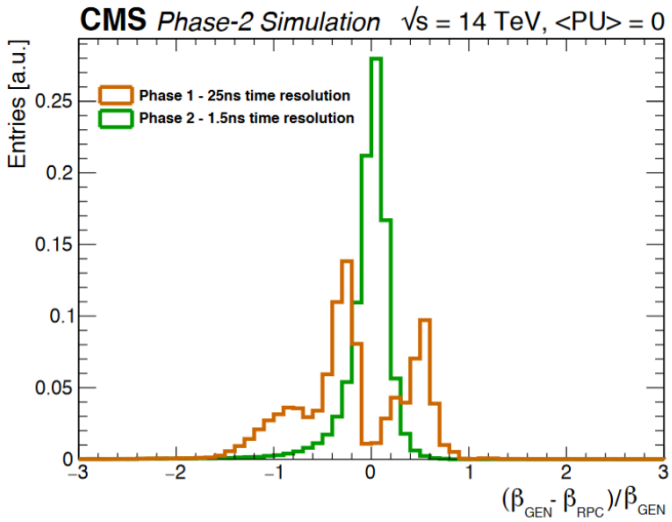

Figure 6-7: Resolution of the β measurement for L1 muon tracks using L1 trigger RPC hit [1].

HSCPs can be found as a slowly-moving muon-like within iRPC. A particle with mass m and momentum p has a velocity $v = c\beta$:

$$\beta = \frac{p}{\sqrt{p^2 + (mc)^2}} \tag{6.1}$$

where β is the coefficient of normalization. For a path length of L, the time T is given by:

$$T = \frac{L}{v} = \frac{L}{c\beta} = \frac{L}{c}(\sqrt{1 + (m/p)^2}) \tag{6.2}$$

If the momentum of the particle is much bigger than its rest mass ($p >> mc$) the can be written as follows, taking into account two first terms of Taylor series:

$$T = \frac{L}{c}(1 + \frac{1}{2}(m/p)^2) \tag{6.3}$$

The TOF can be used to distinguish HSCPs from muons with two iRPC stations. If the time of flight is precisely measured, the mass of particles can be identified. Thus, the difference in flight time of distance L between two particles with the same momentum and two different masses (m_1 and m_2) will be:

$$\Delta t = t_1 - t_2 = \frac{Lc}{2p^2}(m_1^2 - m_2^2) \tag{6.4}$$

In order to evaluate the performance of the TOF method for distinguishing two masses with iRPC resolution, we use the following formula to estimate the number of Standard Deviations (SD):

$$n_\sigma = (\frac{Lc}{2p^2})\frac{m_1^2 - m_2^2}{\sigma_t}, \tag{6.5}$$

where σ_t is the time resolution of the iRPC chamber.

Thus, it can be seen (Fig. 6-8) that for the entire range of the momentum, the iRPC resolution allows us to separate muons from possible HSCP candidates. Each curve gives a minimum mass of HSCP that could be distinguished from muon for a given resolution in terms of the number of SD (1,2,3, ... etc. sigmas).

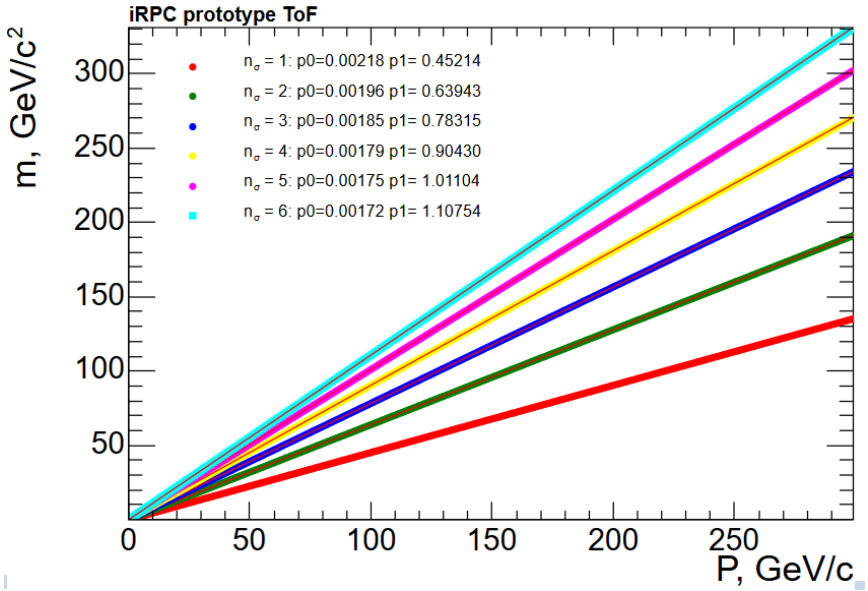

Figure 6-8: The resolution estimation of Time of Flight method for two station of iRPC. p_0, p_1 are parameters of the linear fit.

The resolution of more than three sigmas for high-p_t will allow the use of iRPC in track reconstruction of muons and HSCPs. This provides unique track search capabilities. A new data acquisition system could therefore be implemented to exploit the iRPC timing performance. The bew system could be implemented in EMTF.

Chapter 7

Conclusion

English

The LHC upgrade for high luminosity requires an upgrade of the CMS in many parts. One of the CMS upgrade tasks is to improve the muon tracking and trigger performance, particularly the installation of a new generation of RPC in the RE3/1 and RE4/1 stations. These areas, which were initially planned to be equipped from the beginning of the CMS construction, are still not used today because of the high flux of particles passing through them.

The accumulated experience with RPC has made it possible to achieve a chamber with the requested rate capability. This task required the use of new 1.2 mm Bakelite gaps to be produced in KODEL. In parallel, an innovative method of reading out the strips from both ends is proposed to better exploit the RPC capabilities. To achieve this, long strips with return lines read out from both ends independently using PETIROC ASIC are adopted.

Three prototypes were produced. The prototypes were tested in numerous tests using cosmic rays at CERN and CERN SPS beamlines (North Area). The high rate capability of the new chamber with high detection efficiency (>90%) was successfully demonstrated at CERN GIF++ facility. Based on these results, the proposed electronics readout system based on PETIROC and the single partition strips read out from both ends has been approved for CMS's upgrade project. In addition, an excellent absolute time resolution is obtained and is proposed to improve the search of HSCP particles that are predicted by several models beyond the Standard Model.

The possibility of integrating a new type of readout into the CMSSW is studied, and a new way of clustering is developed and tested. A new way to incorporate these stations into EMTF to improve the CMS trigger's efficiency is proposed. It is demonstrated that the prototypes can reach the required performance under the conditions of the RE3/1 and RE4/1 stations. Also, during the R&D the limitations of electronics were identified, and possible solutions were proposed that would increase the performance of electronics at high background loads. Improvements to the electronics are now planned. The minimum threshold will be lowered to 50 fC to ensure performance above 2 kHz without loss of efficiency due to the dead time effect. The latter is to be eliminated by making independent the reset of each of the PETIROC's channels.

As a result of this work, electronics based on PETIROC was approved to be used in the iRPC for CMS experiment.

French

La mise en jouvence du LHC pour la phase de la haute luminosité nécessite une mise à niveau du CMS en de nombreux points. L'une des tâches de la mise à niveau du CMS consiste à améliorer les performances des détecteurs de muons par l'installation, en particulier,d'une nouvelle génération de RPC dans les stations à haut η: RE3/1 et RE4/1. Ces zones, qui devaient initialement être équipées dès le début de la construction du CMS, ne sont toujours pas utilisées aujourd'hui en raison du flux important de particules qui les traversent.

L'expérience accumulée avec la RPC a permis de réaliser une chambre avec la capacité d'être opérée dans les flux de particules au moins trois fois supérieurs à ceux attendus. Cette tâche a nécessité l'utilisation de nouveux détecteurs utilisant des électrodes en Bakélite de 1.2 mm . Cesdétecteurs seront produits en Corée du Sud par le groupe KODEL. En parallèle, une méthode innovante de lecture électronique des détecteurs basée sur l'analyse des signaux des deux bouts des strips a été proposée. Pour y arriver, il a été suggéré d'utiliser de long strips avec des lignes de retour lues des deux cotés par une puce appelée PETIROC qui possède des performances temporelles remarquables.

Trois prototypes ont été produits. Les prototypes ont été testés lors de nombreux essais en utilisant les rayons cosmiques au CERN et des aisceaux de particules du SPS CERN (Zone Nord). Les capacités des noveaux détecteur à être opérés efficacement (>90) dans des flux élevés ont été démontrées dans l'installation GIF++ du CERN. Suit à ces résultats, l'électronique proposée, basée sur PETIROC et les strips lus des deux cotés, a été approuvée dans le cadre du projet de mise à niveau de CMS. De plus, une résolution remarquable du temps absolu a été obtenue avec les bouveux détecteurs. Cette performance sera extrêmement utile pour améliorer la recherche des particules hypothétques de type HSCP prédits dans plusieurs modèles au delà du Modèle Standard.

La possibilité d'intégrer un nouveau type de "readout" dans le CMSSW a été étudiée, et une nouvelle méthode de regroupement a été développée et testée. Une nouvelle méthode d'intégrer ces stations dans l'EMTF pour améliorer l'efficacité du déclenchement du CMS a été aussi proposée. Il a été démontré que les nouveaux détecteurs fonctionnent avec les performances requises dans les conditions des stations RE3/1 et RE4/1. En outre, au cours de la R&D, les limites de l'électronique ont été identifiées et des solutions possibles ont été proposées pour augmenter les performances de l'électronique en présence d'un taux de particules élevé. Des améliorations de l'électronique sont maintenant prévues. Le seuil minimal sera abaissé à 50 fC pour assurer des performances supérieures à 2 kHz/cm^2 sans perte d'efficacité due à l'effet de temps mort. Ce dernier sera drastiquement réduit en rendant la remise à zéro pour chaque canal indépendente des autres.

À la suite de ces travaux, l'électronique basée sur PETIROC a été approuvée pour être utilisée dans l'iRPC pour l'expérience CMS.

Acknowledgement

French

Ma participation dans ce projet n'aurait pas été possible sans mes directeurs de thèse Imad Laktineh et Maxime Gouzevitch. Je veux leur adresser toute ma gratitude pour leur aide et leur soutient, à la fois pour des démarches administratives mais avant tout pour l'ouverture à la science qu'ils m'ont offert.

Je souhaite remercier toute l'équipe du RPC IPNL avec laquelle j'ai travaillé, notamment Susana, Laurent, Christophe, François, Ece. Les échanges avec eux m'ont aidé chaque jour à progresser.

Ce travail n'aurait pas été possible sans Gabriella, Salvatore, Andre, Jan, Salvador, Nicolas, Cécilia qui ont participé, mais aussi aidé, dans l'innombrable quantité de tests réalisés au GIF++ et au 904 du CERN.

English

My project participation could not have been realized if it was not for my supervisors Imad Laktineh and Maxime Gouzevitch. I want to express my gratitude for the comprehensive assistance that I received, from the paperwork needed to prepare for my arrival in France to the project's daily routine and opened the door to science.

I would also like to thank all the staff of RPC IPNL with whom I worked in the person of Susana, Laurent, Christophe, Francois, Ece, for the example of professionalism and responsibility.

This work could not have been done without Gabriella, Salvatore, Andre, Jan, Salvador, Nicolas, Cécilia, who helped and participated in the organization of countless tests in GIF++ and 904 CERN.

Lyon's time would not have been so productive without the help of my wife Daria, who supported me throughout the time. It is also impossible to leave aside the moral support from family.

Appendixes

Table 7-1: Table with characteristics of prototypes.

Parameters/Name	FEBv0A44C	FEBv0A44R1	FEBv1A48R2	FEBv1B48R2
GAP Material	Bakelite			
Number of GAPs	2			
GAP Thickness	1.4 mm			
HPL Thickness	1.4 mm			
PCB	v.1 (Coaxial)	v.2 (Return)	v.3 (Return)	v.3 (Return)
Dimension (mm)	1645/570/315	1700/586/325	1700/586/325	1559/518/243
Strip Pitch (mm)	10-5			
Number of strips	48	48	48	48
Position of plug	Side	Side	Middle	Middle
PCB Material	FR4	FR4	FR4	FR4
FEB	Prototype (v.0)	Prototype (v.1)	Prototype (v.1)	Prototype (v.1)
PETIROC	2A	2A	2A	2B (Only FEB)
Threshold	‘100 fC	80 fC	100 fC	50 fC
Efficiency (2kHz)	0.99 (0.95)	0.99 (0.96)	0.98	0.98 (0.96)
WP (2kHz)	7.311 (7.464) kV	7.277 (7.442) kV	7.380 kV	7250 (7330) kV
Noise	$<$3.5 Hz/cm^2	$<$3 Hz/cm^2	$<$2 Hz/cm^2	$<$2 Hz/cm^2
Time Resolution	177+-8 (ps)			
Absolute Rime Resolution	377+-17 (ps)			

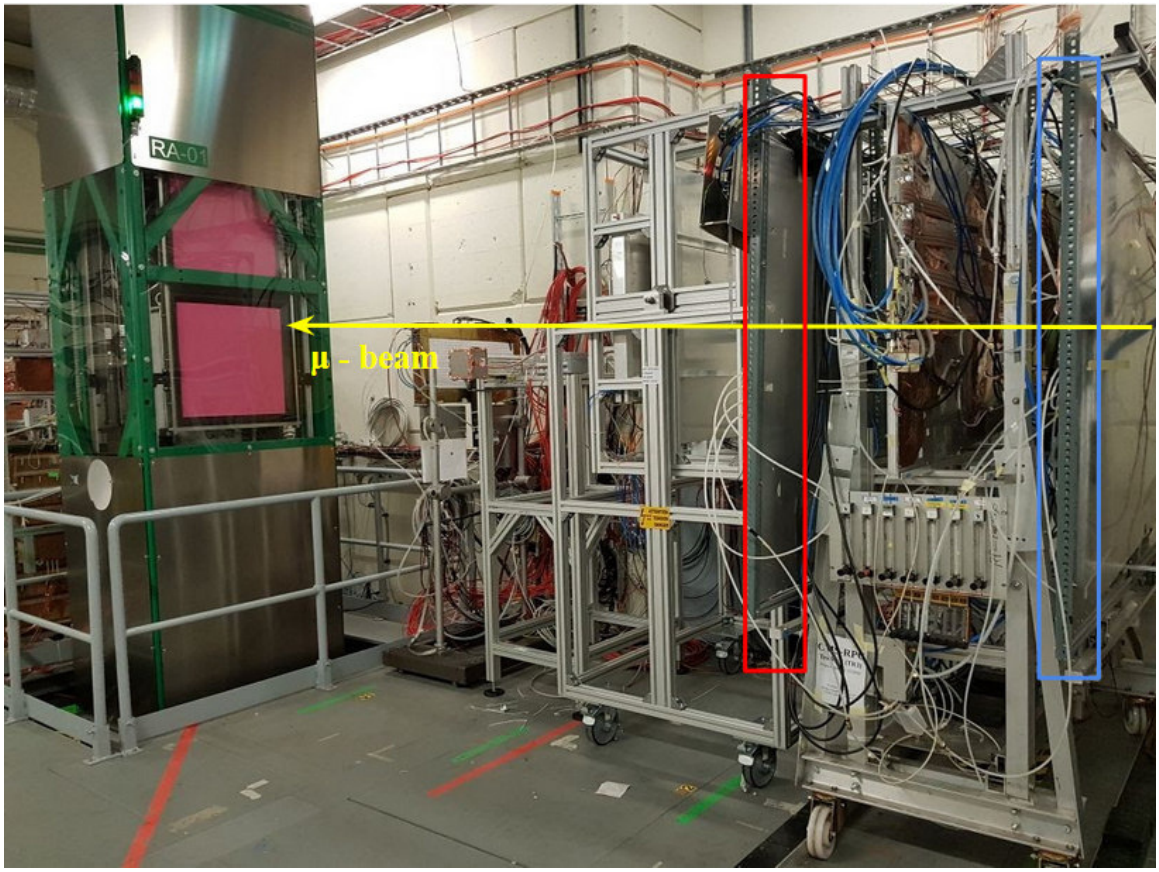

Figure 7-2: Photo of GIF setup from 2018.

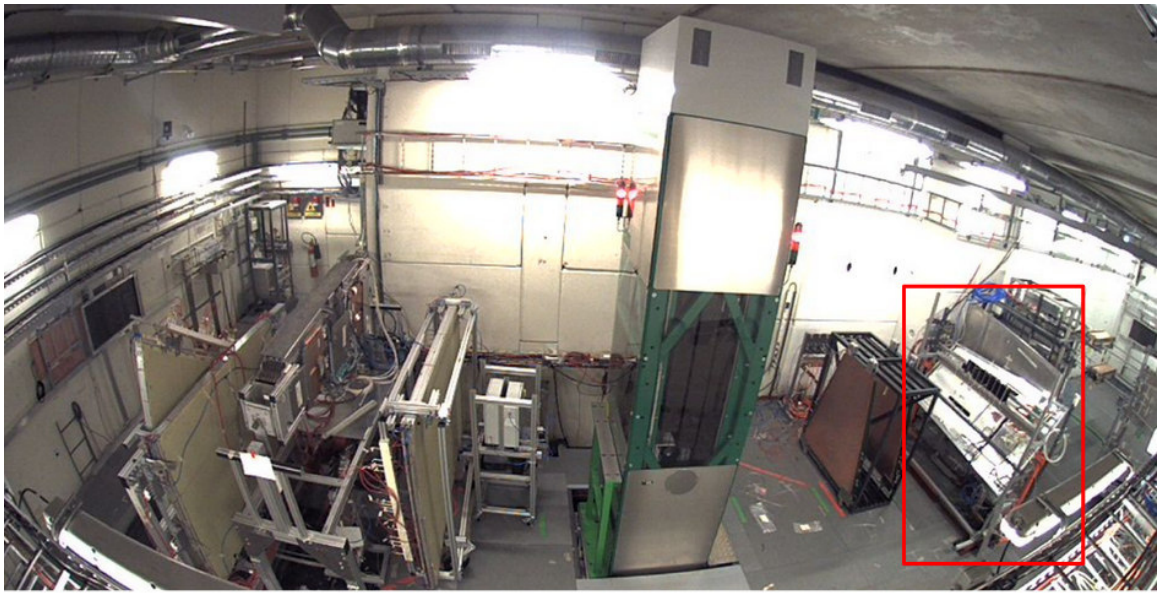

Figure 7-3: Photo of GIF setup from 2019.

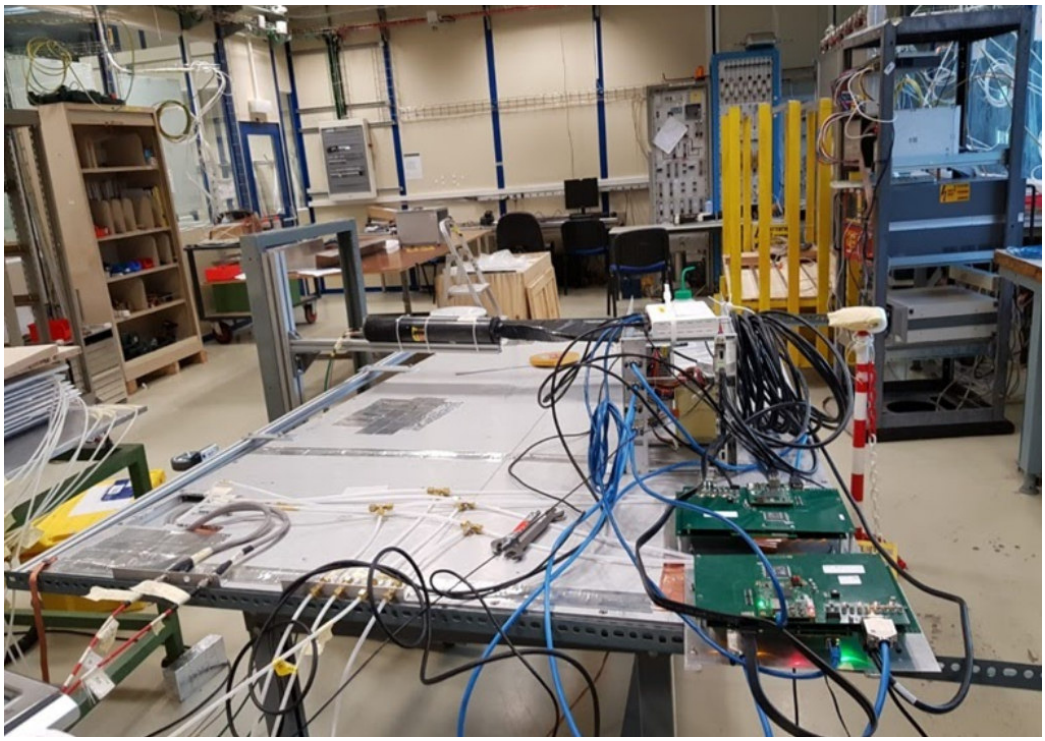

Figure 7-4: Photo of cosmic setup.

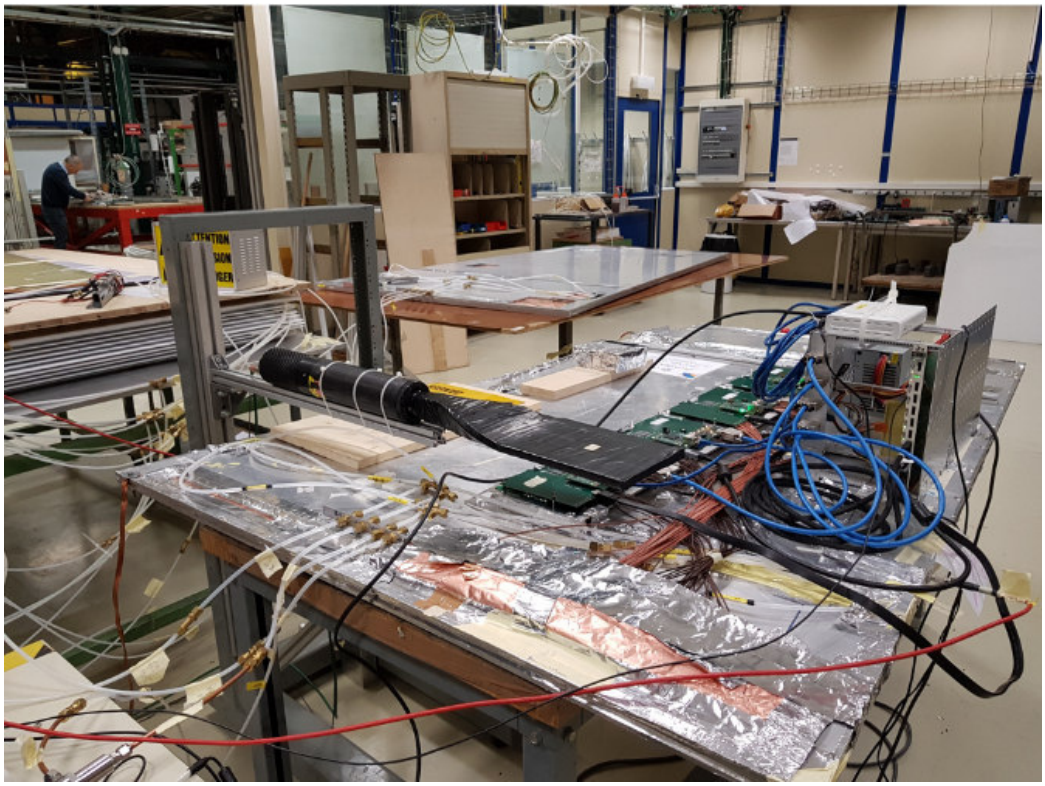

Figure 7-5: Photo of cosmic setup.

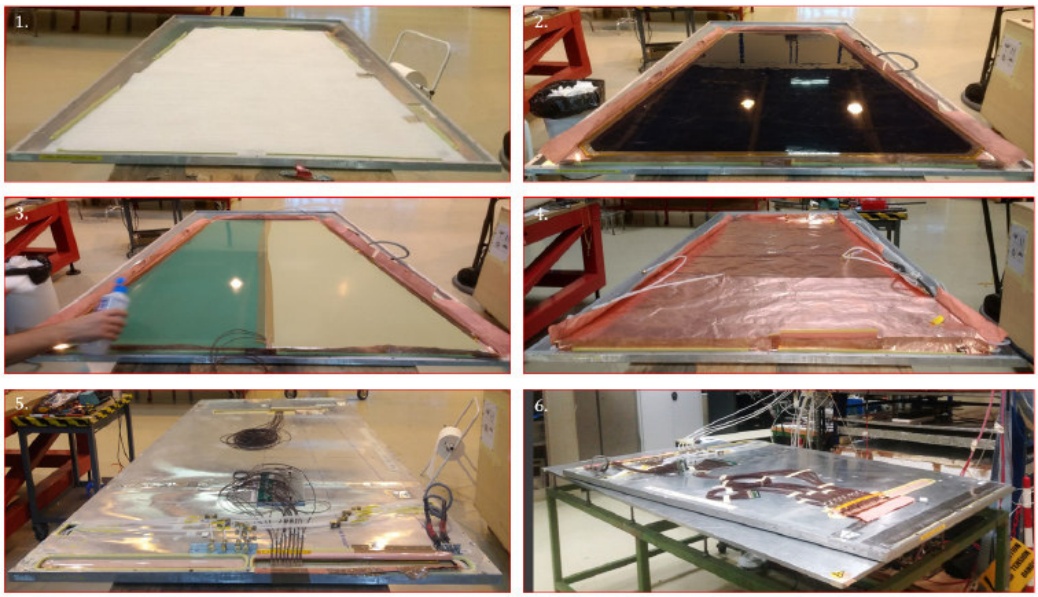

Figure 7-6: Photos of several steps assembly of the chamber.

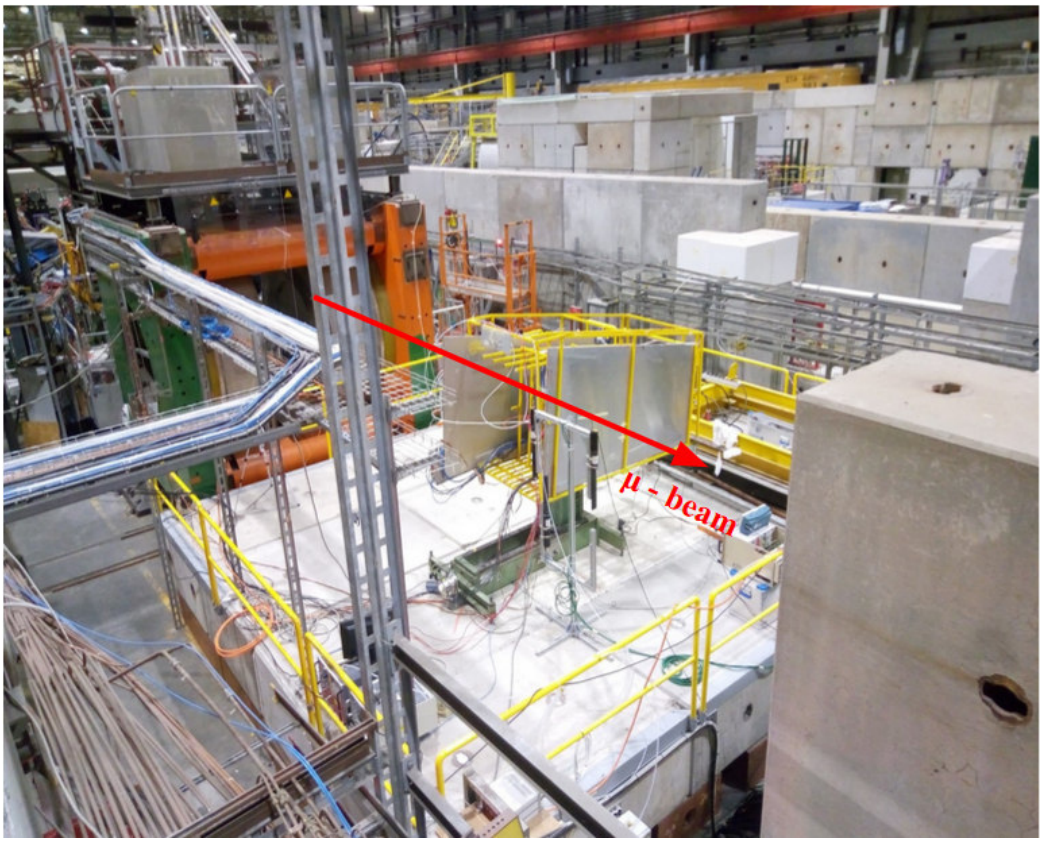

Figure 7-7: Photo of setup in H2 line SPS.

List of Figures and Tables

Bibliography

[1] The Phase-2 Upgrade of the CMS L1 Trigger Interim Technical Design Report. Technical Report CERN-LHCC-2017-013. CMS-TDR-017, CERN, Geneva, Sep 2017. This is the CMS Interim TDR devoted to the upgrade of the CMS L1 trigger in view of the HL-LHC running, as approved by the LHCC.

[2] The Phase-2 Upgrade of the CMS Level-1 Trigger. Technical Report CERN-LHCC-2020-004. CMS-TDR-021, CERN, Geneva, Apr 2020. Final version.

[3] Ijaz A. et al. Quality assurance tests of the cms endcap rpcs. *CERN-CMS-NOTE-2008-030*, 07 2013.

[4] G. Aad et al. The ATLAS Experiment at the CERN Large Hadron Collider. *JINST*, 3:S08003, 2008.

[5] G. Aad et al. Observation of a new particle in the search for the Standard Model Higgs boson with the ATLAS detector at the LHC. *Phys. Lett. B*, 716:1–29, 2012.

[6] K. Aamodt et al. The ALICE experiment at the CERN LHC. *JINST*, 3:S08002, 2008.

[7] W. Adam et al. The CMS high level trigger. *Eur. Phys. J. C*, 46:605–667, 2006.

[8] S. Agostinelli et al. Geant4—a simulation toolkit. *Nuclear Instruments and Methods in Physics Research Section A: Accelerators, Spectrometers, Detectors and Associated Equipment*, 506(3):250 – 303, 2003.

[9] Reyes Alemany-Fernández et al. Performance of the CERN Injector Complex and Transmission Studies into the LHC during the Second Proton-Lead Run. In *8th International Particle Accelerator Conference*, page TUPVA128, 2017.

[10] Jr. Alves, A.Augusto et al. The LHCb Detector at the LHC. *JINST*, 3:S08005, 2008.

[11] I. Antcheva et al. Root — a c++ framework for petabyte data storage, statistical analysis and visualization. *Computer Physics Communications*, 180(12):2499 – 2512, 2009. 40 YEARS OF CPC: A celebratory issue focused on quality software for high performance, grid and novel computing architectures.

[12] P. Azzi et al. Standard model physics at the hl-lhc and he-lhc, 2019.

[13] Paolo Azzurri. The CMS silicon strip tracker. *Journal of Physics: Conference Series*, 41:127–134, may 2006.

[14] David Barney and Sergio Cittolin. CMS Detector Drawings. *CERN*, Jan 2000.

[15] Giuseppe Battistoni et al. The fluka code: An accurate simulation tool for particle therapy. *Frontiers in Oncology*, 6, 05 2016.

[16] Christian W. Bauer, Zoltan Ligeti, Martin Schmaltz, Jesse Thaler, and Devin G.E. Walker. Supermodels for early lhc. *Physics Letters B*, 690(3):280–288, Jun 2010.

[17] Federico Betti. Observation of CP violation in charm decays at LHCb. In *54th Rencontres de Moriond on Electroweak Interactions and Unified Theories*, 5 2019.

[18] C. Binetti et al. A new front-end board for rpc detector of cms. *CMS-NOTE-1999-047, CERN-CMS-NOTE-1999-047*, 09 1999.

[19] Blomer et al. Evolution of the ROOT Tree I/O. *FERMILAB-CONF-20-165-SCD*, 3 2020.

[20] Oliver S. Bruning and Paul Collier. Building a behemoth. *Nature*, 448:285–289, 2007.

[21] Oliver Sim Brüning, Paul Collier, P Lebrun, Stephen Myers, Ranko Ostojic, John Poole, and Paul Proudlock. *LHC Design Report*. CERN Yellow Reports: Monographs. CERN, Geneva, 2004.

[22] Karol Bunkowski. The algorithm of the CMS Level-1 Overlap Muon Track Finder trigger. Technical Report CMS-CR-2018-073, CERN, Geneva, Jun 2018.

[23] Martin J. VanDer Burgt. Coaxial Cables and Applications. Technical report, Belden Electronics Division, SeniorProduct Engineering Project Manager, 2003.

[24] R Cardarelli, V Makeev, and R Santonico. Avalanche and streamer mode operation of resistive plate chambers. *Nuclear Instruments and Methods in Physics Research Section A: Accelerators, Spectrometers, Detectors and Associated Equipment*, 382(3):470 – 474, 1996.

[25] Jean-Luc Caron. The LHC injection complex.. L'ensemble d'injection du LHC. AC Collection. Legacy of AC. Pictures from 1992 to 2002., May 1993.

[26] CERN. *The CMS magnet project: Technical Design Report*. Technical Design Report CMS. CERN, Geneva, 1997.

[27] CERN. Geneva. LHC Experiments Committee. The CMS tracker system project: Technical Design Report. Technical report, CERN, 1997.

[28] Chatrchyan and CMS Collaboration. Identification and filtering of uncharacteristic noise in the cms hadron calorimeter. *Journal of Instrumentation*, 5:T03014, 03 2010.

[29] S. Chatrchyan et al. The CMS Experiment at the CERN LHC. *JINST*, 3:S08004, 2008.

[30] S. Chatrchyan and etc. Observation of a new boson at a mass of 125 gev with the cms experiment at the lhc. *Physics Letters B*, 716(1):30 – 61, 2012.

[31] Sergey Chatrchyan et al. Precise mapping of the magnetic field in the cms barrel yoke using cosmic rays. *Journal of Instrumentation*, 5:T03021, 03 2010.

[32] Xiushan Chen, C. Combaret, C. Girerd, C. Guerin, I. Laktineh, X. Lin-Ma, L. Mirabito, and G-N Lu. Multi-channel time-tagging module for fast-timing Resistive Plate Chamber detectors. *PoS*, TWEPP2019:093, 2020.

[33] Xiushan Chen, Xueying Lin-Ma, Christophe Combaret, Laurent Mirabito, Guo-Neng Lu, and Imad Laktineh. Improved Tapped-Delay-Line Time-to-Digital Converter with Time-over-Threshold measurement for a new generation of Resistive Plate Chamber detectors. *PoS*, TWEPP2018:141, 2019.

[34] D.J.A. Cockerill. The CMS Electromagnetic Calorimeter at the LHC. In *34th International Conference on High Energy Physics*, 10 2008.

[35] ATLAS Collaboration. Technical Design Report for the ATLAS Inner Tracker Pixel Detector. Technical Report CERN-LHCC-2017-021. ATLAS-TDR-030, CERN, Geneva, Sep 2017.

[36] CMS Collaboration. Performance of the cms cathode strip chambers with cosmic rays. *Journal of Instrumentation*, 5(03):T03018–T03018, Mar 2010.

[37] CMS Collaboration. Performance of the cms drift tube chambers with cosmic rays. *Journal of Instrumentation*, 5(03):T03015–T03015, Mar 2010.

[38] CMS Collaboration. Performance study of the CMS barrel resistive plate chambers with cosmic rays. *Journal of Instrumentation*, 5(03):T03017–T03017, mar 2010.

[39] CMS Collaboration. The Phase-2 Upgrade of the CMS Barrel Calorimeters. Technical Report CERN-LHCC-2017-011. CMS-TDR-015, CERN, Geneva, Sep 2017. This is the final version, approved by the LHCC.

[40] CMS Collaboration. The Phase-2 Upgrade of the CMS Endcap Calorimeter. Technical Report CERN-LHCC-2017-023. CMS-TDR-019, CERN, Geneva, Nov 2017. Technical Design Report of the endcap calorimeter for the Phase-2 upgrade of the CMS experiment, in view of the HL-LHC run.

[41] CMS Collaboration. The Phase-2 Upgrade of the CMS Muon Detectors. Technical Report CERN-LHCC-2017-012. CMS-TDR-016, CERN, Geneva, Sep 2017. This is the final version, approved by the LHCC.

[42] CMS Collaboration. The Phase-2 Upgrade of the CMS Tracker. Technical Report CERN-LHCC-2017-009. CMS-TDR-014, CERN, Geneva, Jun 2017.

[43] CMS Collaboration and Thomas Mc Cauley. Collisions recorded by the CMS detector on 14 Oct 2016 during the high pile-up fill. CMS Collection., Nov 2016.

[44] Et Collaboration, Krzysztof Pozniak, Ryszard Romaniuk, and Wojciech Zabolotny. Calibration of the cms drift tube chambers and measurement of the drift velocity with cosmic rays. *Journal of Instrumentation*, 5:1–39, 03 2009.

[45] The CMS collaboration. Alignment of the CMS tracker with LHC and cosmic ray data. *Journal of Instrumentation*, 9(06):P06009–P06009, jun 2014.

[46] Collaborations et al. Design, performance, and calibration of the cms hadron-outer calorimeter cms hcal. 2008.

[47] D Contardo, M Klute, J Mans, L Silvestris, and J Butler. Technical Proposal for the Phase-II Upgrade of the CMS Detector. Technical Report CERN-LHCC-2015-010. LHCC-P-008. CMS-TDR-15-02, CERN, Geneva, Jun 2015.

[48] T. Dai, Liangxiu Han, S. Hou, M. Liu, Q. Li, H. Song, L. Xia, and Z. Zhang. Low resistance bakelite rpc study for high rate working capability. *Journal of Instrumentation*, 9:C11013–C11013, 11 2014.

[49] D. Denegri. Standard model physics at the LHC (*pp* collisions). *Conf. Proc. C*, 901004:56–117, 1990.

[50] P. A. M. Dirac. The theory of magnetic poles. *Phys. Rev.*, 74:817–830, Oct 1948.

[51] Dominguez et al. CMS Technical Design Report for the Pixel Detector Upgrade. Technical Report CERN-LHCC-2012-016. CMS-TDR-11, CERN, Sep 2012.

[52] M. Drees and X. Tata. Signals for heavy exotics at hadron colliders and super-colliders. *Physics Letters B*, 252(4):695 – 702, 1990.

[53] L. Ducimetiere, Noel Garrel, Michael Barnes, and Gary Wait. The lhc injection kicker magnet. volume 2, pages 1162 – 1164 Vol.2, 06 2003.

[54] Ltd. Elite Material Co. High tg / low loss / halogen free em-888 / em-888b. Technical report, Elite Material Co., Ltd., Nov. 2017.

[55] G. Abbiendi et al. The cms muon barrel drift tubes system commissioning. *Nuclear Instruments and Methods in Physics Research Section A: Accelerators, Spectrometers, Detectors and Associated Equipment*, 598(1):192 – 195, 2009. Instrumentation for Collding Beam Physics.

[56] Julien Fleury et al. Petiroc a new front-end asic for time of flight application. *2013 IEEE Nuclear Science Symposium and Medical Imaging Conference (2013 NSS/MIC)*, pages 1–5, 2013.

[57] M. Fairbairn, A.C. Kraan, D.A. Milstead, T. Sjöstrand, P. Skands, and T. Sloan. Stable massive particles at colliders. *Physics Reports*, 438(1):1–63, Jan 2007.

[58] Apollinari G. et al. High Luminosity Large Hadron Collider HL-LHC. *CERN Yellow Rep.*, pages 1–19, 2015.

[59] R. Ganai, K. Agarwal, A. Roy, B. Muduli, S. Chattopadhyay, Z. Ahammed, G. Das, and S. Ramnarayan. Study of Performance of Bakelite Resistive Pate Chamber (RPC). *Springer Proc. Phys.*, 174:547–551, 2016.

[60] G.F. Giudice and R. Rattazzi. Theories with gauge mediated supersymmetry breaking. *Phys. Rept.*, 322:419–499, 1999.

[61] G.F. Giudice and A. Romanino. Erratum to: "split supersymmetry" [nucl. phys. b 699 (2004) 65]. *Nuclear Physics B*, 706(1-2):487, Jan 2005.

[62] Junghwan Goh. CMS RPC efficiency measurement using the tag-and-probe method. Technical Report CMS-CR-2018-131, CERN, Geneva, Jul 2018.

[63] Jeff Greensite. *An Introduction to the confinement problem*. Springer, Heidelberg New York, 2011.

[64] David Griffiths. Introduction to elementary particles. *Introduction to Elementary Particles by David Griffiths. Wiley, 2008. ISBN: 978-3-527-40601-2*, 01 2008.

[65] R. Guida. Gif++: The new cern irradiation facility to test large-area detectors for hl-lhc. In *2015 IEEE Nuclear Science Symposium and Medical Imaging Conference (NSS/MIC)*, pages 1–4, 2015.

[66] R. Hadjiiska et al. Cms rpc background – studies and measurements, 2020.

[67] Patricia Hansen, Per Carlson, Emiliano Mocchiutti, S. Sciutto, and M. Boezio. Flux of atmospheric muons: Comparison between aires simulations and caprice98 data. *Physical review D: Particles and fields*, 68, 07 2003.

[68] J. Hauser et al. Experience with trigger electronics for the csc system of cms. *CERN*, 01 2004.

[69] JoAnne L Hewett, Ben Lillie, Manuel Masip, and Thomas G Rizzo. Signatures of long-lived gluinos in split supersymmetry. *Journal of High Energy Physics*, 2004(09):070–070, Oct 2004.

[70] H. Holden and C.F. Coombs. *Printed Circuits Handbook, Seventh Edition*. McGraw-Hill Education, 2016.

[71] J Jeanneret et al. Beam loss and collimation at lhc, cern-lhc-project-report-663. 08 2020.

[72] Jian Song, Qi An, and Shubin Liu. A high-resolution time-to-digital converter implemented in field-programmable-gate-arrays. *IEEE Transactions on Nuclear Science*, 53(1):236–241, 2006.

[73] D.I. Kazakov. Beyond the standard model: In search of supersymmetry. In *2000 European School of High-Energy Physics*, pages 125–199, 8 2000.

[74] V. Khachatryan and another. Search for long-lived charged particles in proton-proton collisions at $\sqrt{s} = 13$ TeV. *Phys. Rev. D*, 94:112004, Dec 2016.

[75] V. Khachatryan et al. The CMS trigger system. *Journal of Instrumentation*, 12(01):P01020–P01020, jan 2017.

[76] W. Kilian, T. Plehn, P. Richardson, and E. Schmidt. Split supersymmetry at colliders. *The European Physical Journal C*, 39(2):229–243, Feb 2005.

[77] Wm. David Kulp. *Ionizing Radiationionizing radiationDetectorsradioactivity-detectors*, pages 5560–5572. Springer New York, New York, NY, 2012.

[78] Kumari et al. Improved-RPC for the CMS muon system upgrade for the HL-LHC. Technical Report arXiv:2005.11396, May 2020.

[79] Priyanka Kumari. Improved-rpc for the cms muon system upgrade for the hl-lhc, 2020.

[80] F. Lagarde et al. High rate, fast timing Glass RPC for the high η CMS muon detectors. *JINST*, 11(09):C09006, 2016.

[81] Christian Lippmann. Particle identification. *Nucl. Instrum. Methods Phys. Res., A*, 666(arXiv:1101.3276):148–172. 61 p, Jan 2011. 61 pages, 30 figures.

[82] Rong-Shyang Lu. The cms preshower construction and commissioning. *Nuclear Instruments and Methods in Physics Research Section A: Accelerators, Spectrometers, Detectors and Associated Equipment*, 617(1):103 – 104, 2010. 11th Pisa Meeting on Advanced Detectors.

[83] Joseph D. Lykken. Beyond the standard model, 2010.

[84] Ahmad Moshaii et al. Rpc simulation in avalanche and streamer modes using transport equations for electrons andions. *Nuclear Instruments & Methods in Physics Research Section A-accelerators Spectrometers Detectors and Associated Equipment - NUCL INSTRUM METH PHYS RES A*, 661, 01 2012.

[85] Philippe Mouche. Overall view of the LHC. Vue d'ensemble du LHC. *CERN*, Jun 2014. General Photo.

[86] E. Noether. Invariante variationsprobleme. *Nachrichten von der Gesellschaft der Wissenschaften zu Göttingen, Mathematisch-Physikalische Klasse*, 1918:235–257, 1918.

[87] Robert Oerter. *The theory of almost everything : the Standard Model, the unsung triumph of modern physics*. Pi Press, New York, 2006.

[88] E. Voevodina on behalf of the CMS Muon group. RE3/1 & RE4/1 RPC chambers integration in the inner region of the forward muon spectrometer in the CMS experiment. *Journal of Instrumentation*, 14(10):C10027–C10027, oct 2019.

[89] Brian O'Keefe. Finding Location with Time of Arrival and Time Difference of Arrival Techniques. Technical report, ECE'17, Senior Capstone Project, 2017.

[90] Carmine Elvezio Pagliarone. Collider physics an experimental introduction. *Journal of Physics: Conference Series*, 287:012005, apr 2011.

[91] J. Paleček, M. Vestenický, P. Vestenický, and J. Spalek. Frequency dependence examination of pcb material fr4 relative permittivity. *IFAC Proceedings Volumes*, 46(28):90 – 94, 2013. 12th IFAC Conference on Programmable Devices and Embedded Systems.

[92] Paolucci et al. Cms resistive plate chamber overview, from the present system to the upgrade phase i. *Journal of Instrumentation*, 8:P04005, 04 2013.

[93] Sung Keun Park. Charge distribution dependency on gap thickness of CMS endcap RPC. Technical Report CMS-CR-2016-073, CERN, Geneva, May 2016.

[94] Dorothea Pfeiffer et al. The radiation field in the gamma irradiation facility gif++ at cern. *Nuclear Instruments and Methods in Physics Research Section A: Accelerators, Spectrometers, Detectors and Associated Equipment*, 866:91 – 103, 2017.

[95] Gabriella Pugliese. The RPC system for the CMS experiment. *IEEE Nucl. Sci. Symp. Conf. Rec*, pages 822–826, 2006.

[96] H Raether. *Electron avalanches and breakdown in gases*. Butterworths advanced physics series. Butterworths, London, 1964.

[97] Simon Ramo. Currents induced by electron motion. *Proc. Ire.*, 27:584–585, 1939.

[98] W Riegler, Christian Lippmann, and R Veenhof. Detector Physics and Simulation of Resistive Plate Chambers. *Nucl. Instrum. Methods Phys. Res., A*, 500(CERN-EP-2002-046):144–162. 27 p, Jun 2002.

[99] Werner Riegler, Christian Lippmann, and Rob Veenhof. Detector physics and simulation of resistive plate chambers. *Nuclear Instruments and Methods in Physics Research Section A: Accelerators, Spectrometers, Detectors and Associated Equipment*, 500(1):144 – 162, 2003. NIMA Vol 500.

[100] Anirban Saha. Phase 1 upgrade of the CMS pixel detector. *Journal of Instrumentation*, 12(02):C02033–C02033, feb 2017.

[101] R. Santonico. Topics in resistive plate chambers. In *3rd International Workshop on Resistive Plate Chambers and Related Detectors (RPC 95)*, pages 1–10, 1995.

[102] R. Santonico and R. Cardarelli. Development of resistive plate counters. *Nuclear Instruments and Methods in Physics Research*, 187(2):377 – 380, 1981.

[103] Hongyan Shi, Xianwen Liu, and Yan Lou. Materials and micro drilling of high frequency and high speed printed circuit board: a review. *The International Journal of Advanced Manufacturing Technology*, 100, 01 2019.

[104] N Siegel. Overview of the LHC Magnets other than the Main Dipoles. *CERN-LHC-Project-Report-422*, page 6 p, Sep 2000.

[105] John Simpson. The cosmic ray nucleonic component: The invention and scientific uses of the neutron monitor – (keynote lecture). *Space Science Reviews*, 93:11–32, 04 2012.

[106] A.M. Sirunyan et al. Precision measurement of the structure of the CMS inner tracking system using nuclear interactions. *Journal of Instrumentation*, 13(10):P10034–P10034, oct 2018.

[107] A Tapper and Darin Acosta. CMS Technical Design Report for the Level-1 Trigger Upgrade. Technical Report CERN-LHCC-2013-011. CMS-TDR-12, CERN, Jun 2013.

[108] H Teng. CMS endcap RPC performance analysis. *JINST*, 9:C08007, 2014.

[109] Daniel Francois Teyssier. CMS Drift Tubes performance. Technical report, CERN, 2016.

[110] The Gfitter Group, Baak, M., Cúth, J., Haller, J., Hoecker, A., Kogler, R., Mönig, K., Schott, M., and Stelzer, J. The global electroweak fit at nnlo and prospects for the lhc and ilc. *Eur. Phys. J. C*, 74(9):3046, 2014.

[111] E. Tournefier. The preshower detector of cms at lhc. *Nuclear Instruments and Methods in Physics Research Section A: Accelerators, Spectrometers, Detectors and Associated Equipment*, 461(1):355 – 360, 2001. 8th Pisa Meeting on Advanced Detectors.

[112] A. Triossi et al. 12(01):C01095–C01095, jan 2017.

[113] M. Tytgat et al. The Upgrade of the CMS RPC System during the First LHC Long Shutdown. The Phase-1 Extension of the CMS Endcap Resistive Plate Chamber System. *PoS*, RPC2012(arXiv:1209.1979):063. 9 p, Sep 2012.

[114] Jian Wang. Upgrade plans and ageing studies for the CMS muon system in preparation of HL-LHC. *Nucl. Instrum. Meth.*, 9 2018.

[115] Ltd. Weeroc Co. Positron emission tomography integrated read-out chip (petiroc2a) datasheet. Technical report, Weeroc Co., Ltd., 2014.

[116] J. Wu. Several key issues on implementing delay line based tdcs using fpgas. *IEEE Transactions on Nuclear Science*, 57(3):1543–1548, 2010.

[117] C. N. Yang and R. L. Mills. Conservation of isotopic spin and isotopic gauge invariance. *Phys. Rev.*, 96:191–195, Oct 1954.

[118] J Ying, YL Ye, Y Ban, H Liu, Zhu, Z Zhu, Thiha Chen, J Ma, and Sijin Qian. Study of an avalanche-mode resistive plate chamber. *Journal of Physics G: Nuclear and Particle Physics*, 26:1291, 07 2000.

[119] Xiaoming Zhang. Overview of alice results. *Nuclear and Particle Physics Proceedings*, 289-290:1 – 6, 2017. 8th International Conference on Hard and Electromagnetic Probes of High Energy Nuclear Collisions.